1

Computer Simulations of Planetary Rings (Revised 29.11.2016)

H. SALO, K. OHTSUKI AND M. C. LEWIS

The local dynamics of planetary rings is governed by the orbital motion, the frequent impacts between ring particles, their mutual self-gravity, and the perturbations exerted by external satellites and embedded moonlets. In Saturn's dense A and B rings the particles collide ~ 100 times per orbital revolution. Although the orbital velocities are ~ 20 km/s, the random velocities related to orbital eccentricities and inclinations are small, of the order of few mm/s (this corresponds to a ring vertical thickness of few tens of meters, excluding strongly perturbed regions). Such gentle impacts do not lead to fragmentation, but still dissipate a significant fraction of random kinetic energy in each collision. This loss is balanced by the viscous gain of energy from the orbital motion around the planet, resulting on a local steady-state in a time scale of few tens of impacts/particle. Characteristics of this energy balance (such as velocity dispersion, geometric thickness, and viscosity) are determined by the frequency and elasticity of impacts, and by the internal density and size distribution of particles. In much longer timescales the ring radial evolution is governed by viscous evolution. Depending on the viscosity-density relation following from the energy balance, the ring can be either stable or unstable against the viscous growth of local perturbations. For example, dense rings composed of quite inelastic particles can become viscously overstable, while less dissipative particles may be prone to viscous instability.

The basic collisional dynamics of planetary rings is theoretically fairly well understood, and in the case of non-gravitating particles the steady-state properties can be obtained analytically from kinetic theory (Goldreich and Tremaine, 1978b; Hämeen-Anttila, 1978; Stewart et al., 1984; Shu and Stewart, 1985; Latter and Ogilvie, 2006), also in the case of dense flattened rings where finite-size (nonlocal) effects become important (Hämeen-Anttila, 1982; Shukhman, 1984; Araki and Tremaine, 1986). The same is true even if particle size distribution and pairwise gravitational encounters are included (e.g. Hämeen-Anttila, 1984; Hämeen-Anttila and Salo, 1993), although the resulting analytical expressions become cumbersome. Similarly, the viscous stability properties of rings can be analyzed via hydrodynamical (Schmit and Tscharnuter, 1995; Schmidt et al., 2001) or kinetic theory approach (Latter and Ogilvie, 2008). Numerical simulations, however, are indispensable for many reasons as they take automatically into account the non-isotrophy of velocity dispersion following from orbital motion, and allow the accurate treatment of dense flattened rings without simplifying assumptions. In particular, the realistic inclusion of collective self-gravity, implying the formation of gravitational wakes and particle aggregates, is still out of scope of analytical treatments.

The fundamental importance of ring particles' feeble mutual gravity for shaping the fine structure of Saturn's rings is strikingly demonstrated by the Cassini stellar (Colwell et al., 2006, 2007; Hedman et al., 2007) and radio occultation measurements (Thomson et al., 2007), which confirm the presence of unresolved trailing structures (self-gravity wakes (Salo, 1992a)) throughout the A and B rings. These transient, continuously re-generated trailing density enhancements arise as a superposition of tiny wakes excited around each individual ring particle, amplified by the interplay of shear and gravity (swing-amplification mechanism, see: Toomre, 1981; Goldreich and Lynden-Bell, 1965). Such structures were envisioned already decades ago (Julian and Toomre, 1966), though in a very different context (and scale - kpcs rather than tens of meters), as a suggestion of how to create and maintain spiral structure in galactic stellar disks. In planetary rings the dissipative impacts between particles provide a natural mechanism which keeps the rings dynamically cool and reactive to such gravitational disturbances. For the same reason the excitation of spiral density waves at satellite resonance locations (Goldreich and Tremaine, 1978a) - another concept originally developed in the context of galaxy dynamics - has its clearest manifestation in Saturn's rings (see e.g. Shu, 1984; Burns and Cuzzi, 2006; Cuzzi et al., 2010). Saturn's rings also provide the most extreme examples of disk warping (Hedman et al., 2011), and the Julian-Toomre type wakes excited around individual massive boulders orbiting among the ring particles ('propellers') (Spahn and Sremčević, 2000; Tiscareno et al., 2006; Sremčević et al., 2007).

This Chapter reviews numerical N-body simulations of self-gravitating, mutually colliding particles, concentrating on a local method, where the evolution of a small ring patch co-moving with the mean orbital motion is followed. After reviewing the main ingredients of the simulations (dynamical equations, treatment of boundaries, impacts, and self-gravity), we illustrate the basic mechanisms affecting the local energy balance and give simulation examples of self-gravity wakes, gravitationally bound particle aggregates, and the nonlinear structures resulting from viscous overstability and instability. Also photometric modeling of dynamical simulations is addressed, and the results compared with both Hubble Space Telescope and Cassini observations.

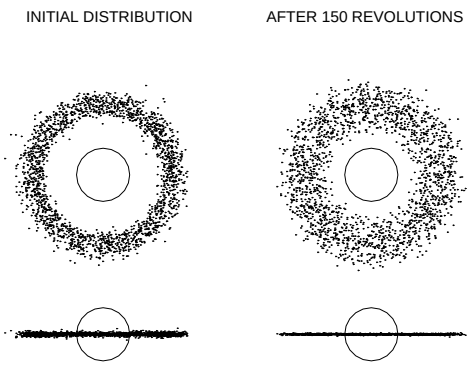

Figure 1.1 Simulation example of azimuthally complete ring. The number of particles N=2000, and the particle radius is 0.005a, where a is the mean distance of particles. The initial width of the ring is 0.2a, yielding a dynamical optical depth $\tau_D = 0.125$. The impacts are described with a constant coefficient of restitution $\epsilon_{\rm n} = 0.5$. During 150 orbital revolutions each particle has experienced on average about 250 impacts: the system has flattened to a few particle diameter thick disk, and has at the same time nearly doubled its radial width.

1.1 Early simulation studies

The pioneering simulation studies of the collisional evolution of planetary rings were performed in the 1970s, by Trulsen (1972), Brahic (1977) and Hämeen-Anttila and Lukkari (1980). All these simulations used the same basic approach: a complete ring of particles revolving around the central body in Keplerian orbits. The particles were identical hard spheres, and impacts were treated as leading to instantaneous changes of relative velocity vectors. Since only a few hundred particles could be followed with the available computer capacity, these simulations were limited to low optical depth $\tau_D \lesssim 10^{-3}$. The particle sizes were unrealistically large compared to the width of the ring, which made it difficult, for example, to separate the time scales for the establishment of local steady-state velocity dispersion from the viscous radial spreading (see Fig. 1.1). Nevertheless, many basic characteristics of collisional systems (see Section 1.7) were discovered, including the existence of a critical upper limit for the coefficient of restitution $\epsilon_{\rm cr}$, required for a stable thermal balance in the case of constant $\epsilon_{\rm n}$ (Trulsen, 1972), a minimum residual velocity dispersion of the order of few times nR (Brahic, 1977), where n is the local angular velocity and R the particle radius, and the establishment of equilibrium with a finite velocity dispersion in a case of a velocity-dependent coefficient of restitution (Hämeen-Anttila and Lukkari, 1980). These simulations also served as important checks for various analytic treatments (see Stewart et al. (1984)). Brahic (1977) also provided the first constraints for the velocity dispersion in Saturn's rings, in terms of timescales for viscous spreading. However, a fundamental breakthrough was provided by the Wisdom and Tremaine (1988) application of the local method to planetary ring simulations.

In contrast to the simulations of a complete ring, in local simulations all calculations are restricted to a small region co-moving with the mean orbital motion of the particles (Fig. 1.2). This allows the extension of the simulations to high optical depths, with realistic particle sizes. However, due to systematic velocity shear individual particles will rapidly leave the calculation region. As described in detail below, this is taken into account by periodic boundary conditions, returning the leaving particles to the calculation region with properly modified position and velocity vectors. An important advantage of the method is that it facilitates the study of local steady-state properties as a function of fixed optical depth. The larger-scale viscous evolution can then be deduced from the viscosity-density relation derived from a set of small-scale simulations for different optical depths. This is justified, based on the large separation of the time scale for the establishment of the local thermal balance ($\propto (\tau_D n)^{-1}$), and the much longer time scale for the radial evolution ($\propto W^2/\nu \propto (\tau_D n)^{-1}(W/H)^2$, where ν is the kinematic viscosity, W is the radial scale of interest, and H is the ring vertical thickness).

The local method, developed for Molecular Dynamics simulations by Lees and Edwards (1972), was first applied to planetary rings by Wisdom and Tremaine (1988) and to stellar disks by Toomre and Kalnajs (1991). In the former study impacts between identical particles were taken into account, but not their mutual gravity, whereas the latter study concentrated only on gravitational forces. In Salo (1992a) both, gravity and impacts, were simultaneously included. Since then, the local method has been extensively used (e.g. Richardson, 1993, 1994; Salo, 1995; Mosqueira, 1996; Daisaka and Ida, 1999; Lewis and Stewart, 2000; Daisaka et al., 2001; Ohtsuki, 1999; Robbins et al., 2010; Perrine and Richardson, 2012).

1.2 The Local Simulation Method

The coordinate system in the local method has its origin at $\vec{r}_0$, a reference point orbiting the planet of mass M_P in a circular orbit at the distance a, with a constant angular velocity $n = \sqrt{GM_P/a^3}$. The x-axis points in the radial direction, the y-axis in the direction of orbital motion, and the z-axis is perpendicular to the equatorial plane, parallel to the angular velocity vector $\vec{n} = n\hat{z}$. Since a rotating reference frame is used, the equations of motion are

$$\ddot{\vec{r}} + 2\vec{n} \times \dot{\vec{r}} + \vec{n} \times (\vec{n} \times \vec{r}) = \vec{F}_G/m + \vec{F}/m \tag{1.1}$$

where $\vec{r} = (x, y, z)$ is a particle's radius vector with respect to $\vec{r}_0$, $\vec{F}_G$ denotes the central force on the particle relative to the force at $\vec{r}_0$, $\vec{F}$ the additional forces, and the two last terms on the left hand side represent the Coriolis and centrifugal terms, respectively. For the Keplerian case (spherically symmetric central body) the difference in the acceler-

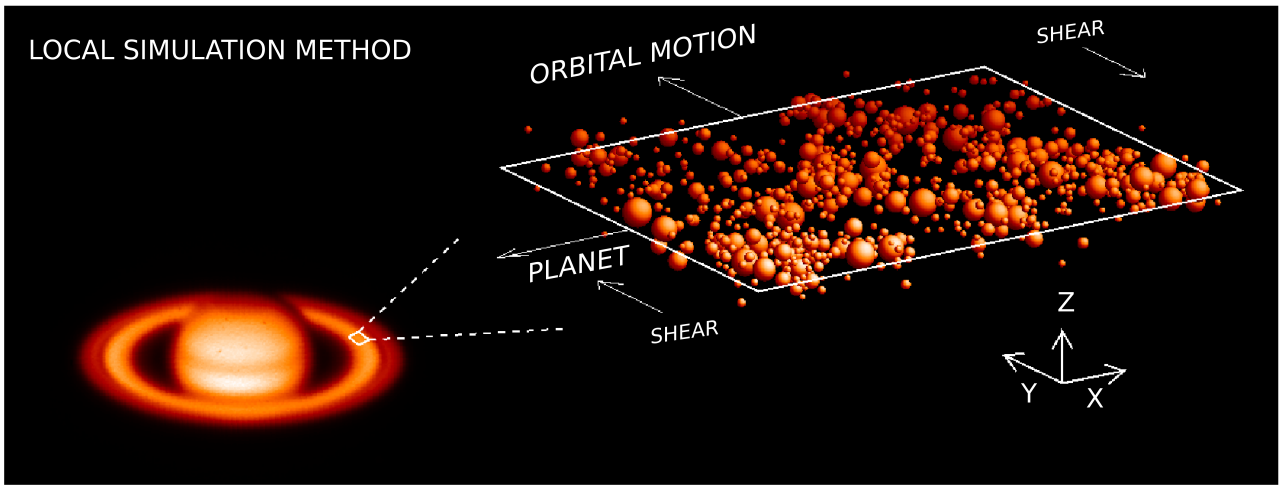

Figure 1.2 Schematic representation of the local simulation method ("shearing brick" method) (see text for explanation).

ation due to the central field is

$$\begin{aligned} \vec{F}_G/m &= -GM_P\left(\frac{\vec{r}_0+\vec{r}}{|\vec{r}_0+\vec{r}|^3}-\frac{\vec{r}_0}{a^3}\right) \\ &\approx -\frac{GM_P}{a^3}\left(\vec{r}-3\frac{\vec{r}\cdot\vec{r}_0}{a^2}\vec{r}_0\right) \\ &= n^2(2x,-y,-z), \end{aligned} \tag{1.2}$$

if only terms linear in $|\vec{r}|/a$ are retained. In the more general case where the azimuthal, radial, and vertical frequencies (n, κ, and n_z) are different from each other[1]

$$\vec{F}_G/m = \left((3n^2-\kappa^2)x, -n^2 y, -{n_z}^2 z\right), \tag{1.3}$$

with

$$\begin{aligned} n^2 &= \frac{F_r}{r}\Big|_{\vec{r}=\vec{r}_o}, \\ \kappa^2 &= \frac{1}{r^3}\frac{d}{dr}(r^3F_r)\Big|_{\vec{r}=\vec{r}_o}, \\ n_z^2 &= \frac{d}{dz}(F_z)\Big|_{\vec{r}=\vec{r}_o}, \end{aligned}$$

where F_r and F_z are the radial and vertical components of the central force. Inserting this in Eq. (1.1) yields

$$\begin{aligned} \ddot{x}-2n\dot{y}+(\kappa^2-4n^2)\,x &= F_x/m, \\ \ddot{y}+2n\dot{x} &= F_y/m, \\ \ddot{z}+{n_z}^2 z &= F_z/m, \end{aligned} \tag{1.4}$$

where F_x, F_y, F_z stand for the components of additional forces besides the central force, e.g. due to impacts and particles' mutual gravity. This is the familiar Hill-approximation, describing the elliptical motion in terms of epicycles superposed on the circular motion of the guiding centre. In the absence of additional forces Eqs. (1.4) have the solution

$$\begin{aligned} x &= x_0 - A\cos[\kappa(t-t_0)], \\ y &= y_0 + \frac{2nA}{\kappa}\sin[\kappa(t-t_0)] + \frac{\kappa^2-4n^2}{2n}\,x_0 t, \\ z &= B\sin[n_z(t-t_1)], \end{aligned} \tag{1.5}$$

[1] Note that in this Chapter the symbol n_z is used for the vertical frequency instead of ν; the latter symbol is reserved for kinematic shear viscosity.

where x_0, y_0, A, t_0, B, t_1 are six constants of integration: x_0 and y_0 are given by the guiding centre location at $t=0$, while $A=ea, B=Ia$ correspond to eccentricity and inclination, and t_0, t_1 to the times of pericenter and ascending node passage, respectively. The guiding centre drifts tangentially with the speed sx_0, where the shear rate

$$s = \frac{\kappa^2-4n^2}{2n} \tag{1.6}$$

reduces to $s=-\frac{3}{2}n$ in the Keplerian case.

The use of linearized equations is physically well justified, as the typical particle excursion from circular orbit may be expected to be at least a factor of 10^{-6} smaller than a. Furthermore, through the linearization the set of Eqs. (1.4) is invariant under the transformation

$$\begin{aligned} (x',y',z') &= (x+\Delta x, y+\Delta y+\Delta x\,st, z), \\ (v_x',v_y',v_z') &= (v_x, v_y+\Delta x\,s, v_z), \end{aligned} \tag{1.7}$$

where Δx and Δy denote arbitrary shifts in radial and tangential directions, respectively. This allows to use simple periodic boundary conditions in simulations: using $\Delta x = n_x L_x$ and $\Delta y = n_y L_y$, where n_x and n_y are integers, and L_x and L_y denote the radial and tangential dimensions of the calculation region,

$$\begin{aligned} (x',y',z') &= (x+n_xL_x, y+n_yL_y+n_xL_xst, z), \\ (v_x',v_y',v_z') &= (v_x, v_y+n_xL_xs, v_z), \end{aligned} \tag{1.8}$$

with $|n_x|, |n_y| = 1, 2, ...$, define a set of image particles (replicas, see Fig. 1.3), so that each particle leaving the actual calculation region ($|x| > L_x/2$ or $|y| > L_y/2$), is replaced by one of its replicas which enters the region from the opposite face, with appropriately modified position and velocity. Especially, if the particle crosses the outer or inner radial boundary, the tangential velocity of the particle is modified by $\Delta v_y = \pm sL_x$, which corresponds to the difference of shear velocity across L_x. Since the mean tangential velocity at the radial coordinate x equals sx, this leaves the shear corrected tangential velocity $v_y - sx$ unaffected. With the use of these periodic boundary conditions the evolution of

the system is independent of the size of the calculation region, provided that the size is large compared to the mean free path between impacts (Wisdom and Tremaine (1988), Salo (1991)). Implicitly it is assumed in the local method that the rings are homogeneous on a scale comparable or larger than the size of the simulation region.

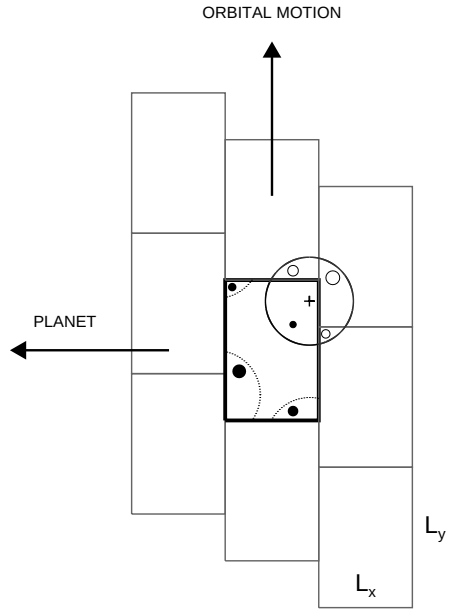

Figure 1.3 Schematic diagram displaying the simulation cell (thick lines) and its eight surrounding replicas (thin lines). Gravitational forces on the given target particle (marked by cross) are calculated from the particles whose nearest images lie within a given maximum distance marked by the circle. The nearest image can either be the actual particle (solid symbols) or one of its copies (open symbols). Likewise, collisional calculations take into account impacts with image particles.

For a system of N particles moving according to Eqs. (1.4) the quantities

$$\begin{aligned} U &= \frac{1}{m_{tot}} \sum_{i=1}^{N} m_i \dot{x}_i, \\ V &= \frac{1}{m_{tot}} \sum_{i=1}^{N} m_i (\dot{y}_i - s x_i), \end{aligned} \tag{1.9}$$

are the analogues to centre-of-mass velocities, where m_{tot} is the total mass. From Eqs. (1.4),

$$\begin{aligned} m_{tot}(\dot{U} - 2nV) &= \sum_i \sum_j {F_x}^{ij}, \\ m_{tot}(\dot{V} + (2n+s)U) &= \sum_i \sum_j {F_y}^{ij}, \end{aligned} \tag{1.10}$$

where $\vec{F}^{ij}$ stands for the mutual impact or gravity force, exerted by particle j on particle i. Since the forces cancel pairwise, the sums on the right-hand sides vanish. Also, U and V are unaffected by boundary crossings. Thus, U and V remain zero at all times if they vanish initially. This provides a useful check for the accuracy of the orbit and impact calculations. In the more general case, U and V oscillate about their initial values, but as shown in Wisdom and Tremaine (1988), the evolution of a system with arbitrary U_0 and V_0 is easily determined from the evolution with $U_0 = V_0 = 0$.

Eqs. (1.4) have the energy integral (multiply with velocities and integrate once),

$$\begin{aligned} E &= \sum_i m_i \left(\frac{1}{2}(\dot{x}_i^2 + \dot{y}_i^2 + \dot{z}_i^2) + ns{x_i}^2 + \frac{1}{2}{n_z}^2 {z_i}^2 \right) \\ &- \frac{1}{2} \sum_i \sum_{j \neq i} G \frac{m_i m_j}{|\vec{r}_j - \vec{r}_i|}, \end{aligned} \tag{1.11}$$

the last term representing the self-gravitational potential energy (we have assumed that the additional forces arise from mutual self-gravity). In contrast to centre-of-mass velocities, the quantity E does not remain constant in boundary crossings or impacts.

1.3 Impact calculations

The impacts between planetary ring particles damp the relative velocity difference between the colliding particles, which leads to dissipation of random kinetic energy. The impacts also transfer energy between planar and vertical directions, and between translational and spin motions. The damping of the relative velocity component in the direction perpendicular to the impact plane is specified by the normal coefficient of restitution $\epsilon_{\rm n}$, describing the energy loss due to irreversible deformations during the impact. Similarly, the tangential coefficient of restitution, $\epsilon_{\rm t}$, can be included, describing the change of the relative velocity component along the impact plane. In this case the exchange of energy with the particles' spin motion needs also be taken into account. Surface irregularities and the overall non-spherical shape of the particles may also affect the impact outcome.

Two main methods are generally used in the description of impacts: i) instantaneous velocity changes ("hard sphere" collisions), where the collisions are treated as discrete events, and ii) force model method, where the impacts are treated in terms of forces affecting during the finite-duration impact ("soft sphere" collisions).

1.3.1 Instantaneous Impacts

In most local simulations (Wisdom and Tremaine (1988), Salo (1991, 1992b,a); Richardson (1994)) an impact model with instantaneous velocity changes has been used. This is well justified, as the contact time in impacts is probably less than one second (Bridges et al., 1984), or of the order of 10^{-5} orbital periods. Below we summarize the equations for the velocity and spin changes in impacts, following from the specified elastic model and the conservation laws of linear and angular momentum. The equations are first derived in

an inertial frame, and then we discuss the slight modifications required when a local rotating frame is used.

1.3.1.1 Contact dynamics

The pre-collisional position, velocity, and spin vector of the impacting particle are denoted by $\vec{r}$, $\dot{\vec{r}}$, and $\vec{\omega}$, respectively, and its radius and mass by R and m. The impact partner is distinguished by the subscript 1, and the post-collisional quantities by a prime. We define

$$\begin{aligned} \vec{v} &= \dot{\vec{r}}_1 - \dot{\vec{r}}, \\ \vec{k} &= \frac{\vec{r}_1 - \vec{r}}{R + R_1}, \end{aligned} \tag{1.12}$$

standing for the velocity difference of the particle centres, and for the unit vector in the direction joining the particle centres. For an impact to take place $\vec{v} \cdot \vec{k} < 0$. The pre-collisional velocity difference at the contact point, taking into account the spins, is

$$\vec{g} = (\dot{\vec{r}}_1 - R_1\vec{\omega}_1 \times \vec{k}) - (\dot{\vec{r}} + R\vec{\omega} \times \vec{k}) \tag{1.13}$$

$$= \vec{v} - (R\vec{\omega} + R_1\vec{\omega}_1) \times \vec{k}. \tag{1.14}$$

The post-collisional contact velocity $\vec{g}\,'$ is determined by the impact model, giving its components in three orthogonal directions $\vec{k}$, $\vec{k} \times (\vec{g} \times \vec{k})$, and $\vec{g} \times \vec{k}$, of which the last two lay on the impact plane; unit vectors in these directions will be denoted by $\vec{k}_T$ and $\vec{k}_\gamma$, respectively. Note that these vectors form a right-handed system. We use the notation

$$\vec{g}\,' = -\epsilon_\mathrm{n}\ \vec{k}\vec{k} \cdot \vec{g} + \epsilon_\mathrm{t}\ \vec{k} \times (\vec{g} \times \vec{k}) + \epsilon_\gamma\ \vec{g} \times \vec{k}, \tag{1.15}$$

which implies

$$\begin{aligned} \vec{k} \cdot \vec{g}\,' &= -\epsilon_\mathrm{n}\ \vec{k} \cdot \vec{g}, \\ \vec{k} \times (\vec{g}\,' \times \vec{k}) &= \epsilon_\mathrm{t}\ \vec{k} \times (\vec{g} \times \vec{k}) + \epsilon_\gamma\ \vec{g} \times \vec{k} \end{aligned} \tag{1.16}$$

Thus ϵ_n denotes the coefficient of normal restitution, and if $\epsilon_\gamma = 0$, then ϵ_t corresponds to friction. For totally elastic impacts $\epsilon_\mathrm{n} = 1$ while with $\epsilon_\mathrm{n} = 0$ the post-collisional perpendicular velocity difference vanishes. Similarly $\epsilon_\mathrm{t} = 1$ means a frictionless impact while if $\epsilon_\mathrm{t} = 0$ the whole tangential velocity difference at the contact point is lost. Note that $\epsilon_\mathrm{n} = \epsilon_\mathrm{t} = 0$ does not imply sticking of particles as the orbital motion is free to separate them. In principle, $-1 \le \epsilon_\mathrm{t} < 0$ is also physically meaningful, corresponding to reversal of tangential velocity difference (Shu and Stewart, 1985). A non-zero ϵ_γ can be used to describe the effect of surface irregularities, giving rise to a post-collisional velocity component perpendicular to both $\vec{k}$ and $\vec{g}$. If included, ϵ_γ needs to be a random variable with a zero mean, and since surface irregularities affect also in the direction of $\vec{k} \times (\vec{g} \times \vec{k})$, a similar random component needs to be present in ϵ_t.

The collisional changes of particles' velocity and spin vectors,

$$\begin{aligned} \Delta\dot{\vec{r}} &= \dot{\vec{r}}\,' - \dot{\vec{r}}, \qquad & \Delta\dot{\vec{r}}_1 &= \dot{\vec{r}}\,'_1 - \dot{\vec{r}}_1, \\ \Delta\vec{\omega} &= \vec{\omega}' - \vec{\omega}, \qquad & \Delta\vec{\omega}_1 &= \vec{\omega}'_1 - \vec{\omega}_1 \end{aligned} \tag{1.17}$$

are determined by the conservation of linear momentum

$$m\dot{\vec{r}}\,' + m_1\dot{\vec{r}}\,'_1 = m\dot{\vec{r}} + m_1\dot{\vec{r}}_1, \tag{1.18}$$

and the conservation of angular momentum

$$\begin{aligned} & m\vec{r} \times \dot{\vec{r}}\,' + m_1\vec{r}_1 \times \dot{\vec{r}}\,'_1 + J\vec{\omega}' + J_1\vec{\omega}'_1 \\ = \ & m\vec{r} \times \dot{\vec{r}} + m_1\vec{r}_1 \times \dot{\vec{r}}_1 + J\,\vec{\omega} + J_1\vec{\omega}_1 \end{aligned} \tag{1.19}$$

where J and J_1 denote the particles' moments of inertia. These equations can be written in a more compact form

$$m\Delta\dot{\vec{r}} + m_1\Delta\dot{\vec{r}}_1 = 0 \tag{1.20}$$

$$m\vec{r} \times \Delta\dot{\vec{r}} + m_1\vec{r}_1 \times \Delta\dot{\vec{r}}_1 + J\Delta\vec{\omega} + J_1\Delta\vec{\omega}_1 = 0 \tag{1.21}$$

Together with the model for $\vec{g}\,'$ (Eq. 1.15), the conservation laws provide nine conditions for the six post collisional velocity components and six spin components. The remaining three relations are obtained by determining how the change of spin is distributed between the two particles. Since the forces acting on both particles are identical except in their sign, the torques during the impact are proportional to the particle radii,

$$\frac{J\Delta\vec{\omega}}{R} = \frac{J_1\Delta\vec{\omega}_1}{R_1}. \tag{1.22}$$

To simplify the notations in solving the above set of 12 equations, Eqs. (1.15), (1.20) - (1.22), we define

$$\vec{q} \equiv R\vec{\omega}, \quad \vec{q}_1 \equiv R_1\vec{\omega}_1, \quad \vec{q}_s \equiv \vec{q} + \vec{q}_1\,, \tag{1.23}$$

$$J = \alpha m R^2, \ J_1 = \alpha_1 m_1 R_1^2. \tag{1.24}$$

Thus $\vec{q}$ denotes the surface velocity due to spin rotation, and α describes the internal mass distribution of particles; for homogeneous spherical particles $\alpha = \alpha_1 = 2/5$. From Eqs. (1.20) and (1.22) we find

$$\Delta\dot{\vec{r}} = -\frac{m_1}{m + m_1}\ \Delta\vec{v}, \quad \Delta\vec{q} = \frac{m_1\alpha_1}{m\alpha + m_1\alpha_1}\ \Delta\vec{q}_s, \tag{1.25}$$

$$\Delta\dot{\vec{r}}_1 = \frac{m}{m + m_1}\ \Delta\vec{v}, \quad \Delta\vec{q}_1 = \frac{m\alpha}{m\alpha + m_1\alpha_1}\ \Delta\vec{q}_s. \tag{1.26}$$

Inserting these in Eq. (1.21), using $\vec{r}_1 = \vec{r} + \vec{k}(R + R_1)$ yields

$$\Delta\vec{q}_s = m_\mathrm{eff}\left(\frac{1}{m\alpha} + \frac{1}{m_1\alpha_1}\right)\Delta\vec{v} \times \vec{k} \equiv f\Delta\vec{v} \times \vec{k}. \tag{1.27}$$

Here

$$m_\mathrm{eff} = \frac{m_1 m}{m + m_1} \tag{1.28}$$

is the effective mass of the pair. In the case of particles with the same internal mass distribution the factor f reduces to $f = 1/\alpha$, which equals $f = 5/2$ for homogeneous spheres. The change of the relative velocity at the point of contact can thus be written (from Eq. 1.14)

$$\begin{aligned} \Delta\vec{g} = \vec{g}\,' - \vec{g} &= \Delta\vec{v} - \Delta\vec{q}_s \times \vec{k} \\ &= \Delta\vec{v} + f\ \vec{k} \times (\Delta\vec{v} \times \vec{k}). \end{aligned} \tag{1.29}$$

Solving for $\Delta\vec{v}$ gives

$$\Delta\vec{v} = \Delta\vec{g} \cdot \vec{k}\vec{k} + (1 + f)^{-1}\left(\Delta\vec{g} \cdot \vec{k}_T\vec{k}_T + \Delta\vec{g} \cdot \vec{k}_\gamma\vec{k}_\gamma\right), \tag{1.30}$$

and inserting the components of $\Delta\vec{g}$ which follow from the impact model, Eq. (1.15),

$$\Delta\vec{g} = -(1 + \epsilon_\mathrm{n})\vec{g} \cdot \vec{k}\vec{k} + (\epsilon_\mathrm{t} - 1)\vec{k} \times (\vec{g} \times \vec{k}) + \epsilon_\gamma\vec{g} \times \vec{k} \tag{1.31}$$

finally gives

$$\begin{aligned}\Delta\vec{v} = & - (1+\epsilon_{\rm n})\vec{g}\cdot\vec{k}\vec{k} \\ & - \frac{2}{7}\left[(1-\epsilon_{\rm t})\vec{k}\times(\vec{g}\times\vec{k}) - \epsilon_\gamma(\vec{g}\times\vec{k})\right]. \end{aligned} \quad (1.32)$$

We have used $(1+f)^{-1} = 2/7$, the value for homogeneous spheres. From Eq. (1.27) we obtain

$$\Delta\vec{q}_s = \frac{5}{7}\left[(1-\epsilon_{\rm t})(\vec{g}\times\vec{k}) + \epsilon_\gamma(\vec{k}\times(\vec{g}\times\vec{k})\right]. \quad (1.33)$$

The changes for the individual particles are now obtained from Eqs. (1.25). Note that in the case with no friction ($\epsilon_{\rm t} = 1$) nor irregularity ($\epsilon_\gamma = 0$), the changes of velocity are independent from spins and no change of spins occurs.

1.3.1.2 Energy dissipation

The total kinetic energy of a colliding pair of particles consists of translational and rotational parts

$$E = E_{kin} + E_{rot} = \frac{1}{2}(m\dot{\vec{r}}^{\,2} + m_1\dot{\vec{r}}_1^{\,2}) + \frac{1}{2}(m\alpha\vec{q}^{\,2} + m_1\alpha_1\vec{q}_1^{\,2}) \quad (1.34)$$

With the centre of mass velocity

$$\vec{v}_c = \frac{m\dot{\vec{r}} + m_1\dot{\vec{r}}_1}{m+m_1}, \quad (1.35)$$

the translational part can be written as

$$E_{kin} = \frac{1}{2}\left((m+m_1)\vec{v}_c^{\,2} + m_{\rm eff}\vec{v}^{\,2}\right), \quad (1.36)$$

and since $\vec{v}_c$ is conserved,

$$\Delta E_{kin} = \frac{1}{2}m_{\rm eff}\Delta(\vec{v}^{\,2}) \quad (1.37)$$

The rotational contribution can be decomposed in a similar manner by defining

$$\vec{q}_c = \frac{m\alpha\ \vec{q} - m_1\alpha_1\ \vec{q}_1}{m\alpha + m_1\alpha_1}, \quad (1.38)$$

leading to

$$E_{rot} = \frac{1}{2}\left[(m\alpha + m_1\alpha_1)\vec{q}_c^{\ 2} + \frac{m_{\rm eff}}{f}\ \vec{q}_s^{\ 2}\right]. \quad (1.39)$$

Since $\vec{q}_c$ is conserved, we have

$$\Delta E_{rot} = \frac{1}{2}\frac{m_{\rm eff}}{f}\Delta(\vec{q}_s^{\ 2}), \quad (1.40)$$

As $\Delta\vec{q}_s = f\Delta\vec{v}\times k$, the total energy change is

$$\begin{aligned}\Delta E &= \frac{1}{2}m_{\rm eff}\left[2\vec{v}\cdot\Delta\vec{v} + (\Delta\vec{v})^2 + 2\Delta\vec{v}\times\vec{k}\cdot\vec{q}_s\ + f(\vec{k}\times\Delta\vec{v})^2\right] \\ &= \frac{1}{2}m_{\rm eff}\left[2\vec{g}\cdot\Delta\vec{v} + (\Delta\vec{v})^2 + f(\vec{k}\times\Delta\vec{v})^2\right]. \end{aligned} \quad (1.41)$$

Inserting $\Delta\vec{v}$ from Eq.(1.30) gives

$$\Delta E = -\frac{1}{2}m_{\rm eff}\left[\Delta(g_n^{\ 2}) + \frac{1}{1+f}\Delta(g_t^{\ 2})\right], \quad (1.42)$$

where $g_n \equiv |\vec{g}\cdot\vec{k}|$ and $g_t \equiv |\vec{k}\times(\vec{g}\times\vec{k})|$. In terms of the impact model we find

$$\begin{aligned}\Delta E = & - \frac{1}{2}m_{\rm eff}\Big[(1-\epsilon_{\rm n}^2)g_n^{\ 2} \\ & + \frac{1}{1+f}\left(1-(\epsilon_{\rm t}+\epsilon'_\gamma)^2 - \epsilon_\gamma^2\right)g_t^{\ 2}\Big], \end{aligned} \quad (1.43)$$

where we have also explicitly included the random component ϵ'_γ, present in $\epsilon_{\rm t}$. Note that the factor $(1+f)^{-1}$ enters by including the exchange of energy between rotational and translational motions. The use of $\epsilon_{\rm t}$ to account for friction without including particle spins, would correspond to setting $f = 0$, thus leading to an incorrect amount of dissipation.

1.3.1.3 Surface irregularities

In principle, irregularities can be described in terms of ϵ_γ, but this treatment has some caveats. Namely, a realistic impact model must have $\Delta E \le 0$. With $\epsilon_\gamma = \epsilon'_\gamma = 0$ the energy change implied by Eq. (1.43) is guaranteed to be negative for all $0 \le \epsilon_{\rm n} < 1, -1 \le \epsilon_{\rm t} \le 1$, but if irregularity is included, the allowed range of ϵ_γ and ϵ'_γ depends on $\epsilon_{\rm n}$, $\epsilon_{\rm t}$, and the ratio g_n/g_t. This makes it hard to interpret the physical meaning of the model. An alternative description for small-scale irregularity was introduced in Salo (1987a,b), where the actual normal vector of the impact plane, $\vec{k}^*$, is allowed to deviate from $\vec{k}$ by a small random amount in each impact,

$$\vec{k}^* = \vec{k}\sqrt{1-\gamma_a^2-\gamma_b^2}\ \ + \gamma_a\ \vec{k}_T + \gamma_b\ \vec{k}_\gamma, \quad (1.44)$$

where γ_a and γ_b are random variables with zero mean, and using

$$\Delta\vec{g} = -(1+\epsilon_{\rm n})\vec{g}\cdot\vec{k}^*\vec{k}^* + (\epsilon_{\rm t}-1)\vec{k}^*\times(\vec{g}\times\vec{k}^*). \quad (1.45)$$

On the other hand, the overall shape of the particles is assumed to stay close to spherical, so that Eq. (1.14) can still be used for the relative velocity at the contact point. The advantage of this description is that the variables γ_a and γ_b have an obvious physical interpretation, and a negative energy loss is guaranteed for any allowed impact with $\vec{k}^*\cdot\vec{v} < 0$.

1.3.1.4 Rotating frame

The calculations presented above are valid in an inertial frame. When using a rotating frame, with same instantaneous axis directions, the velocities and spins are connected to their inertial frame values by

$$\begin{aligned}\dot{\vec{r}}_I &= \dot{\vec{r}}_\Omega + \vec{n}\times\vec{r}_I, \\ \vec{\omega}_I &= \vec{\omega}_\Omega + \vec{n}, \end{aligned} \quad (1.46)$$

where subscripts $_I$ and $_\Omega$ are used to distinguish between the two frames. On the other hand, the instantaneous direction vectors are unaffected. Thus the only differences to Eqs. (1.32) and (1.33) for $\Delta\dot{\vec{r}}$ and $\Delta\vec{\omega}$ would come through $\vec{g} = \vec{v} - (R_1\vec{\omega}_1 + R\vec{\omega})\times\vec{k}$. However, as

$$\begin{aligned}\vec{v}_I &= \vec{v}_\Omega + \vec{n}\times\vec{k}(R+R_1), \\ (R\vec{\omega}+R_1\vec{\omega}_1)_I\times\vec{k} &= (R\vec{\omega}+R_1\vec{\omega}_1)_\Omega\times\vec{k} \\ &\quad +(R+R_1)\vec{n}\times\vec{k}, \end{aligned} \quad (1.47)$$

the vector $\vec{g}$ has the same expression in both frames. Thus no modifications are needed if both, velocities and spins, are treated consistently. Alternatively, we may use $\vec{\omega}_I$ in the collisional equations and add a correction term $(R+R_1)\vec{n}\times\vec{k}$ to $\vec{g}_\Omega$, as was done in Hämeen-Anttila and Salo (1993).

1.3.2 Force model for impacts

The treatment of impacts in terms of instantaneous velocity changes leads to problems if the particles do not separate after the impact. Even in the absence of mutual gravity or attractive contact forces, a situation can occur where the particles have a net central acceleration toward each other even when their post-collisional relative velocity is zero. This corresponds to a sliding motion of the particles, before they are eventually separated by the shear. Following Wisdom and Tremaine (1988) such a phase is convenient to handle with a succession of small jumps, achieved by setting $\epsilon_\mathrm{n} = 1$ whenever the perpendicular impact velocity falls below a threshold value, say, $0.01nR$. Since such impacts do not dissipate much energy to start with, the energy balance of the system is not affected by this replacement.[2]

However, the problem becomes more severe if self-gravity or cohesive forces between particles are included. In these cases impacts may lead to a semi-permanent physical sticking of particles. In the instantaneous impact method this leads to particle overlaps, unless some special measure is applied to force a separation of the particles. Further difficulties may still arise for example if gravitational aggregates are formed, in which case it is insufficient to consider only binary impacts independently from each other. A physically motivated solution, which is also computationally feasible, is to include explicitly the pressure forces affecting the particles in the impact. In Salo (1995) this was done in terms of the linear visco-elastic model originally developed by Dilley (1993) for the theoretical parameterisation of his measurements of velocity and size-dependent elasticity. Likewise, frictional forces may be included in the simulations (Salo, 1995; Morishima and Salo, 2006). Such *Discrete element method (DEM)* algorithms (Cundall and Strack, 1979) are commonly used in granular dynamics (see e.g. Pöschel and Schwager (2005)).

The equations of motion for the impacting particles are

$$\begin{aligned} m\ddot{\vec{r}} &= \vec{F}^{\,imp} + \vec{F}, \\ m_1\ddot{\vec{r}}_1 &= \vec{F}_1^{\,imp} + \vec{F}_1, \end{aligned} \tag{1.48}$$

$$\begin{aligned} J\dot{\vec{\omega}} &= R\vec{k}\times\vec{F}^{\,imp}, \\ J_1\dot{\vec{\omega}}_1 &= R_1(-\vec{k})\times\vec{F}_1^{\,imp}, \end{aligned} \tag{1.49}$$

where $\vec{F}_1^{\,imp} = -\vec{F}^{\,imp}$ represent the impact forces, and $\vec{F}$ and $\vec{F}_1$ include additional forces affecting the particles (central force and gravity of other particles), not causing any torque on the impacting pair. Let us express the impact force as

$$\vec{F}_1^{\,imp} = f_N\vec{k} + f_T\vec{k}_T \tag{1.50}$$

with the normal force (the tangential force f_T will be treated below)

$$\begin{aligned} f_N(\xi) &= \beta_1\xi + \beta_2\dot{\xi}, \quad \xi > 0 \\ &= 0, \qquad\qquad\quad \xi \le 0, \end{aligned} \tag{1.51}$$

where

$$\xi = R + R_1 - |\vec{r} - \vec{r}_1| \tag{1.52}$$

is the penetration depth during the impact. Here $\beta_1 > 0$ is the spring constant of the restoring harmonic force, while due to the dissipative term with $\beta_2 > 0$ the energy stored during the compression phase is not completely returned in the rebound phase. From Eqs. (1.48), (1.51) and (1.52),

$$\begin{aligned} \dot{\xi} &= -\vec{v}\cdot\vec{k}, \\ \ddot{\xi} &= -\vec{v}\cdot\vec{k} - \vec{v}\cdot\dot{\vec{k}}, \\ \dot{\vec{v}} &= (\vec{F}/m - \vec{F}_1/m_1) + \vec{F}_1^{\,imp}/m_\mathrm{eff}, \end{aligned} \tag{1.53}$$

which yields

$$\ddot{\xi} = -\frac{(\beta_1\xi + \beta_2\dot{\xi})}{m_\mathrm{eff}} + C, \tag{1.54}$$

with

$$C = \left(\frac{\vec{F}_1}{m_1} - \frac{\vec{F}}{m}\right)\cdot\vec{k} - \vec{v}\cdot\dot{\vec{k}}, \tag{1.55}$$

where C contains the difference of additional accelerations felt by the particles, as well as the change of the normal direction during the impact.

Ignoring the term C, the solutions of Eq. (1.54) are exponentially damped oscillations (impact starts at $t = 0$ when $\xi = 0$),

$$\xi = \frac{v_n}{\omega}\exp(-\omega_d t)\sin(\omega t) \tag{1.56}$$

where $v_n \equiv \dot{\xi}(0)$, and the oscillation frequency ω and the damping rate ω_d are

$$\begin{aligned} \omega^2 &= {\omega_0}^2 - {\omega_d}^2, \\ {\omega_0}^2 &= \frac{\beta_1}{m_\mathrm{eff}}, \\ \omega_d &= \frac{1}{2}\frac{\beta_2}{m_\mathrm{eff}}, \end{aligned} \tag{1.57}$$

with ω_0 denoting the undamped frequency. The duration of the impact (the length of the first half-cycle) and the coefficient of restitution are

$$\begin{aligned} T_{dur} &= \pi/\omega \approx \pi/\omega_0 \\ \epsilon_\mathrm{n} &= -\frac{\dot{\xi}(T_{dur})}{\dot{\xi}(0)} = \exp\left(-\pi\,\frac{\omega_d}{\omega}\right) \end{aligned} \tag{1.58}$$

Thus specifying β_1/m_eff gives the approximate impact duration, and then β_2 is determined by ϵ_n,

$$\frac{\beta_2}{m_\mathrm{eff}} = \frac{2\omega_0}{\sqrt{(\pi/\ln\epsilon_\mathrm{n})^2 + 1}}. \tag{1.59}$$

[2] Note that setting $\epsilon_\mathrm{n} = 1$ for $g_n \to 0$ is just a useful computational trick: in reality small impact velocity favors particle sticking, thus formally corresponding to $\epsilon_\mathrm{n} = 0, \epsilon_\mathrm{t} = 0$.

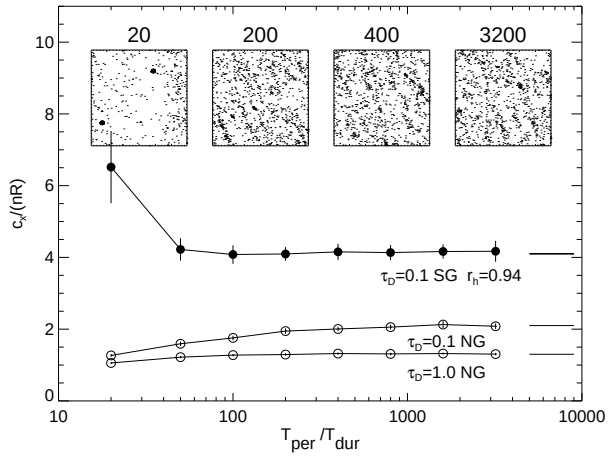

Figure 1.4 The steady-state velocity dispersion in force-method simulations using different impact duration T_{dur}. Results with instantaneous impact method are indicated by the horizontal lines. A constant $\epsilon_{\rm n} = 0.5$ is used. In the non-gravitating simulation (NG) elongation of impact duration ($T_{per}/T_{dur} \lesssim 100$) enhances dissipation, resulting in a lower velocity dispersion. In self-gravitating simulations (SG) this extra dissipation is compensated by the enhanced energy gain due to gravitational viscosity, caused by the longer time the particles spend in the vicinity of each other. For long enough T_{dur} the particles may even stick together ($T_{per}/T_{dur} \lesssim 50$), leading to strongly enhanced gravitational viscosity. The inserts show snapshot from the self-gravitating simulations with different T_{per}/T_{dur} ratios.

Note that a velocity-dependent elasticity law $\epsilon_{\rm n}(v_n)$ can also be used in simulations: in this case the value of β_2 is chosen for each impact based on the pre-impact relative velocity v_n of the pair and the desired $\epsilon_{\rm n}$.

In the force method the particle motion is integrated through the impact, so that the time step is basically determined to be a small fraction of T_{dur}. On the other hand, the total span of any simulation is determined by the orbital time-scale $T_{per} = 2\pi/n$. Since the physical $T_{dur} << T_{per}$, it is advantageous to speed up the calculations by scaling the simulated impact duration to be larger than the physical duration. Otherwise most of the computing time would be spent on calculating the motion of particles which are not currently colliding with much smaller steps than required to resolve their motion due tidal and self-gravitational forces. Indeed, the most attractive feature of the above linear force model is that the impact duration is independent of impact velocity, and is easily adjusted via β_1.

However, there is an upper limit for the allowed T_{dur}, as the solution obtained above ignored the term C: preserving this term may change the implied elasticity. Likewise, the maximum penetration in impacts $\xi_{max} \approx (v_n/\pi)T_{dur}$ should not be too large compared to the particle size: we may write this dependence in the form

$$\frac{T_{dur}}{T_{tper}} \approx \frac{\xi_{max}}{R} \quad \left(\frac{c}{nR}\right)^{-1}. \tag{1.60}$$

Also, if the impact duration is extended to $T_{dur} > 1/\omega_c$, where ω_c is the impact frequency, the binary nature of collisions is not retained. It is thus important to address what is the maximum T_{dur} one can use. According to simulation tests (see Fig. 1.4), using $T_{dur}/T_{per} < 10^{-2}$ leads to a practically same steady state as the instantaneous impact method. Most of the simulations of Sect. 1.7.2 use $\omega_0/n = 400$, corresponding to $T_{dur}/T_{per} = 1/800$. In this case ξ_{max}/R is typically of the order of $10^{-3} - 10^{-2}$.

1.3.2.1 Surface friction

A straightforward way to include friction in the force model is to use

$$f_T \;=\; k_f f_N \tag{1.61}$$

in Eq. (1.51), where $k_f < 0$ denotes the coefficient of friction. This description is quite different from using $\epsilon_{\rm t}$ in the instantaneous impact model, as there is no single choice of k_f that would corresponds to a given $\epsilon_{\rm t}$. To connect k_f to $\epsilon_{\rm t}$, we write $\vec{\dot{g}}$ in terms of Eqs. (1.48) and (1.49) as

$$\begin{aligned}
\vec{\dot{g}} &= \vec{\dot{v}} - (R_1\,\vec{\dot{\omega}}_1 + R\,\dot{\vec{\omega}}) \times \vec{k} \\
&= \frac{1}{m_{\rm eff}}\left(\vec{F}_1^{\,imp} + f\,\vec{k} \times (\vec{F}_1^{\,imp} \times \vec{k})\right) \\
&= \frac{1}{m_{\rm eff}}\left(f_N\,\vec{k} + (1+f)k_f\,f_N\,\vec{k}_T\right),
\end{aligned} \tag{1.62}$$

where f is the factor defined in connection to Eq. (1.29), reducing to 5/2 for homogeneous spheres; we have ignored the extra forces due to orbital motion and self-gravity ($C = 0$). Thus, the total change of normal and tangential velocity difference are

$$\begin{aligned}
\Delta g_n &= \Delta\vec{\dot{g}} \cdot \vec{k} \;=\; \int_{T_{dur}} \frac{f_N}{m_{\rm eff}} dt \quad \equiv (1+\epsilon_{\rm n}) g_n, \\
\Delta g_t &= \Delta\vec{\dot{g}} \cdot \vec{k}_T = \frac{7}{2} k_f \int_{T_{dur}} \frac{f_N}{m_{\rm eff}} dt \quad \equiv (\epsilon_{\rm t} - 1) g_t,
\end{aligned} \tag{1.63}$$

where the force model results are identified with those of the instantaneous impact model. Thus

$$\epsilon_{\rm t} = 1 + \frac{7}{2} k_f (1+\epsilon_{\rm n}) g_n / g_t \tag{1.64}$$

implying $\epsilon_{\rm t} \leq 1$ since $k_f < 0$. Nevertheless, the regime $\epsilon_{\rm t} < 0$ can not be handled with this model, as the frictional force acts against the relative tangential contact velocity. In practice, if friction is strong enough to suppress the tangential velocity difference, $g_t = 0$ appears as a discontinuity in the force and the solution oscillates around $\epsilon_{\rm t} = 0$.

1.3.2.2 Nonlinear impact models and adhesion

In principle, more realistic theoretical models, for both friction and normal restitution (Spahn et al., 1995) are also available. For example, in Brilliantov et al. (1996) the nonlinear elastic collision model of Hertz (1882) was generalized to include visco-elastic dissipation. In this case the perpendicular relative motion during impacts is described by

$$\ddot{\xi} = -A_1\,\xi^{1.5} - A_2\,\xi^{0.5}\dot{\xi}, \tag{1.65}$$

with the constants A_1, A_2 following from material properties. With reasonable choice of parameters this model can

reproduce quite successfully the Bridges et al. (1984) laboratory measurements of $\epsilon_{\rm n}(v_n)$ relation of icy particles (see Sect. 1.7). This treatment has also been extended to tangential friction, in terms of deforming surface asperities (allows also the reversal of tangential velocity difference, i.e. $\epsilon_{\rm t} < 0$; Brilliantov et al., 2007), and to include adhesion between particles (Albers and Spahn, 2006; Brilliantov et al., 2007). Adhesion is included by a term of the form $A_3\xi^{0.75}$ to Eq. (1.65), derived from considering the surface energy associated with the cohesive bonds between particles. With the inclusion of cohesive forces the particles may stick in collisions where the normal component of impact velocity is below a critical threshold value v_{adh} (see Fig. 1.5). According to Albers and Spahn (2006) v_{adh} is of the order cm/sec for cm-sized particles (either in mutual impacts, or in impacts with larger particles), but drops rapidly for larger particles.

Although more realistic than the simple linear force model, the disadvantage of nonlinear collision models is that the scaling of physical impacts to simulations is more complicated, as the impact duration will generally depend on the impact speed. Therefore in simulations of Sect 1.7 the linear force model is used, with the desired $\epsilon_{\rm n}(v_n)$ relation achieved by adjusting the β_2 parameter in each impact according to Eq. (1.59), while keeping the impact duration fixed. Simulations of particle sticking will be briefly addressed, but in the context of linear force model. Since the functional forms of Eqs. (1.54) and (1.65) are different, using an adhesion term proportional to $\xi^{0.75}$ is not reasonable with the linear force model (too close to harmonic force). However, adding a constant extra attractive force F_{adh} between slightly overlapping colliding particles can reproduce the same qualitative behavior as more realistic nonlinear collision models: impacts with $v_n < v_{adh}$ will lead to sticking. In the linear model the critical v_{adh} is directly proportional to F_{adh} (Fig. 1.5).

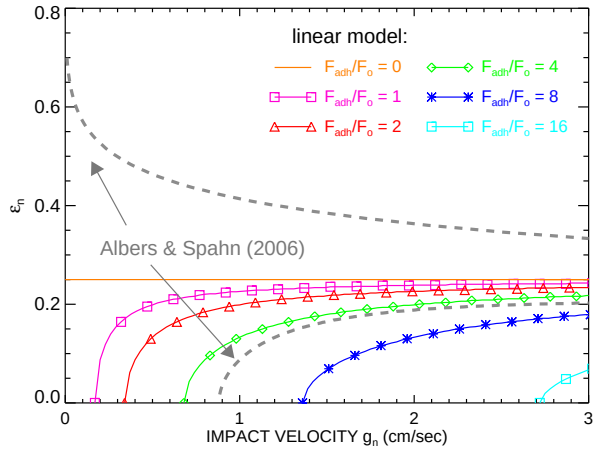

Figure 1.5 Effect of contact forces on $\epsilon_{\rm n}(v_n)$ relation. The thick dashed lines correspond to nonlinear visco-elastic model from Albers and Spahn (2006): the upper dashed curve, omitting contact forces, provides a close match to the Bridges et al. (1984) laboratory measurements (compare with Fig. 1.11). In the lower dashed curve, contact force is included, which for the assumed 2 cm particle size implies sticking for impact velocities $v_n < v_{adh} = 0.88$ cm/sec. The curves with symbols follow from the linear force model, with various magnitudes of constant attractive force F_{adh} between particles in contact. The parameters β_1 and β_2 are chosen to yield $\epsilon_{\rm n} = 0.25$ in the absence of contact forces. For the nominal value F_o, sticking occurs for $v_n < 0.17$ cm/sec; for larger attractive forces, $v_{adh} \propto F_{adh}$.

1.3.3 Search for impact pairs

The speed of the collisional simulation depends crucially on the efficient search for impact pairs. For example, in their simulations of non-gravitating particles Wisdom and Tremaine (1988) used the fact that orbits between impacts are Keplerian epicycles, and solved iteratively for the intersection time of each pair of epicycles. The impact of the pair with the smallest impact time was executed with instantaneous velocity changes, and the post-impact orbital elements of the pair members were re-calculated, leading to updated intersection times with all the other particles. The system was thus moved on from one impact to the next (the method is called "event-driven"). Similar methods were used also in the early simulations of rarefied azimuthally complete rings: due to extremely long intervals between impacts elaborate schemes were developed for detecting orbital intersections taking place after even several hundreds of synodic periods (Hämeen-Anttila and Lukkari, 1980).

Event-driven methods are fairly fast for small particle numbers ($N \approx 50$ in Wisdom and Tremaine (1988)), but as N increases, the checking of next orbital intersections between all $N(N-1)/2$ pairs gets excessively slow. Also, the inclusion of additional forces besides the central gravity poses problems. Therefore, in the self-gravitating case the equations of motions are integrated with small time steps, and the potential intersections during each step are searched only among the neighboring particles. Similar stepwise time integration is advantageous also in the case of high particle density and large N, even if self-gravity is not included. Provided that the step size is small, the distances between particles can be expanded as a second-order Taylor polynomial, providing a fast method for constructing a list of potential impacts during the step (Salo, 1991). From this list, the impacts during the time step are then executed as in the event-driven method.

Regardless of the time-advancement method a considerable speedup can be achieved if the number of pairs examined for potential impacts is kept as small as possible. This can be done quite efficiently by keeping track of the maximum pre-step separation which has actually led to an impact during previous steps, and by checking in each step only those pairs whose distance does not exceed this maximum, multiplied by some threshold factor. This threshold must be chosen in a manner which ensures that no impacts are lost, and it also must be dynamically adjusted as the velocity dispersion of the system evolves. A useful trick is to sort the particles according to their radial coordinate and choose first only pairs whose radial distances fall below the threshold. In the optimal case, the number of pairs examined is proportional to $c/(nR)N$. Note that the actual or-

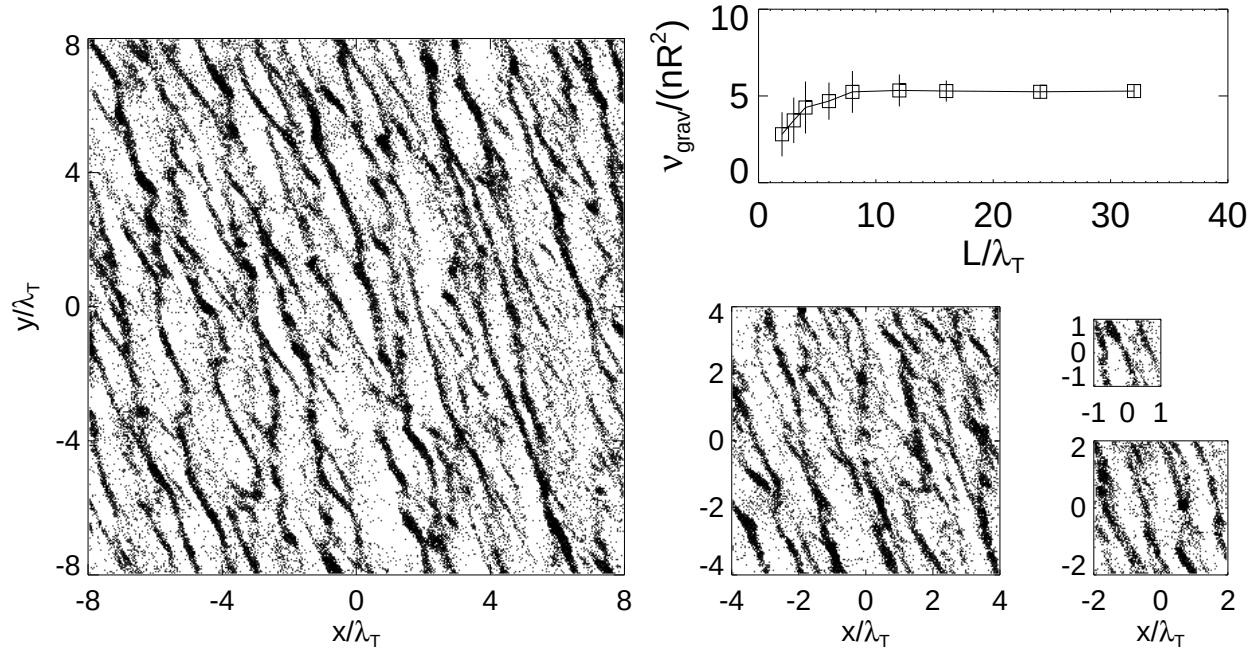

Figure 1.6 Snapshots of self-gravitating simulations with different sized calculation regions, after 50 orbital periods. In each simulation $\tau_D = 0.5$, $\epsilon_{\rm n} = 0.5$ $\rho = 900$ kg/m^3, $R = 1$m, and $a = 100,000$ km ($r_h = 0.82$). The width of the square-shaped region is $L/\lambda_T = 32, 16, 8, 4, 2$. In physical units the Toomre critical wavelength $\lambda_T = 41.6$m. The self-gravity is calculated from all particles within a cylindrical radius $\Delta_{max} = L/2$. Gravitational forces from within $\Delta_{min} = 0.25\lambda_T$ are calculated with the PP-method and beyond that with the PM-method, using a grid spacing of $\lambda_T/16$. The graph shows the gravitational viscosity (Eq. 1.89) as a function L/λ_T (averaged between 25-50 orbits).

bital integration needs not to be performed by a Taylor series: for example in Salo (1995) a fourth order Runge-Kutta integration was utilized, and the impact locations initially estimated by the second-degree polynomial expansion were iteratively improved to correspond to the full accuracy of the integration. See section 1.6 for more detailed considerations of how to speed up various parts of the numerical calculations.

It must be stressed that it is important to take correctly into account impacts taking place over boundaries of the local calculation region. For small calculation regions this fraction can be quite significant, and the omission of such impacts will considerably modify the energy balance, and thus, all steady-state properties of the system. Also, if the force method is used, even a single non-detected impact may lead to large injection of energy to the system if it happens to lead to a deep overlap on the next step. However, such a situation is easy to detect by monitoring the ξ_{max} during the simulation.

1.4 Calculation of self-gravity

1.4.1 Force evaluation

Inclusion of gravitational forces increases the computational burden significantly, as in principle the forces between each particle pair need to be included (as well as to account for the contribution of the replicas of the local calculation region). Moreover, self-gravity typically enhances the velocity dispersion and increases the impact frequency (see Section 1.7.2). Both factors make the collisional calculations more time consuming. These problems are especially pronounced in the case of a weak tidal field, i.e. far from the planet, when gravitationally bound particle aggregates form. Proper simulation of self-gravity also sets additional constraints for the required minimum size of the calculation region, since it must exceed the scale of the self-gravity wake structures formed via gravity (roughly of the order of Toomre critical wavelength λ_T, see Fig 1.6). In practice this means using at least $10^4 - 10^5$ simulation particles. On the other hand, for non-gravitating spatially uniform systems a fairly modest particle number ($10^2 - 10^3$) is usually sufficient to give the steady-state properties with a good accuracy.

The most straight-forward way of force evaluation is the *particle-particle (PP)* method, using a direct summation over particle pairs. The obvious advantage is that no approximations are involved, the gravitational field corresponding exactly to that implied by the particle ensemble. The method can also be fairly efficient (Daisaka et al., 2001) when using a special-purpose processor, like GRAPE, with a hardware calculation of gravity forces (Makino and Funato, 1993). With standard-type processors the implied N^2 time consumption becomes prohibitively large for a few thousand

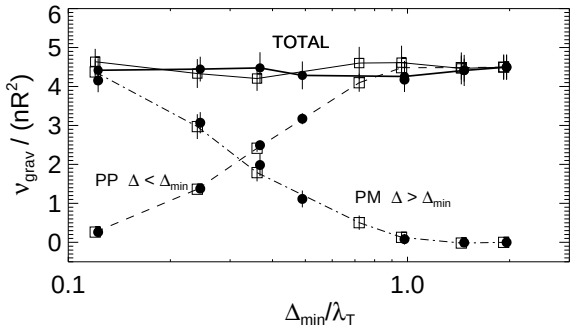

Figure 1.7 The near (PP) and far (PM) contributions to self-gravity, measured in terms of gravitational viscosity (Eq. 1.89), are compared for different dividing distances Δ_{min}. Simulation parameters are the same as in the previous figure, and the total extent of the simulation region is $4\lambda_T \times 4\lambda_T$. The rightmost point corresponds to using solely PP method. Two set of simulations are shown, with $\lambda_T/16$ (thin lines, open squares) and $\lambda_T/32$ (thick line, filled circles) PM grid spacing. Within error bars, the total ν_{grav} is the same in all simulations.

particles, so that other methods are needed. Also, due to partial cancellation of distant forces it is in fact unnecessary to calculate the contribution from distant particles with the same accuracy as that of the nearby particles.

This fact is utilized in *hierarchical tree-codes*, where the distant particles are grouped together in force calculation, so that only few low order moments of their distribution are included (see e.g. the galaxy simulation codes described in Barnes and Hut, 1986; Hernquist and Katz, 1989). The essential part of the method is the efficient construction of the connected particle lists ("tree"), leading to a $N \ln N$ dependence of the CPU-time consumption. Richardson (1994) first applied this method to self-gravitating rings. On the other hand, N-body simulations of galactic dynamics often employ *particle-mesh (PM)* method (see Sellwood, 2014): the density of the system is tabulated in a regular mesh, and the forces (or gravity potential) at each mesh location are evaluated by convolving the density with the interaction law, and then interpolating to the particle locations. The speed of the method relies on the use of a Fast Fourier Transform for performing the force convolution, and in the optimal case the CPU-time consumption of gravity calculations is determined mainly by the interpolation of forces, being linear in N. In current large-scale cosmological simulations the tree and PM methods are often combined (Springel, 2005).

The important difference between planetary rings and galaxy disks is that binary gravitational encounters between ring particles are not insignificant compared to the mean gravitational field (rings are not 'collisionless'). Therefore the smoothing of forces implied by the gravity mesh (or by explicit gravity softening) is incorrect. On the contrary, the most important contributions from self-gravity come from the fluctuating gravitational forces exerted by the nearest neighboring ring particles (within $\sim \lambda_T$, see Fig. 1.8).

An obvious way to speed up the calculations, while retaining the accurate treatment of nearby gravity encounters, is to combine PP and PM methods, for example in a manner that was employed in Salo et al. (2001). In this treatment the gravitational force exerted on each particle is divided in a nearby and distant contribution,

$$\vec{F}_i = \vec{F}_i^{\,near} + \vec{F}_i^{\,far},$$

$$\vec{F}_i^{\,near} = G \sum_{\Delta_{ij}<\Delta_{min}} m_j \frac{\vec{r}_j - \vec{r}_i}{|\vec{r}_j - \vec{r}_i|^3}, \tag{1.66}$$

$$\vec{F}_i^{\,far} = G \int_{\Delta>\Delta_{min}} \rho(\vec{r}) \frac{\vec{r} - \vec{r}_i}{|\vec{r} - \vec{r}_i|^3}\, d^3r, \tag{1.67}$$

where Δ denotes the projected 2D distance in the xy-plane. The near contribution is calculated by direct particle-particle summation, in order to include accurately the effects of close gravitational encounters, as well as the gravitational sticking of particles. Typically $\Delta_{min} << L_x, L_y$, so that just a few percents of all $N(N-1)/2$ particle pairs are involved. The latter, usually smaller distant contribution is calculated with a particle-mesh method.

An efficient way to calculate the PM contribution is to use FFT in a sheared coordinate system, defined by the transformation

$$\begin{aligned} u &= x, \\ v &= y - tsx \mod L_y, \end{aligned} \tag{1.68}$$

where t is the time since the beginning of the simulation and $s = -\frac{3}{2}n$ in the Keplerian case. In these coordinates the Eqs. (1.8) for the image particles transform into

$$\begin{aligned} u' &= u + n_x L_x, \\ v' &= v + n_y L_y. \end{aligned} \tag{1.69}$$

indicating that the system is double periodic in the planar directions. We define a 3D Cartesian mesh with $m_u \times m_v \times m_z$ cells, and tabulate the mass $\delta m(u, v, z)$ in each cell by a cloud-in-cell (CIC) assignment. The size of the cells is denoted with Δu, Δv, and Δz. In planar directions the mesh has the same size as the calculation region, $|u| < L_x/2, |v| < L_y/2$. The vertical coverage of the mesh, $|z| < L_z/2$, can be either a constant, or varied according to the vertical thickness of the system, using $L_z/2 = k_z\sqrt{\overline{z^2}}$, for example with $k_z = 3$: the small fraction of particles with $|z| > L_z/2$ contribute insignificantly to the total density and can be ignored. The force on each cell center (labeled with i, j, k) is obtained with a convolution over other cells (labeled with l, m, n)

$$\vec{F}_{i,j,k} = \sum_{l,m,n} \delta m_{l,m,n}\ \vec{\Gamma}_{l-i,m-j,n-k} \tag{1.70}$$

where $\vec{\Gamma}$ (with same number of elements as δm) denotes the Green function for the gravitational interaction between the cells. Written in terms of the newly defined coordinates,

$$\vec{\Gamma}_{abc} = G\left[a\Delta u, b(\Delta v + st\Delta u), c\Delta z\right] / {d_{abc}}^3 \tag{1.71}$$

with

$$d_{abc} = \left[(a\Delta u)^2 + (b(\Delta v + st\Delta u))^2 + (c\Delta z)^2\right]^{1/2}. \tag{1.72}$$

To exclude the near contribution Γ_{abc} is set to zero for $(a\Delta u)^2 + (b(\Delta v + st\Delta u))^2 < {\Delta_{min}}^2$.

If carried out by direct summation, the convolution in Eq. (1.70) would require $\propto (m_u m_v m_z)^2$ operations. Even for moderate spatial resolution this would mean an excessive number of calculations (even larger than that for the direct summation over all $N(N-1)/2$ pairs). It is therefore essential to utilize the Fourier convolution theorem, according to which the inverse transform of mesh forces equals the product of the inverse transforms of density and Green function,

$$\widetilde{\vec{F}}_{i,j,k} = \widetilde{\delta m}_{l,m,n}\, \widetilde{\vec{\Gamma}}_{l-i,m-j,n-k}. \tag{1.73}$$

In order to be able to apply the convolution theorem, we double the mesh size in the vertical direction, padding the extra cells with zeros. Using a Fast Fourier Transform, the number of calculations becomes proportional to $(m_u \ln m_u)(m_v \ln m_v)(2m_z \ln 2m_z)$, making the method feasible. The forces at the particle locations are interpolated from the grid, with the same CIC-assignment as in the tabulation of density. The forces on the few particles with $|z| > L_z/2$ are calculated with an extrapolation from the grid. In this manner the force on each particle is due to the density in the region which corresponds in size to the whole original rectangular calculation region (see Fig. 1.3). If a circular region is desired (to avoid any artificial 'polarization' of forces due to corners of the region) we can set the Γ_{abc} to zero beyond some distance $\Delta_{max}(< \max\{L_x/2, L_y/2\})$.

Figure 1.7 shows the gravitational viscosity (Eq. (1.89)) from $4\lambda_T \times 4\lambda_T$ simulations where different dividing distances Δ_{min} between PP and PM methods are used, confirming that similar results are obtained in all cases. However, the gravity calculation is about 10 times faster when using PP+PM with $\Delta_{min}/\lambda_T = 1/8$ in comparison with using just the PP method to calculate gravity from within $2\lambda_T$. For larger calculation regions and particle numbers, the gain in speed becomes even more important.

1.4.2 Approximate treatments of self-gravity

Fully self-consistent calculation of particles' mutual gravity, as described above, is quite CPU time intensive. Wisdom and Tremaine (1988) devised a simple method for mimicking self-gravity in terms of an enhanced vertical frequency $n_z > n$ in the dynamical equations. They estimated the vertical self-gravity inside the ring layer from Poisson's equation,

$$F_{sg}(z) = -2\pi G \int_{-z}^{z} \rho(z')dz' = -\frac{4\pi G\Sigma_0}{h} z, \tag{1.74}$$

where the ring is approximated with a homogeneous infinite layer with a vertical half-thickness h and constant surface mass density Σ_0. Combining with the vertical component of the central field, $F_c = -n^2 z$, gives

$$F_z(z) = -\left(n^2 + \frac{4\pi G\Sigma_0}{h}\right) z \equiv -{n_z}^2 z \tag{1.75}$$

Most of their simulations used a constant $n_z/n = 3.6$, which corresponds to $F_{sg}/F_c \approx 12$, assumed to approximate the enhancement in vertical gravity due self-gravity in the dense B-ring of Saturn. Such a treatment mimics qualitatively quite well the effects of vertical gravity, like the enhanced impact frequency (see Sect. 1.7), which leads to strongly increased non-local viscosity, thus promoting viscous overstability. Indeed, the use of $n_z/n > 1$, even if not realistic for exploring the full effects of self-gravity, is a useful method when analyzing overstability in terms of hydrodynamic transport coefficients evaluated from N-body simulations (Salo et al., 2001; Schmidt et al., 2001). Nevertheless, since the approximation ignores the planar components of gravity, which are responsible for the emergence of self-gravity wakes, it is questionable how useful it is for describing real systems in any quantitative way. Also, the originally used enhancement factor 3.6 is likely to overestimate the vertical field considerably, since it is based on space density $\rho_s = \Sigma_0/(2h) = 400$ kg/m^3 inside the ring layer (Wisdom and Tremaine, 1988). For example, with the current estimate $\Sigma_0 \approx 700$kg/m^2 (Hedman and Nicholson, 2016) this would correspond to unlikely small vertical thickness $h \approx 1$ meters.

Another useful approximation can be applied to the calculation of axisymmetric component of self-gravity, in terms of a superposition of infinite plane waves. We first make a radial Fourier decomposition of the tangentially averaged surface density

$$\Sigma(x) = \Sigma_0 \left[1 + \sum_{m=1}^{\infty} A_m \cos\left(m\frac{2\pi}{L_x}(x - x_m)\right)\right], \tag{1.76}$$

where A_m and x_m are the fractional amplitude and phase of different m-components with wavelengths $\lambda = L_x/m$. We then treat each component as an infinite plane wave, and use the Poisson equation for an infinite 2D sheet to calculate the corresponding radial force. Superposition of modes with different m gives

$$F_x(x) = -2\pi G\Sigma_0 \sum_{m=1}^{m_{max}} A_m \sin\left[m\frac{2\pi}{L_x}(x - x_m)\right]. \tag{1.77}$$

A finite m_{max} is used in order to suppress small scale noise. Such a treatment was applied in Salo and Schmidt (2010) to compare viscous instability in N body simulations to Schmit and Tscharnuter (1995) hydrodynamic predictions in the case axisymmetric self-gravity is included.

1.4.3 Time integration

In the force method the basic timestep of integration is determined by the need to resolve the rebound of individual particle pairs. Depending on the chosen spring constant of the restoring harmonic force, this requires time step of the order of $\Delta T_{imp} = (0.01 - 0.1)T_{dur} \sim (10^{-4} - 10^{-5})T_{orb}$, where T_{dur} is the impact duration. On the other hand, self-gravitational forces are practically constant over such sort time scales. To speed up calculations, one can therefore use a larger time step, say $\Delta T_{grav} \sim 10^{-3} T_{orb}$, for updating the gravity forces. This simple method works well in the case of gravity wake structures: the errors made in keeping the self-gravity constant tend to cancel each other on the average. However, when particles stick physically, this method

may lead to artificial destabilization of gravity aggregates via rotational instability (Karjalainen and Salo, 2004). This is solely a numerical artifact, rising from the fact that then the force integration errors do not cancel each other, but lead to a net torque on particles attached to the aggregate. As illustrated in Karjalainen and Salo (2004) a totally sufficient remedy is to calculate both the forces and their time derivatives at the beginning of each gravity step, and then apply linear extrapolation of self-gravity during the step.

1.5 Extracting quantities from simulations

The fundamental[3] quantity describing both the dynamics and observed structures of Saturn's rings is the dynamical (geometric) optical depth, defined as the total surface area of particles divided by the total area. For identical particles with radius R

$$\tau_D = \frac{N\pi R^2}{L_x L_y}. \tag{1.78}$$

One of the main advantages of the local method is that the optical depth (and surface density in case of self-gravitating particles) of the system is fixed. Thus, after the establishment of local energy balance, all dynamical properties characterizing the steady-state corresponding to this τ_D can be obtained with an arbitrary accuracy, by time averaging over sufficiently long time intervals over all particle orbits and impacts. The efficiency of time averaging was strikingly demonstrated in Wisdom and Tremaine (1988), who made a practically complete study of identical, non-gravitating particles, up to $\tau_D \sim 3$, using experiments with only $N = 50$ particles.

1.5.1 Steady-state quantities

The interesting dynamical quantities include the impact frequency ω_c, the velocity dispersion tensor $\widehat{C}_{\alpha\beta}$, the pressure tensor $\widehat{P}_{\alpha\beta}$ and shear viscosity $\eta = -(1/s)\widehat{P}_{xy}$. Other important properties are the geometric thickness H, and the volume filling factor $D_3(z)$, useful for connecting the dynamical estimates to photometric observations of rings. In non-gravitating case the steady-state values of all these quantities are determined by the optical thickness of the system τ_D, the size distribution of particles $N(R)$, and their elastic properties $\epsilon_{\rm n}, \epsilon_{\rm t}$. The effects of self-gravity depend on the internal density ρ of the particles, and the planetocentric distance.

The extraction of the impact frequency ω_c is straightforward both in the instantaneous impact and force method simulations (total number of impact detections/particle/time interval, divided by factor 2 to avoid counting twice the same impact), as long as the tendency for particle sticking is weak (weak to moderate self-gravity not leading to bound aggregates). In the calculation of impact related mean values, like the average of $\epsilon_{\rm n}$ in the case of velocity dependent elasticity, one can weight with v_n to exclude the contribution of possible sliding motion, if described by small, totally elastic rebounds in the instantaneous impact method.

The flow of momentum across the ring consists of a local contribution, related to the momentum carried with the particles during their random motions between successive impacts, and of a nonlocal contribution, arising due to momentum transferred via impacts or via gravitational forces, between particles at different radial distances (Wisdom and Tremaine, 1988). We denote the particle positions by $\vec{r}$ and their random velocities by $\vec{c} = \dot{\vec{r}} - \vec{u}$, with $\vec{u}$ standing for the mean flow velocity at $\vec{r}$. For simplicity, we restrict our attention to the case of a linear shear profile $\vec{u} = sx\hat{\vec{e}}_y$, where $\hat{\vec{e}}_y$ denotes the unit vector in the tangential direction.

By definition, the components of the pressure tensor $P_{\alpha\beta}$ give the amount of the β-component of momentum transferred in the α-direction, per unit area and unit time. When evaluating the momentum flow in simulations, it is convenient to include all particles and impacts, regardless of their vertical coordinate. This corresponds to a vertical averaging

$$\overline{\widehat{P}_{\alpha\beta}} = \int_{-\infty}^{\infty} \widehat{P}_{\alpha\beta} \;\; dz \tag{1.79}$$

From hereon we denote $\overline{\widehat{P}_{\alpha\beta}}$ simply by $\widehat{P}_{\alpha\beta}$, thus having the units of momentum/unit time/unit length.

The local contribution to the pressure tensor is obtained by adding the momenta $p_\beta = mc_\beta$ of the N particles, moving with velocity c_α with respect to the mean flow,

$$P_{\alpha\beta}{}^{local} = \frac{1}{A_o}\sum_i^N (c_\alpha)_i (mc_\beta)_i = N_2\,\overline{mc_\alpha c_\beta}, \tag{1.80}$$

where A_o is the area of the simulation region and $N_2 = N/A_o$ denotes the surface number density. The bar indicates average over particles. Once the steady-state has been achieved, one can improve the accuracy by averaging over arbitrarily long time intervals.

The standard formula for nonlocal momentum transfer is (Wisdom and Tremaine 1988)

$$P_{\alpha\beta}{}^{nl} = \frac{1}{A_o \Delta t}\sum_{impacts} \Delta r_\alpha \, m_> \delta c_{\beta_>}, \tag{1.81}$$

where the summation is over all impacts occurring during the time interval Δt, and $m_>\,\delta c_{\beta_>}$ denotes the change of the momentum of the particle with the larger r_α in each impact, and Δr_α the absolute difference in the r_α-coordinates of the impacting particles. However, application of this formula is problematic in the case of strong particle grouping, as it may be difficult to identify the separate impacts. For the case of force-method impact calculation, the collisional change of momentum is

$$m_>\delta c_{\beta_>} = \int_{T_{dur}} F_{\beta_>} dt, \tag{1.82}$$

where F_β denotes the impact force felt by the particle with the larger r_α coordinate, and T_{dur} is the duration of the

[3] Observationally the importance comes from the close correspondence of τ_D to the normal photometric optical depth $\tau_\perp$, which is the quantity inferred from occultation experiments: in the limit of homogeneous low filling factor systems τ_D and $\tau_\perp$ are identical. However, in a typical case of non-homogeneous and/or high filling factor rings they generally differ, see Sect. 1.11.2.1

impact. By defining

$$F_{\beta>} = \sum_i \sum_{\substack{j \\ (r_\alpha)_j > (r_\alpha)_i}} F_\beta^{ij}, \tag{1.83}$$

where $\vec{F}^{ij}$ stands for the impact force exerted by particle i on the particle j, with $\vec{F}^{ij} \neq 0$ for colliding, overlapping pairs, and zero otherwise, the integral (1.82) can be extended to the whole interval Δt, also covering the possibility of particles experiencing multiple simultaneous impacts, or even a permanent sticking of particles. Summing over all particles then gives an equation corresponding to Eq. (1.81),

$$P_{\alpha\beta}{}^{nl} = \frac{1}{A_o}\left\langle \sum_i \sum_{\substack{j \\ (r_\alpha)_j > (r_\alpha)_i}} ((r_\alpha)_j - (r_\alpha)_i) F_\beta^{ij} \right\rangle, \tag{1.84}$$

where the average is taken over an arbitrary time interval. Furthermore, Eq. (1.84) can obviously be generalized to the momentum flow due to long-range forces, e.g in the case of self-gravity,

$$P_{\alpha\beta}{}^{grav} = \frac{1}{A_o}\left\langle \sum_i \sum_{\substack{j \\ (r_\alpha)_j > (r_\alpha)_i}} -Gm_i m_j \frac{((r_\alpha)_j - (r_\alpha)_i)((r_\beta)_j - (r_\beta)_i)}{|\vec{r}_j - \vec{r}_i|^3} \right\rangle. \tag{1.85}$$

Likewise, $\vec{F}^{ij}$ can be identified with adhesive forces, Eq. (1.84) then giving their contribution to the nonlocal pressure. In the case of well defined separate impacts, Eqs. (1.81) and (1.84) give identical results for the nonlocal pressure tensor.

The corresponding contributions to the (vertically integrated) dynamic shear viscosity are readily evaluated from $\eta = -(1/s)P_{12}$. In the case of Keplerian shear, $s = (-3/2)n$, and we have

$$\eta_{local} = \frac{2}{3n} N_2 \langle \overline{m c_x c_y} \rangle, \tag{1.86}$$

$$\eta_{nl} = \frac{2}{3n} \frac{1}{A_o \Delta t} \sum_{impacts} m_> \Delta x_> (\delta c_y)_> \tag{1.87}$$

$$= \frac{2}{3n} \frac{1}{A_o} \left\langle \sum_i \sum_{\substack{j \\ x_j > x_i}} \Delta x_> (F^{ij}{}_y)_> \right\rangle, \tag{1.88}$$

$$\eta_{grav} = \frac{2}{3n} \frac{1}{A_o} \left\langle \sum_i \sum_{\substack{j \\ x_j > x_i}} -Gm_i m_j \frac{(x_j - x_i)(y_j - y_i)}{|\vec{r}_j - \vec{r}_i|^3} \right\rangle. \tag{1.89}$$

The kinematic shear viscosities are obtained from these, dividing by the surface mass density of the system $\Sigma = N_2 \overline{m}$. In particular, in the case of identical particles (Wisdom and Tremaine, 1988)

$$\nu_{local} = \frac{2}{3n} \overline{c_x c_y}, \tag{1.90}$$

$$\nu_{nl} = \frac{2}{3n} \frac{1}{N \Delta t} \sum_{impacts} \Delta x_> (\delta c_y). \tag{1.91}$$

The above formula for gravitational viscosity is identical to that in Daisaka et al. (2001). Fig. 1.8 shows the contributions to the integrand of Eq. 1.89, arising from different relative locations $\Delta x = x' - x$, $\Delta y = y' - y$. Largest gravitational torques are exerted by material within $\sim 0.25\lambda_T$, and almost all of ν_{grav} is due to particles within one λ_T.

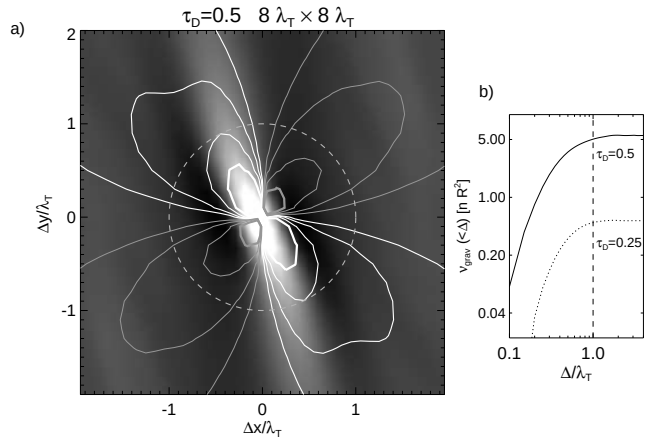

Figure 1.8 a) The contributions to gravitational viscosity (Eq. 1.89). The contours indicate the mean torque density exerted from relative location $(\Delta x, \Delta y)$: positive (white contours) by the particles on the trailing quadrants and negative (gray contours) from the leading quadrants. The gray scale background image is the 2D auto-correlation function (Eq.1.95) for the same simulation. Note the slightly larger positive net torques arising due to overdensities in the trailing quadrants. In b) the cumulative gravitational viscosity due to material within a cylindrical radius Δ is shown as a function of Δ/λ_T.

The velocity dispersion tensor is collected by sampling the random velocity components of each particle with short intervals and tabulating the averages values as a function of simulation time. In particular, in Sect. 1.7 we will use the time-averaged 1-d velocity dispersion c to characterize the dynamical "temperature" of the system

$$c^2 = \frac{1}{3}\left\langle \overline{{c_1}^2 + {c_2}^2 + {c_3}^2} \right\rangle = \frac{1}{3} \frac{tr \hat{P}^{local}}{\Sigma} \tag{1.92}$$

where c_1, c_2, and c_3 are the principal axis components of the velocity dispersion tensor. At the low optical depth the largest principal axis points to the radial direction: at this limit $c_2/c_1 = c_y/c_x = 0.5$ and $c_3/c_1 = c_z/c_x \approx 0.65$. The vertical thickness is defined as

$$H = \sqrt{12 \overline{z^2}}, \tag{1.93}$$

which corresponds to the full thickness of a uniform layer with the same vertical dispersion as the simulated particle field. At $\tau_D \sim 0$, we have $H \approx 3c/n$. The vertical distribution can be further characterized by tabulating the vertical density profile of the simulation particles. This can be based on the locations of particle centers (Wisdom and Tremaine, 1988), or by $D_3(z)$ indicating the fraction of volume filled by particles as a function of z (Salo and Karjalainen, 2003). In particular, the filling factor at the equatorial plane $D_3(z = 0)$ (often denoted as $FF(0)$) is useful in comparison to theoretical treatments of dense rings (Araki and Tremaine, 1986; Araki, 1991).

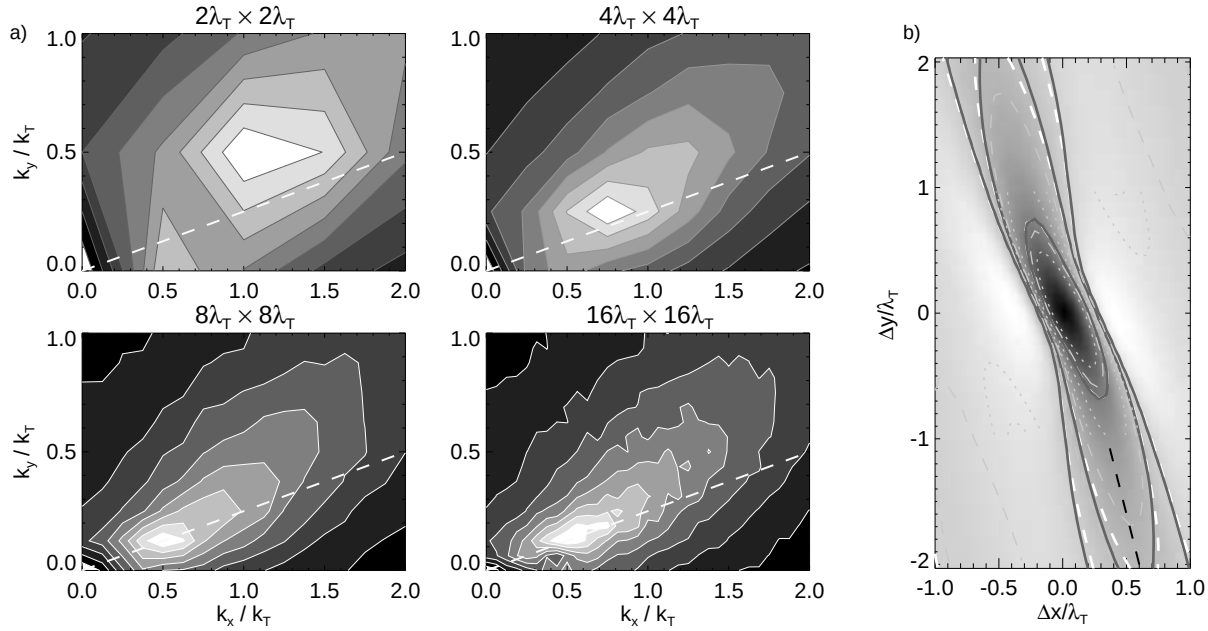

Figure 1.9 a) Fourier amplitudes $|\widetilde{\Sigma}_{l,m}|$ (see Eq. 1.94) in the simulations of Fig. 1.6, as a function of wavenumbers $k_x = 2\pi/\lambda_x$ and $k_y = 2\pi/\lambda_y$, where λ_x and λ_y are the radial and tangential wavelengths. The contours indicate amplitude levels 0.1,...0.9 times the maximum amplitude. The dashed line indicates $k_y = 0.25k_x$, corresponding to a pitch angle $\approx 14°$. In b) time averaged 2D auto-correlation functions of the same simulations (Eq. 1.95). Solid black and dashed white contours correspond to $16\lambda_T \times 16\lambda_T$ and $8\lambda_T \times 8\lambda_T$ simulations. Dashed black line indicates a 14° asymptotic pitch angle.

Other hydrodynamic quantities besides ν can also be extracted from simulations, like the radial heat conductivity and bulk viscosity, and the temperature derivatives of pressure, shear viscosity and energy dissipation. Such tabulations were made in Salo et al. (2001) for non-gravitating simulations assuming three different values of n_z/n. However, compared to the shear viscosity that can be extracted at the steady-state, these other quantities require that the system is perturbed and the measurement is carried out while the system relaxes back toward the uniform steady-state. Besides the technical difficulties involved, the exact relation of the derived quantities to their hydrodynamic interpretation is not clear. Mainly this is due to the non-isotropic velocity distribution (see Fig. 1.15e) following from particle's orbital motion around the planet. Such a distribution has more degrees of freedom than taken into account in hydrodynamical treatment. Nevertheless, such 'fitted' quantities applied to hydrodynamic stability analysis are quite successful in describing the viscous stability properties of larger-scale simulations (Schmidt et al., 2001; Schmidt and Salo, 2003). [4]

1.5.2 Characterization of self-gravity wakes

Examples of self-gravitating simulations were shown in Fig. 1.6 comparing snapshots from simulations with different sized calculation regions, while keeping other parameters the same. The snapshots indicated that the typical appearance of wake structure is evident even for calculation regions as small as $2\lambda_T \times 2\lambda_T$. However, comparison of gravitational viscosity (see Sect. 1.5) indicates that the strength of wakes is not fully developed unless a few times larger region, say $8\lambda_T \times 8\lambda_T$ is simulated. Similarly, the spacing and pitch angle of wakes is affected by the periodic boundaries: this is illustrated in Fig. 1.9a in terms of 2D Fourier decomposition of surface density[5]

$$\Sigma(x,y) = \Sigma_0 \sum_{l,m} \widetilde{\Sigma}_{l,m} \exp\left(i\frac{2\pi l}{L_x}x + i\frac{2\pi m}{L_y}y\right) \qquad (1.94)$$

where $|\widetilde{\Sigma}_{l,m}|$ gives the normalized amplitude corresponding to the radial and tangential wavelengths $\lambda_x = L_x/l$ and $\lambda_y = L_y/m$. In the $2\lambda_T \times 2\lambda_T$ simulation the peak amplitude occurs at $(\lambda_x, \lambda_y) = (1,2)\lambda_T$, but when the region is increased, (λ_x, λ_y) approaches $(2,8)\lambda_T$. This corresponds to a pitch angle $\tan^{-1}(\lambda_x/\lambda_y) \approx 14°$ between tangential direction and the the average direction of wakes.

The shape and orientation of the wakes is best illustrated in terms of 2D auto-correlation function of surface density,

$$\zeta_{2d}(\Delta x, \Delta y) = \frac{1}{{\Sigma_0}^2 A_0} \int\int \Sigma(x+\Delta x, y+\Delta y)\Sigma(x,y)\; dxdy. \qquad (1.95)$$

Taking the time average of this describes the typical density structure the particle sees around its location. It can be calculated directly from stored particle snapshots (e.g. Salo

[4] Isothermal hydrodynamical models which ignore bulk viscosity and temperature derivatives (Schmit and Tscharnuter, 1995) give a qualitatively correct picture of viscous behavior but fail to predict quantitatively the correct regime of viscous overstability.

[5] A convenient way to calculate the amplitudes is to perform 2D FFT on the system whenever the image regions happen to be aligned along the x-axis, which takes place $3\pi L_x/L_y$ times per orbit; at these instants FFT can be readily applied as Σ is periodic in both x and y.

1995), or more conveniently (e.g. Toomre and Kalnajs 1991) with the FFT, by taking the inverse Fourier transform of the squared density amplitudes, $\widetilde{\zeta}_{2d} = |\widetilde{\Sigma}_{l,m}|^2$. Figure 1.9b displays the auto-correlation functions, together with a line corresponding to 14° pitch angle.

1.5.3 Energy budget in local simulations

In the steady-state, the energy dissipation rate is connected to momentum flow by

$$\dot{E}_{diss} - sP_{12} = 0 \tag{1.96}$$

where $\dot{E}_{diss}$ is the energy loss in impacts, per unit time and unit area. Although this formula is valid for any shear flow, it is instructive to check how the formula actually arises in a local calculation region with periodic boundaries.

As mentioned in section 1.2, the quantity (Eq. 1.11)

$$E = E_{kin} + E_{pot} + E_{grav} \tag{1.97}$$

with

$$E_{kin} = \sum_i \frac{1}{2} m_i (\dot{x}_i^2 + \dot{y}_i^2 + \dot{z}_i^2) \tag{1.98}$$

$$E_{pot} = \sum_i m_i (ns{x_i}^2 + \frac{1}{2} {n_z}^2 {z_i}^2) \tag{1.99}$$

$$E_{grav} = -\frac{1}{2} G \sum_i \sum_{j \neq i} \frac{m_i m_j}{|\vec{r}_j - \vec{r}_i|} \tag{1.100}$$

is conserved along the orbital motion of particles. On the other hand, E changes both due to crossing of radial boundaries and due to impacts, via changes in E_{kin}, while both E_{pot} and E_{grav} remain unchanged[6].

The above expression for E_{kin}, using the actual velocities of the simulation particles, includes both, the kinetic energy associated to their random motions, E_{rnd}, and the kinetic energy associated to the systematic shear flow E_{shear},

$$E_{kin} = E_{rnd} + E_{shear} \tag{1.101}$$

where

$$E_{rnd} = \frac{1}{2} \sum_i m_i \vec{c}_i^{\,2} = \sum_i \frac{1}{2} m_i [\dot{x}_i^2 + (\dot{y}_i - s x_i)^2 + \dot{z}_i^2], \tag{1.102}$$

$$E_{shear} = \frac{1}{2} \sum_i m_i [2s x_i (c_y)_i + s^2 {x_i}^2] \tag{1.103}$$

Since E_{rnd}, rather than E_{kin} is of interest in many applications, we next look how it evolves in local simulations, subject to periodic boundaries, collisions, and gravitational forces.

In crossing of boundaries, the random velocity relative to mean flow is unaffected, so that ΔE_{rnd} remains constant, the change of E_{kin} being associated solely with E_{shear}. In an impact of a particle pair

$$\frac{1}{2}\delta(m_1 \vec{v}_1^{\,2} + m_2 \vec{v}_2^{\,2}) = \frac{1}{2}\delta(m_1 \vec{c}_1^{\,2} + m_2 \vec{c}_2^{\,2}) + s\,[m_1 x_1 (\delta c_y)_1 + m_2 x_2 (\delta c_y)_2]\,, \tag{1.104}$$

where the last term can be combined to $s\, m_2 (\delta c_y)_2 (x_2 - x_1)$, using the conservation of momentum (the subscript *2* labels the particle with the larger radial coordinate). Summing over all impacts during the time interval Δt we have

$$(\Delta E_{rnd})^{coll} = \Delta E_{diss} - s \sum_{impacts} m_> (\delta c_y)_> \Delta x_>. \tag{1.105}$$

To obtain the change of E_{rnd} due to self-gravity and orbital motion, we use Eqs. (1.97) and (1.101) to write

$$\begin{aligned} E_{rnd} &= E - E_{grav} - E_{pot} - E_{shear} \\ &= E - E_{grav} - E_z \\ &- \sum_i m_i [(ns + \frac{1}{2} s^2) {x_i}^2 + s x_i (\dot{y}_i - s x_i)] \end{aligned} \tag{1.106}$$

where

$$E_z = \frac{1}{2} \sum_i m_i {n_z}^2 {z_i}^2 \tag{1.107}$$

denotes the potential energy associated with vertical motions. Since E is conserved during orbital motion, the change of E_{rnd} during time interval Δt equals

$$(\Delta E_{rnd})^{orb} = -(\Delta E_{grav} + \Delta E_z) - \int_t^{t+\Delta t} \sum_i m_i \Big[(2ns + s^2) x_i \dot{x}_i + s\dot{x}_i (\dot{y}_i - s x_i) + s x_i (\ddot{y}_i - s \dot{x}_i) \Big] dt. \tag{1.108}$$

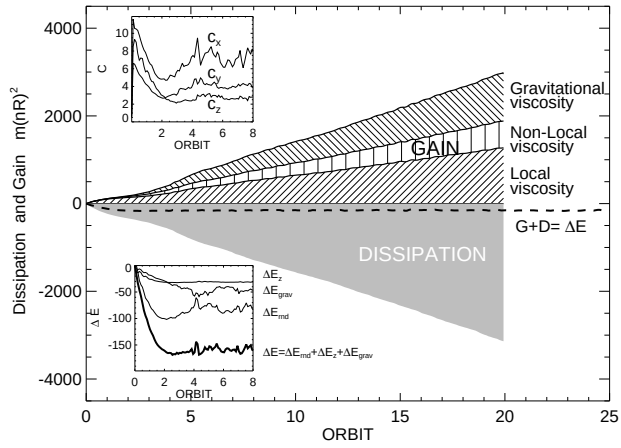

Figure 1.10 Energy balance in the $4\lambda_T \times 4\lambda_T$ simulation of Fig 1.6. Different contributions to viscous gain are shown separately: in the steady-state they balance the collisional dissipation. The small negative net value of the cumulative sum of gain and dissipation (G+D, dashed curve) equals the change in the total energy ($\Delta E = \Delta E_{rnd} + \Delta E_{grav} + \Delta E_z$) when the system settled toward steady-state values from an initially "hot" state: the upper insert shows the random velocity components, and the lower insert the various components of energy change. The energies are shown in units of $m(nR)^2$, where m is the total mass of simulation particles.

[6] Assuming that gravitational forces are constructed using the nearest image pairs, in which case the distances $|\vec{r}_i - \vec{r}_j|$ are not affected.

Substituting $\ddot{y} = -2n\dot{x}_i + (F_y)_i/m_i$ from the equation of motion, where $(F_y)_i/m_i$ is the y-component of the gravitational force felt by particle i, and taking into account that $c_x = \dot{x}$,

$$(\Delta E_{rnd})^{orb} = -(\Delta E_{grav} + \Delta E_z) - s\Delta t\left\langle \sum_i m_i (c_x)_i (c_y)_i + \sum_i x_i (F_y)_i \right\rangle \quad (1.109)$$

Adding $(\Delta E_{rnd})^{coll}$ and $(\Delta E_{rnd})^{orb}$,

$$\Delta E_{rnd} = \Delta E_{diss} - \Delta(E_{grav} + E_z) - s \sum_{impacts} m_> (\delta c_y)_> \Delta x_> - s\Delta t\left\langle \sum_i m_i (c_x)_i (c_y)_i \right\rangle - s\Delta t\left\langle \sum_i x_i (F_y)_i \right\rangle \quad (1.110)$$

Clearly, the summation in the last term in the right-hand side can be arranged to a form involved in the formula for gravitational viscosity Eq. (1.89), while the two other sums correspond to non-local and local viscosities. Dividing by Δt and A_o thus gives

$$\dot{E}_{rnd} + \dot{E}_{grav} + \dot{E}_z = \dot{E}_{diss} - sP_{xy} = \dot{E}_{diss} + s^2\eta \quad (1.111)$$

where the total viscous gain $-sP_{xy}$ consists of local, nonlocal and gravitational viscosity contributions

$$P_{xy} = {P_{xy}}^{local} + {P_{xy}}^{nl} + {P_{xy}}^{grav} \quad (1.112)$$

In the steady-state the left hand side of Eq. (1.111) is zero, leading to the anticipated result in Eq. (1.96).

An example of energy balance in simulations is shown in Fig. 1.10 for a system that starts with a velocity dispersion exceeding the steady-state value. Initially both $\dot{E}_{rnd}$ and $\dot{E}_z$ are negative as the system cools and flattens down toward steady-state. Also the negative contribution of gravitational energy increases when the particles collect to dense wakes. In steady-state, the left-hand side of Eq. (1.111) vanishes and the rates of viscous gain and dissipation balance each other exactly. Thus, we can obtain the viscosity of the system by calculating $\dot{E}_{diss}$ in steady-state by N-body simulation (Salo et al. 2001, Tanaka et al. 2003, Yasui et al. 2012).

1.6 Advanced computational techniques

1.6.1 Finding Collisions

For hard sphere collisions, where collisions are treated as discrete events, there are two main ways of dealing with them. One is to model each collision in order based on the time when it should happen (e.g. Trulsen, 1972; Wisdom and Tremaine, 1988; Salo, 1991; Richardson, 1994; Lewis and Stewart, 2000, 2003). A second is to advance particles, check if they are overlapping, and adjust their positions based on when the collision should have occurred (Rein and Liu, 2012). This latter option can be faster as it is trivial to determine if particles are currently overlapping, but it isn't currently clear what impact there is on results from not resolving and handling collisions in the order they occur.

The simplest case for finding the collision time for two particles is to approximate their relative motion with a second degree Taylor polynomial, using the particle positions, velocities, and accelerations at the current time t_0. Denoting $\delta\vec{r}(t) = \vec{r}_j(t) - \vec{r}_i(t)$, we may write

$$\delta\vec{r}(t) = \delta\vec{r}(t_0) + \delta\dot{\vec{r}}(t_0)(t - t_0) + \frac{1}{2}\delta\ddot{\vec{r}}(t_0)(t - t_0)^2 \quad (1.113)$$

The impact time t is found by setting $|\delta\vec{r}(t)| = R_i + R_j$. Squaring both sides, keeping terms quadratic in time, and rearranging gives

$$\left(\delta\dot{\vec{r}}(t_0)^2 + \delta\vec{r}(t_0) \cdot \delta\ddot{\vec{r}}(t_0)\right)(t - t_0)^2 + 2\delta\vec{r}(t_0) \cdot \delta\dot{\vec{r}}(t_0)(t - t_0) + \delta\vec{r}(t_0)^2 - (R_i + R_j)^2 = 0 \quad (1.114)$$

If the roots of this quadratic equations are complex, there is no collision. Otherwise, the smaller non-negative root for $t - t_0$ gives the approximative time of the next collision. The collision time can then be iteratively improved to correspond to the full accuracy of the orbital calculations.

1.6.2 Collision Pair Searching

The process of finding the collision time for particles can be expensive, and for that reason, should only be done for pairs of particles that actually have a chance of colliding during the current time step. The computational problem of finding pairs of particles that collide in hard-sphere simulations has a number of similarities to calculating gravitational forces. The brute force approach of checking every particle against every other particle is an $O(N^2)$ operation that is easy to code, but which is unacceptably slow for larger simulations. Gravity calculations can be done faster by approximating the force from particles at a distance. For collisions, one can simply ignore pairs of particles that are too far away and could not collide during a certain interval of time.

Salo (1991) used an approach where they kept lists of neighbors for each particle. Collision searches only had to run through the neighbor lists, and those lists only had to be updated occasionally. This speeds things up significantly for the actual searching process, but building the neighbor lists is still an $O(N^2)$ operation. For simulations with 10^7 or more particles, any $O(N^2)$ operation will be prohibitively expensive, even if it only has to be done very rarely. To get around this, one can use data structures that allow the entire process to be done in $O(N)$ or $O(N \log N)$ time.

1.6.2.1 2-D Grid

The simplest approach is to make a 2-D grid of lists. Rings are remarkably flat, so for any simulation of reasonable size, the radial and azimuthal extent of the particle distribution will be much larger than the vertical extent, and the use of a grid that does resolve vertical separation is unnecessary. The grid can be built in $O(N)$ time if one has a size for each grid cell. The size of the grid cells can be selected so that searches only need to extend out a fixed number of grid cells from the one a particle is located in. Only having to search immediate neighbor cells is ideal in a number of ways. To

make this safe, the grid cell size must not be smaller than the search radius of

$$R_{search} = 2R_{max} + A\,c\,\Delta t, \tag{1.115}$$

where R_{max} is the maximum particle radius, A is a small constant on the order of 5, c is the 1-D velocity dispersion, and Δt is the time step used in the simulation. The ideal grid size depends on many elements in the simulation code, and must be determined empirically, but it is possible for sparse grids with several times as many grid cells as there are particles to be optimally efficient.

The fact that the search radius depends on Δt (Eq.1.115) has an interesting effect. For gravity, one uses the longest time step that is numerically accurate because the total run time scales as $T/\Delta t$, where T is the total time being simulated. The run time of a collision simulation includes a $T/\Delta t$ factor for the number of time steps, but the amount of work done in a time step scales as R^2_{search}. Since R_{search} is proportional to Δt, this means that there is a competing component in the run time that scales as Δt, which will tend to make shorter time steps more optimal. Based on the details of the code and the simulated system, there will be an optimal value for Δt that minimizes the total run time. Note that the optimal value can change during a simulation as the system changes due to formation of structures like gravity wakes or perturbations from moons.

The building and use of the grid are both O(N) operations, so the time required to process collisions using a grid scales at O(N), assuming that the scaling is increasing the size of the simulation cell when running a larger simulation. Scaling the problem up in ways that increase the particle density, such as using smaller particles for higher resolution, can lead to increases in the number of particles in the search radius. This tends to alter the ideal value of Δt, and the overall scaling of run time with number of particles gets more complex.

1.6.2.2 Collision Trees

If the simulation is using a tree to calculate gravitational forces, one can use the same data structure to find potential collision pairs. The nodes in the tree have to be augmented with some additional information beyond what is needed for gravity calculations to help with finding collisions. This includes bounds for the particles below that node, velocity dispersion below that cell, and the maximum particle size below that cell. While the grid has the advantage of O(1) access time, the search area is basically fixed by the grid cell sizes, which are constant over the full grid. The tree has O($logN$) access time, but in many situation it can get a significant boost from the fact that the search radius from Eq. (1.115) can use local values in the tree. This can be a tremendous benefit when the simulation has a small number of much larger particles, such as in moonlet simulations. It also helps when gravity wakes and aggregates form, as the particles in the wakes have small local velocity dispersion.

1.6.3 Handling Collisions

The collisions need to be handled locally in proper time order as one collision can prevent or alter a later collision. The initial search for potential collisions will produce all the collisions that would occur during the time step assuming that all particles remained on their initial trajectories. These potential collisions can be placed on one or more priority queues so that they can be handled in the order of when they should occur. The term "potential collision" is used here intentionally, as these might not wind up being actual collisions. During the search, there is no a priori way of knowing if a given potential collision will be an actual collision or not, so they are simply all added to the appropriate priority queue. The determination of whether a collision actually occurs only happens when it is taken off of the priority queue and handled in the manner described in section 1.3. When that happens, the velocities of the two particles involved change, so all future potential collisions involving those two particles should no longer be considered.

That last requirement places some constraints on what data structures are optimal. For most applications, the optimal priority queue is based on a binary heap. However, because elements move around fairly randomly in memory as part of the binary heap operations, the act of finding an element to remove it later is O(N), which is unacceptable when you have to check for subsequent potential collisions after every collision is processed. Other standard priority queue data structures like Fibonacci heaps have actual nodes, which can be threaded through with links that allow one to find the potential collisions involving any particular particle in O(1) time. Due to the nature of collisions, this O(1) performance can also be achieved using a bucket priority queue where again each node is threaded through with links to other potential collisions that involve the same particle. Assuming that collisions are roughly uniformly distributed in time, and that the number of collisions from one time step to the next is fairly consistent, the bucket priority queue can provide a fairly simple structure with optimal performance.

After a collision is processed and the subsequent potential collisions involving those particles have been removed, new potential collisions must be identified for each of the two particles using whatever data structure is being used for efficient searches. Any that are found between the time of the current collision and the end of the time step are added to the appropriate priority queue. This process continues until the priority queues are empty, at which point all particles can be advanced to the end of the time step.

1.6.4 Parallelizing Collisions

Modern computers require simulations to be run in parallel to take full advantage of the hardware. The parallelism comes in several different forms: multiple threads on a single machine, multiple processes across machines or in a single machine, as well as utilizing GPUs and other co-processors.

Clusters of reasonably inexpensive servers became popular as a high performance computing platform in the 1990s.

To take advantage of this, programs need to support multiprocessing with message passing between machines. The way ring simulations work on these systems differs a bit based on the details of the network connections. The PKDGrav code (Stadel et al., 2002), which has been modified to do rings simulations, breaks the simulation region up across machines using the tree structure. It requires low-latency network interconnects to work efficiently as the machines communicate frequently. This is because machines communicate during the time step when they get to a point in the calculation that requires information from other machines. Caching schemes help to reduce the frequency of communication, but because of the frequency of communication, standard Ethernet connections, which typically have high latency, do not work well with this code.

A less flexible approach was developed by Lewis and Wing (2002) that can only divide the simulation region along the azimuthal direction. This method sends additional information, including adjacent particles and parts of the tree used for gravity calculations, at the beginning of each time step so that no communication has to occur during a time step. Using that additional information, each machine can run independently of the others for the duration of a time step. This makes it possible to use higher latency interconnects without suffering a significant speed reduction.

Beginning around 2005, nearly all workstation and server class processors began to include multiple cores. As of the time of this writing, it is not uncommon for these machines to have 20+ cores. This has made it important to use multithreading, in addition to multiprocessing. In multithreading, multiple threads share the same memory space and can work simultaneously. The fact that collisions have a natural ordering causes a challenge for multithreading. Solving this challenge using a single shared collision queue per process was explored in Lewis and Massingill (2006) and Lewis et al. (2009). Not all collisions have to be handled in time order, only those that are spatially close to one another, because the "sound speed" of the medium limits how far information can propagate through the medium during a time step. Collisions that are spatially separated can be processed out of order as long as they are far enough apart that the outcome of one couldn't alter the inputs of another.

Even more recently, graphics processors (GPUs) have become highly programmable, and are now being used broadly to accelerate calculation intensive computations such as gravitational calculations (Belleman et al., 2008). The applicability to ring simulations is less clear, and work in this area is still in an early stage. The primary challenge is the dependence on ordering. Even soft-sphere methods often use variable time step integrators where the order in which particles are processed is significant, and hard sphere methods generally require nearby collisions to be handled in proper time order. Some work has been done in the area of hard sphere collisions on GPUs. The primary adjustment is the use of many small priority queues, which are better suited to the GPU hardware instead of a single, more complex, priority queue (Langbert and Lewis, 2014).

1.7 Survey of simulation results

This Section collects simulation examples illustrating the intrinsic local dynamics of planetary ring systems. We start by discussing the simplest case of identical, non-selfgravitating particles, and demonstrate how the characteristics of the system's steady-state, e.g. the frequency of impacts and the velocity dispersion, depend on the coefficient of restitution and particle size. We show that the simulation results are consistent with heuristic hydrodynamical estimates. Particles' spin rotation, induced by surface friction and irregularities, is also briefly examined. We then proceed to systems with a distribution of particle sizes, and finally also include the particles' mutual self-gravity. Most of the non-gravitating simulations are made with the event-driven method (Salo, 1995) described on Sect. 1.3.1, since it is typically somewhat faster than the force method. The force code (Salo et al., 2001) described in Sect. 1.3.2 is used in the self-gravitating simulations of this section.

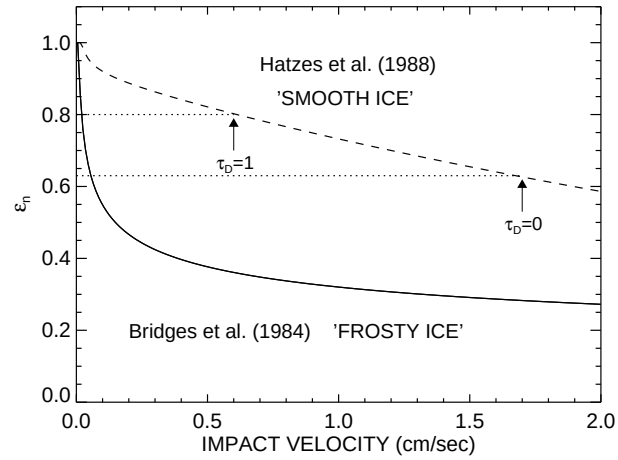

Figure 1.11 Two velocity-dependent elasticity models describing laboratory measurements of icy particles. The curve labeled "frosty" is for frost-covered ice (Bridges et al., 1984) , $\epsilon_{\rm n}(v_n) = 0.32(v_n)^{-0.234} < 1$, while the curve "smooth" refers to particles with compacted-frost surfaces (Hatzes et al., 1988) , $\epsilon_{\rm n}(v_n) = 0.90e^{-0.22v_n} + 0.01{v_n}^{-0.6}$. The normal component of impact velocity v_n is expressed in cm/sec. The Bridges et al. (1984) model can also be written as $\epsilon_{\rm n} = (v_n/v_c)^{-0.234}$, with $v_c = v_B = 0.0077$ cm/s.

Our main goal is to understand how the dynamic viscosity varies with surface density, and how this relation depends on particles' physical properties. As mentioned above, this $\eta(\Sigma)$ relation is crucial for the large-scale viscous stability properties of the particle ensemble. For non-gravitating systems the surface density is replaced with optical depth and dynamic viscosity then corresponds to $\eta = \nu\tau_D$. Two models (Fig 1.11) for velocity-dependent coefficient of restitution are systematically compared, corresponding to laboratory measurements made by Bridges et al. (1984; "frosty" ice) and Hatzes et al. (1988; "smooth" ice). The former model, with a steeper drop of $\epsilon_{\rm n}$ with impact velocity leads to an energy balance where the velocity dispersion corresponds

to ring vertical thickness $H \sim 10$ meters, (when assuming 1 meter ring particles), while the latter model implies a much hotter multilayer ring with $H \sim 100$ meters: these two models serve to illustrate the uncertainty in ring particles' elastic properties.[7] The viscosity versus density relation is constructed from small-scale simulations whose radial size is smaller than the shortest unstable wavelength so that no viscous perturbations can grow. It turns out that the two models predict drastically different viscous behavior: viscous instability in the case of thick rings and overstability in the case of flattened rings. Indeed, when the size of the simulation system is made sufficiently large both viscous instabilities and overstabilities can be directly verified in simulations (see Sect. 1.8).

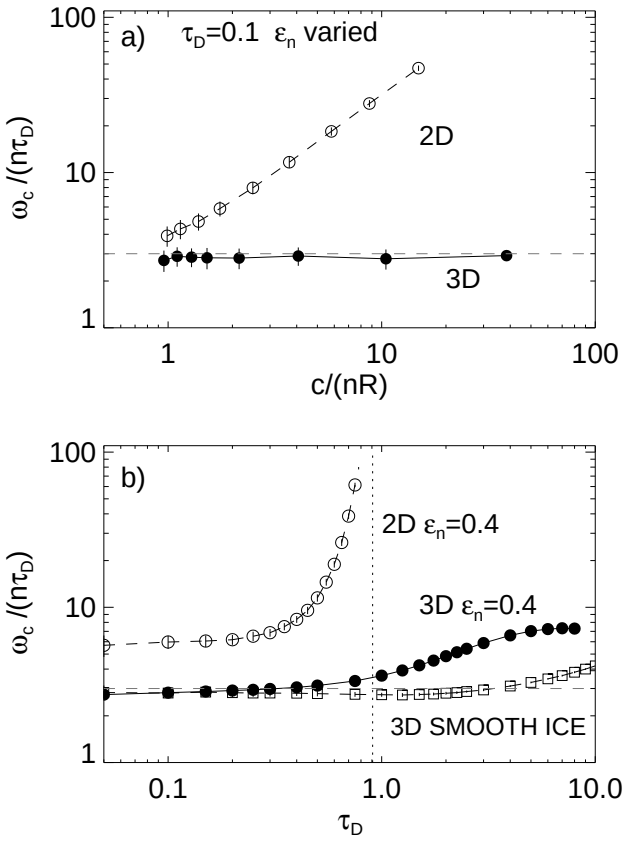

Figure 1.12 Impact frequency ω_c in 3D and 2D non-gravitating simulations, normalized to $n\tau_D$. In a) simulations with fixed $\tau_D = 0.1$ are compared as a function of velocity dispersion c, normalized to nR; the points correspond to steady-state values in simulations with different constant coefficients of restitution. In b) ω_c as a function of optical depth for simulations with constant $\epsilon_n = 0.4$ (circles) and using the Hatzes et al. (1988) velocity-dependent ϵ_n (see Fig 1.11). The vertical line indicates the $\tau_{D\max}$ for 2D systems.

[7] Unless otherwise indicated, the nongravitating simulations are performed for the Saturnocentric distance $a = 100\,000$ km. In the case of constant ϵ_n the distance is irrelevant as all results are expressed scaled to particle size R and angular frequency n.

1.7.1 Simulations of non-selfgravitating systems

1.7.1.1 Impact frequency

The ring system rapidly establishes an energy balance where the collisional dissipation is compensated by the viscous transfer of energy from the systematic orbital motion to random motions (Sect. 1.5.3). The time scale to reach this steady-state is determined by the frequency of particles' mutual impacts, ω_c. As expected, the impact frequency increases proportional to optical depth τ_D. An important peculiarity of the dynamics of dilute non-gravitating rings is that the steady-state ω_c is practically independent from the velocity dispersion. This results from the partitioning of vertical and horizontal random motions via impacts. Thus for example an increase in velocity dispersion, which in itself would enhance ω_c, is compensated by a corresponding vertical thickening and thereby reduced space density.[8] Analytic treatments taking into account the anisotropic distribution of impact directions and a Gaussian vertical profile (e.g Hämeen-Anttila, 1978), indicate

$$\omega_c \sim 3n\tau_D \sim 20\tau_D \text{ impacts/orbit}, \tag{1.116}$$

The independence of ω_c on velocity dispersion is illustrated in Fig. 1.12a, together with the approximation of Eq. 1.116 (dashed line). For comparison, the figure also shows ω_c in a 2D simulation where the motion of particles is limited to the central plane. In this case no adjustment between velocity dispersion and space density is possible and the explicit velocity dispersion dependence in ω_c is retained. As discussed in Salo and Schmidt (2010) this leads to fundamental differences in the viscosity versus density relations and thus the stability properties of 2D and 3D simulation systems.

The linear dependence of ω_c on τ_D breaks down for flattened systems ($\epsilon_n = 0.4$, yielding $H/R \sim 1$) when $\tau_D \gtrsim 1$, in which case the particles' own volume limits the free space available for motion (Hämeen-Anttila 1978). Similarly in a 2D system the impact frequency increases dramatically when the maximum 2D packing limit (maximum $\tau_D = \pi/\sqrt{12} \approx 0.907$ for identical particles) is approached. On the other hand, for a hot 3D multilayer ring ("smooth" ice, $H/R \gg 1$) the simple approximation holds quite well even for $\tau_D > 1$.

1.7.1.2 Establishment of Local Energy balance

Figure 1.13 displays the time evolution of the velocity dispersion c in simulations with different elasticity models. For a constant ϵ_n sufficiently close to unity c increases exponentially with time, and clearly no steady-state is achieved[9]. A

[8] The basic formula is $\omega_c \propto N_3 c_1 \sigma_c$, where N_3 is the volume number density, c_1 is the 1-dimensional velocity dispersion and σ_c the collisional cross-section: $\sigma_c = 4\pi R^2$ assuming identical particles with radius R. The volume number density $N_3 \approx N_2/H$, where $N_2 = \tau_D/(\pi R^2)$ is the surface number density and H the vertical thickness. Due to collisional coupling of horizontal and vertical motions, $c_z \sim c_1$, while due to orbital motion $H \propto c_z/n$. The explicit N_3 and c_1 dependencies thus cancel out, leading to the formula 1.116,

[9] These simulations must be carried out with the instantaneous impact method, since the force method would require impracti-

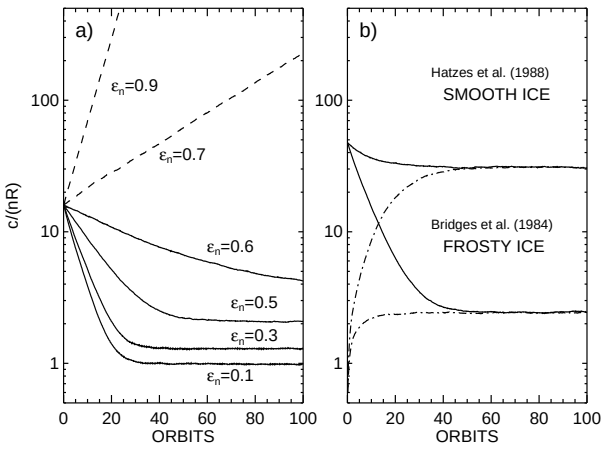

Figure 1.13 a) Evolution of velocity dispersion in simulations with different constant coefficients of restitution $\epsilon_{\rm n}$, for $\tau_D = 0.1$. The critical value $\epsilon_{\rm n} \approx 0.65$ separates the thermally stable (solid) and unstable (dashed) systems. (b) Simulations with two velocity dependent elasticity models of Fig. 1.11, starting from different initial states. Now the system attains a steady-state with the final velocity dispersion depending on the $\epsilon_{\rm n}(v_n)$ relation: the "smooth" ice model with a shallower drop of elasticity with v_n leads to a much hotter steady-state than the "frosty" ice model where $\epsilon_{\rm n}$ drops very fast with v_n.

constant $\epsilon_{\rm n}$ closer to zero leads to an exponential drop until c levels at a few times nR, corresponding to a few particle diameter thick ring. On the other hand, in the case of $\epsilon_{\rm n}(v_n)$ the steady-state depends on the functional form of the relation. The Bridges et al. (1984) model ("frosty" ice) leads to a flattened system very similar to $\epsilon_{\rm n} \approx 0.5$, whereas the Hatzes et al. (1988) model ("smooth" ice) leads to a multilayer ring. Fig 1.13b also illustrates the rapid time scale of evolution: here the system forgets the initial conditions in roughly 50 orbital periods, which for the used $\tau_D = 0.1$ corresponds to about 100 impacts/particle.

The above velocity evolution can be qualitatively explained with a simple heuristic description of the energy balance between dissipation and viscous gain (see Stewart et al., 1984; Schmidt et al., 2009). According to Eq. (1.111), the rate of kinetic energy change/unit mass is

$$\dot{E}_{rnd}/\Sigma + \dot{E}_z/\Sigma = \dot{E}_{diss}/\Sigma + s^2\nu \qquad (1.117)$$

Inserting the Keplerian shear rate $s = -\frac{3}{2}n$ and averaging the energy dissipation in individual impacts (Eq. 1.43; keeping just the $\epsilon_{\rm n}$ contribution, and absorbing the term $\dot{E}_z$ which relates to vertical flattening into $\dot{E}_{rnd}$), we can write

$$\begin{aligned} \frac{1}{2}dc^2/dt &= -k_1\,\omega_c\,c^2(1-{\epsilon_{\rm n}}^2) \\ &+ \frac{9}{4}n^2\Bigg[\underbrace{k_2 c^2\frac{\omega_c}{{\omega_c}^2+n^2}}_{\nu_{local}} + \underbrace{k_3\,\omega_c R^2}_{\nu_{nl}}\Bigg], \end{aligned} \qquad (1.118)$$

cally small T_{dur} for such dynamically very hot simulations, in order to keep $\xi_{max} << R$; see Eq. (1.60).

where the viscosity has been written as a sum of local and nonlocal contributions, and k_1, k_2, k_3 are all constants of the order of unity. The basic expression for local viscosity is $\nu_{local} = \omega_c\lambda^2$, where λ is the radial mean free path between impacts. In the high impact frequency regime the impacts limit the mean free path to $\lambda \sim c/\omega_c$ while for low ω_c an upper bound is set by the amplitude of epicyclic excursions, $\lambda \sim c/n$. Combining these estimates (Goldreich and Tremaine, 1978b) leads to the form in Eq. (1.118). For the non-local term the λ is set equal to the particle radius R.

The Eq. (1.118) describes qualitatively quite well the simulated behavior for a given elasticity of particles. In particular, if the system is very hot, $c/(nR) \gg 1$, the nonlocal gain term can be ignored. In this case both the gain and dissipation terms in the right hand side are proportional to c^2. Thus, no balance is possible unless $\epsilon_{\rm n}$ equals a critical value $\epsilon_{\rm cr}$, which (approximating $\omega_c \sim n\tau_D$) depends on the optical depth via the well-known Goldreich-Tremaine formula

$$(1-{\epsilon_{\rm cr}}^2)(1+{\tau_D}^2) = \frac{9k_2}{4k_1} \approx 0.61. \qquad (1.119)$$

If the constant $\epsilon_{\rm n} > \epsilon_{\rm cr}$, velocity dispersion increases continuously, as the dissipation is too weak to balance the local viscous gain. Similarly, if the constant $\epsilon_{\rm n} < \epsilon_{\rm cr}$, then dissipation exceeds the local viscous gain, leading to reduced c. The eventual steady-state is determined by the nonlocal gain implying a final $c \propto nR$. According to Eq. (1.119), $\epsilon_{\rm cr} \approx 0.65$ for $\tau_D \to 0$, in good agreement with the low τ_D simulations of Fig. 1.13. In the case of velocity dependent $\epsilon_{\rm n}$, the behavior is different, since the effective value of $\epsilon_{\rm n}$ depends on the average impact velocity $\sim c$. In the limit $\nu_{local} \gg \nu_{nl}$ (equivalent to $c \gg nR$), the steady state c would be adjusted to a value that yields $\epsilon_{\rm eff} = \epsilon_{\rm cr}$, where $\epsilon_{\rm eff}$ is the weighted mean of $\epsilon_{\rm n}(v_n)$ in impacts.

Figure 1.14 shows the Goldreich-Tremaine $\epsilon_{\rm cr}$ as a function of τ_D, delineating the thermally stable ($\epsilon_{\rm n} < \epsilon_{\rm cr}$) and unstable ($\epsilon_{\rm n} > \epsilon_{\rm cr}$) regimes. When τ_D is increased, less and less dissipation is needed for a thermally stable state to exist, so that $\epsilon_{\rm cr}$ approaches unity. This follows from the weakening of the local contribution to viscous gain, due to reduced mean free path λ as τ_D increases. Similarly, in the case of a reduced central shear rate, the $\epsilon_{\rm cr}$ would rise toward unity in order to compensate for the less effective viscous gain (for example $\epsilon_{\rm cr} \approx 0.85$ at $\tau_D \to 0$ for a flat rotation curve with $s = -n$; dashed line in Fig. 1.14).

Also shown in the Fig. 1.14 are mean values of $\epsilon_{\rm n}$ measured from simulations. Open symbols show simulations which lead to a dynamically hot steady-state with $c \gg nR$, thus mimicking the conditions leading to Eq. (1.119). In this case the agreement with theoretical approximation is quite obvious. For comparison, filled circles show mean $\epsilon_{\rm n}$ in simulations which lead to a steady-state with $c/(nR)$ not far from unity: in this case both local and nonlocal viscous gains are important, and the steady-state dissipation rate is larger (mean $\epsilon_{\rm n}$ closer to zero) than implied by the Goldreich-Tremaine formula which takes into account only the local viscous gain.

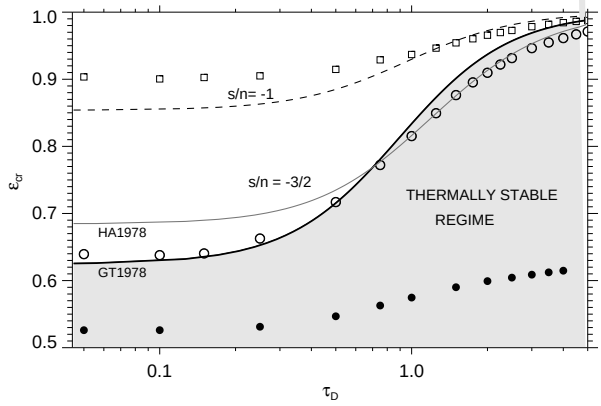

Figure 1.14 Thick solid line is the Goldreich-Tremaine $\epsilon_{\rm cr}(\tau_D)$ relation; thin solid line is the $\epsilon_{\rm cr}$ from (Hämeen-Anttila, 1978). Systems with constant $\epsilon_{\rm n} < \epsilon_{\rm cr}(\tau_D)$ (shaded region) flatten toward a stable near-monolayer state, while those with $\epsilon_{\rm n} > \epsilon_{\rm cr}(\tau_D)$ disperse via growing random velocities. Dashed line shows an approximate critical curve for a flat velocity field with $s/n = -1$ (obtained by replacing 9/4 with 1 in 1.119). Open symbols indicate effective mean values of $\epsilon_{\rm n}$ in dynamically hot simulations with $c/(nR) \gg 1$ (Bridges-type elasticity formula with $v_c = 100 v_B = 0.77$ cm/sec). For comparison, solid symbols indicate effective $\epsilon_{\rm n}$ in simulations with the original Bridges elasticity law. Note that the effective mean of $\epsilon_{\rm n}$ depends on how impacts are weighted (Salo, 1987b); here we use $\epsilon_{\rm eff} =< \epsilon_{\rm n}(v_n) {v_n}^2 > / < {v_n}^2 >$.

1.7.1.3 Steady-state as a function of optical depth

Figure 1.15 collects the various steady state properties as a function of τ_D, for the above two $\epsilon_{\rm n}(v_n)$ models. As mentioned earlier, the main difference between the models is the about 10-fold larger velocity dispersion for the "smooth" ice model at the low τ_D regime. This follows from the shallower slope in the $\epsilon_{\rm n}(v_n)$ relation, indicating that on the average much faster impacts are needed to yield the required dissipation rate. When optical depth increases, there is a strong drop in the c: this results from the above mentioned reduced local viscous gain: energy dissipation rate adjust by reducing the average impact velocities. This was illustrated in Fig. 1.11 by indicating the effective $\epsilon_{\rm n}$ values a hot system adjusts to when $\tau_D = 0$ and $\tau_D = 1$, implying a factor ~ 3 difference in average impacts velocities - this corresponds to the drop of c in Fig. 1.15a. For the "frosty" ice model there is hardly any change of c with τ_D: this is because the nonlocal gain term dominates for all $\tau_D' s$. For the "smooth" ice model the large drop in c reflects also in the strong flattening of the system and the drop of local kinematic viscosity.

The resulting viscosity versus density relations is quantified in Fig. 1.15d where the slope $\beta = d\log\nu/d\log\tau_D$ is displayed. Values of $\beta < -1$ correspond to negative $d\eta/d\tau_D$, the condition for *viscous instability* (collision-induced momentum flux tends to enhance density fluctuations; see Fig. 1.28 for a schematic illustration). In principle $\beta > -1$ indicates viscous stability (collisions smooth density fluctuations). However, particle simulations (Salo et al. 2001) and hydrodynamical models (Schmidt et al 2001) indicate that for $\beta \gtrsim 1$ the system may be prone to *viscous overstability*. The "smooth" ice elasticity model implies instability for $0.7 \lesssim \tau_D \lesssim 2$, while the "frosty" ice fulfills condition for overstability if $\tau_D \gtrsim 4$. We check these predictions in Section 1.8 with radially more extended simulations.

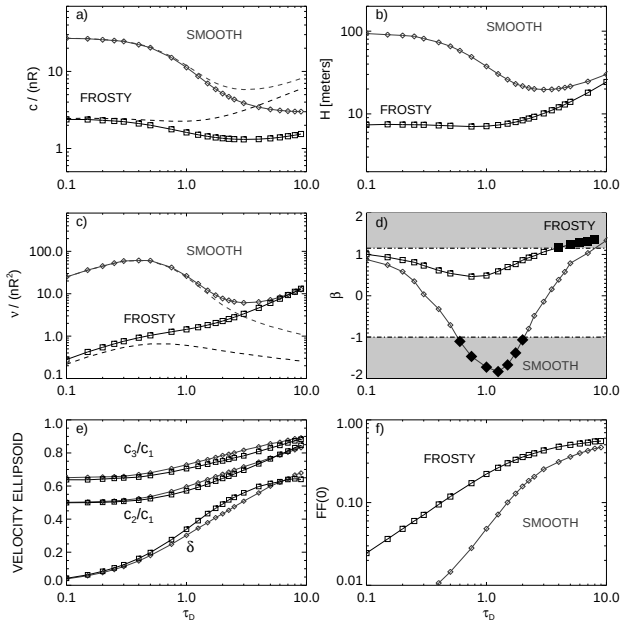

Figure 1.15 Steady-state quantities as a function of τ_D in simulations with velocity-dependent coefficient of restitution: a) the velocity dispersion c (dashed lines include also the contribution from nonlocal pressure, obtained by using $\hat{P}^{nl}$ in Eq. (1.92)), b) the vertical thickness H, c) the kinematic viscosity (dashed lines indicate the local contribution), and d) the slope of $\nu \propto {\tau_D}^{\beta}$ relation; the values of $\beta < -1$ predict viscous instability and $\beta \gtrsim 1$ viscous overstability (large filled symbols), e) shows the axial ratios of the velocity ellipsoid c_2/c_1 and c_3/c_1, and the angle δ (in radians) between the radial direction and the largest principal axis component, and f) the central plane volume filling factor $FF(0)$.

The lowermost row in Fig. 1.15 shows the shape and orientation of the velocity ellipsoid. Regardless of the large difference in the steady-state velocity dispersion, the principal axial ratios are not very different for the two models. At the limit $\tau_D \to 0$ the ratio $c_2/c_1 \to 0.5$ for both models, being determined solely by the systematic gradient in the Keplerian velocity field. On the other hand, the ratio c_3/c_1 depends somewhat on the effectivity of collisions in transferring energy from horizontal to vertical motions: this ratio is smaller in the case of more inelastic models yielding flatter systems. With increased τ_D, both c_2/c_1 and c_3/c_1 increase toward unity, though even at the largest studied value, $\tau_D = 10$, the velocity ellipsoid is still far from isotropic, even if the impact frequency already corresponds to over 100 impacts/orbital period. Likewise, the deviation δ of the longest principal axis from the radial direction, increases with τ_D, but is still below the hydrodynamical limit $\pi/4$ even at $\tau_D = 10$. Also shown in Fig. 1.15f is the central plane volume filling factor of the two models: for the

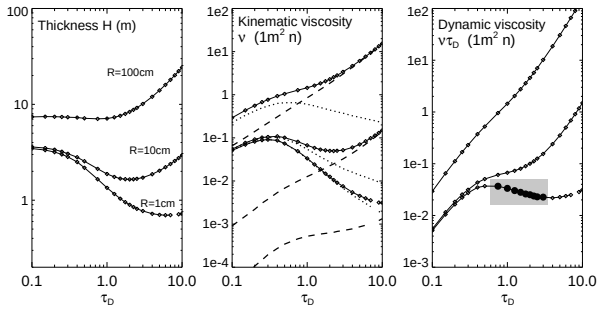

Figure 1.16 Dependence of a) geometric thickness H, b) kinematic viscosity ν , and c) dynamic viscosity $\eta = \nu\tau_D$ on optical depth τ_D, for the "frosty" ice model of the previous figure, but with different sized simulation particles. Large solid circles in c) indicate viscously unstable regime. In b) dotted and dashed lines indicate separately the local and nonlocal contributions.

"frosty" ice model, $FF(0)$ exceeds 0.2 for $\tau_D > 1$, while for the "smooth" ice model the same requires $\tau_D > 3$. Comparison to Fig. 1.12 indicates that this is roughly the regime where the nonlinearity of ω_c versus τ_D becomes apparent.

The above simulation survey for "frosty" and "smooth" elasticity models was done using 1 meter particles. In this case the "smooth" ice model was dominated by local viscosity at low τ_D, while with the "frosty" ice model nonlocal viscosity dominated at all τ_D's. Consequently, the former model is susceptible for viscous instability while the latter model is not. The basic reason for the instability is the rapid drop of steady-state c with τ_D, so that the dynamic viscosity of dense regions falls below that of low density regions. To remind that this behavior depends on the assumed particle size/elasticity model combination, Fig 1.16 compares the expected behavior of the "frosty" ice model when using particles sizes of 0.01, 0.10 and 1 meters. For a rough estimate of the relative importance of local and nonlocal contributions, note that at $\tau_D \to 0$ the local contribution tries to establish a state with a mean $\epsilon_n \approx 0.65$. For the Bridges et al. (1984) "frosty" ice model this corresponds to $c_{\rm local} \approx 0.05$ cm/s. On the other hand, the nonlocal contribution maintains a minimum $c_{\rm nonlocal} \approx nR = 0.2$ cm/sec with the nominal values of the previous figures. Thus with 1 meter particles $c_{\rm nonlocal}$ exceeds $c_{\rm local}$ by a factor of 4. However, with 1 cm simulation particles, $c_{\rm nonlocal} << c_{\rm local}$, and a strong drop in the steady-state c around $\tau_D \sim 1$ is again present. This would again lead to viscously unstable behavior for intermediate τ_D's.

1.7.1.4 Surface friction and Particle spins

In contrast to the normal coefficient of restitution, relatively few laboratory measurements exist for the friction of icy particles. According to Supulver et al. (1995) experiments, friction is weak, corresponding to tangential coefficient of restitution $\epsilon_t \sim 0.9$ in the case of relatively smooth ice surfaces at temperatures near 100 K. Nevertheless, to illustrate the possible effects of tangential friction we will briefly examine the whole allowable range of $1 \geq \epsilon_t \geq -1$, the latter extreme corresponding to the case where friction is able to reverse the tangential relative velocity in impact. Also, as discussed in Section 1.3, a consistent treatment of tangential friction between freely moving particles requires the inclusion of particle spins, which allows for energy transfer between random and rotational motions.

With the addition of frictional dissipation the steady-state velocity dispersion is reduced, the importance of this reduction depending on both the value of ϵ_t and the model for ϵ_n. This is illustrated in Fig. 1.17, comparing different ϵ_t values for "frosty" and "smooth" ice elasticity models. A fixed $\tau_D = 0.5$ is studied, but the relative effect is only weakly dependent on τ_D. The influence of ϵ_t is much more pronounced for the dynamically hot "smooth" ice model. This follows since the energy gain is then determined by the local viscosity. Inclusion of friction adds a dissipation term proportional to $\omega_c\ c^2(1-\epsilon_t^2)$ to Eq. (1.118), which means that the effective ϵ_n required for thermal balance moves closer to unity (Salo, 1987a,b; Araki, 1988, 1991; Ohtsuki, 2006a), thus indicating smaller c. The extra dissipation is most pronounced when ϵ_t is close to zero, leading to minimum of c near this value. On the other hand, a much smaller adjustment in c takes place when the balance is dominated by nonlocal viscosity ("frosty" ice model in the figure).

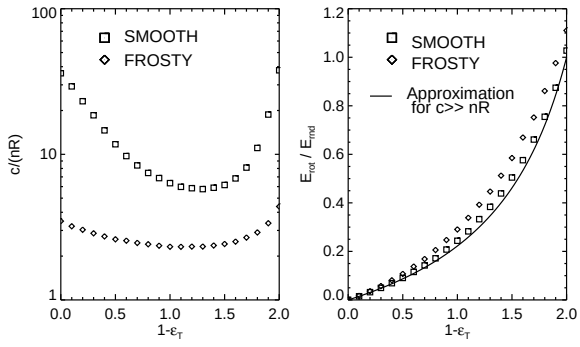

Figure 1.17 Effect of tangential coefficient of restitution ϵ_t on a) the steady-state velocity dispersion, and b) the energy ratio between the rotation and random velocities. The "frosty" and "smooth" ice elasticity models are compared for $\tau_D = 0.5$. The solid line is the theoretical approximation (Eq. 1.122) for the energy ratio in the limit $c \gg nR$.

Friction also induces spin motion of particles, which provides a feedback of energy from rotation to random motions (explains why the minimum of c is not exactly at $\epsilon_t = 0$). An equilibrium ratio between random and rotational energies is established when the net transfer equals zero. In practice the equilibrium implies that the dispersion of the surface velocities due to spins follows the dispersion of random velocities

$$\overline{(R\omega)^2} = k\ \overline{c^2}, \tag{1.120}$$

the proportionality factor k depending mainly on $\epsilon_{\rm t}$, and to lesser degree on $\epsilon_{\rm n}$ and τ_D. For a thick multilayer system the resulting equilibrium ratio of spin and random energies can be estimated by averaging the formula for the change of spin energy in individual impacts (Eq. 1.43), and by assuming an isotropic distribution of impact directions (should be valid in the case $c \gg nR$). For homogeneous spheres with

$$E_{rot} = \frac{1}{5} m({q_1}^2 + {q_2}^2 + {q_3}^2), \qquad (1.121)$$
$$E_{rnd} = \frac{1}{2} m({c_1}^2 + {c_2}^2 + {c_3}^2),$$

this yields (Salo, 1987a,b; Morishima and Salo, 2006)

$$\frac{E_{rot}}{E_{rnd}} \approx \frac{2(1-\epsilon_{\rm t})}{14 - 5(1-\epsilon_{\rm t})}, \qquad (1.122)$$

indicating that the energy ratio grows roughly proportional to $1-\epsilon_{\rm t}$ for $\epsilon_{\rm t}$ close to unity. At the limit $\epsilon_{\rm t} \to -1$ a total equipartition between rotation and random energies is predicted, in agreement with Shu and Stewart (1985). A similar result is obtained based on the three-body formalism for dilute rings (Ohtsuki, 2006a). Based on Fig. 1.17, the Eq. (1.122 holds quite well for the "smooth" ice model, especially in the limit $|\epsilon_{\rm t}| \to 1$ where the system has the largest velocity dispersion. For a more flattened system ("frosty") the simulated E_{rot}/E_{rnd} ratio is somewhat larger, reflecting the non-isotropic orientations of impact directions.

In addition to dispersion of spins, the particles also acquire a small residual mean vertical spin

$$\overline{\omega_z} \sim (0.2 - 0.3)n \qquad (1.123)$$

(Salo, 1987a,b; Richardson, 1994; Ohtsuki and Toyama, 2005; Morishima and Salo, 2006). This mean value is only weakly dependent on $\epsilon_{\rm t}$, $\epsilon_{\rm n}$ or τ_D. Since $\sqrt{\overline{\omega_z^2}}$ is proportional to c/R while $\overline{\omega_z}$ is independent of c, the ratio $\overline{\omega_z}/\sqrt{\overline{\omega_z^2}}$ can be significantly non-zero only for very flattened systems with small $c/(nR)$.

1.7.1.5 Surface irregularity/deviations from spherical shape

Almost all planetary ring simulations have assumed spherical particles. Mainly this is due to the technical simplifications it affords for detection and modeling of impacts. Also, the need for more complicated models is not obvious, since in many respects the effect of small deviations from spherical shape can be expected to average out, or to be accommodated by the uncertainties in the other model parameters like the elasticity of particles. However, irregular shape may have a significant contribution to particle spins, even if the tangential friction is small.

The effect of slightly non-spherical shape in promoting spin dispersion is illustrated in Figure 1.18, in terms of the energy ratio between rotation and random motions. The simulations use the irregularity model of Salo (1987a,b), where the normal vector of the local tangent plane of impact ($\vec{k}^*$) deviates slightly from the direction vector joining the particle centers ($\vec{k}$). In the figure the tilts γ_a and γ_b in Eq. (1.44) are assumed to get independent random values uniformly from the interval $[-f, f]$: the maximum studied value $f = 0.4$ corresponds to rms tilt angle $\sim 10^\circ$. Such a model is very efficient in inducing spin rotation even if the particles are almost frictionless: for example $\epsilon_{\rm t} = 0.99, f = 0.05$ (corresponds to $\sim 1^\circ$ rms tilt) gives about the same amount of spin rotation than $\epsilon_{\rm t} = 0.5$ for spherical particles with $f = 0$. Curiously enough, the energy ratio at the limit $\epsilon_{\rm t} \to 1$ is independent of f. The figure also shows an estimate of the equilibrium energy ratio (again setting the net transfer to zero; Salo 1987a), which is in good agreement with the simulation results,

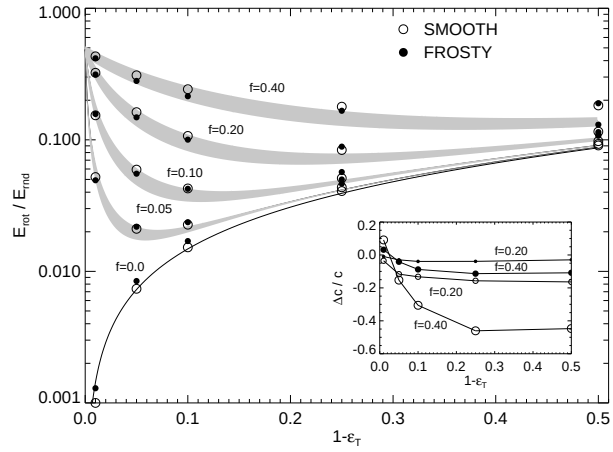

Figure 1.18 The effect of small irregularities/deviation from spherical shape on the energy ratio between rotation and random motions. Simulations with different f (the maximum local tilt of the impact plane, see the text) are compared as a function of $\epsilon_{\rm t}$ for two $\epsilon_{\rm n}(v_n)$ models. The optical depth $\tau_D = 0.5$. The theoretical energy ratio for mass point systems, Eq (1.124) applies to a constant $\epsilon_{\rm n}$: the gray filled areas correspond to this approximation with $\epsilon_{\rm n} = 0.5 - 0.8$. The insert shows the relative change in velocity dispersion c compared to the case $f = 0$. Two values of f are compared (larger symbols $f = 0.4$, smaller symbols $f = 0.2$).

$$\frac{E_{rot}}{E_{rnd}} = \frac{2}{7} \frac{\frac{2}{3} f^2(\epsilon_{\rm t} + \epsilon_{\rm n})(1 + \epsilon_{\rm n}) + \frac{1}{2}(1-\epsilon_{\rm t})^2}{(1-\epsilon_{\rm t}) + \frac{2}{3} f^2(\epsilon_{\rm t} + \epsilon_{\rm n}) - \frac{5}{14}(1-\epsilon_{\rm t})^2}. \qquad (1.124)$$

The theoretical estimate is for a constant $\epsilon_{\rm n}$, but the dependence on $\epsilon_{\rm n}$ is weak (see Fig. 1.18) This agrees with the fact that the simulated E_{rot}/E_{rnd} are very similar for both studied $\epsilon_{\rm n}(v_n)$ models. At the limit $\epsilon_{\rm t} = 1$ this approximation predicts $E_{rot}/E_{rnd} = \frac{2}{7}(1 + \epsilon_{\rm n}) \sim 0.5$.

Irregularity also affects the equilibrium velocity dispersion, the effect depending on $\epsilon_{\rm t}$ and $\epsilon_{\rm n}$ (see the insert in Fig.1.18). In the case of a hot system ("smooth" ice $\epsilon_{\rm n}(v_n)$ model), the reduction in c for $f = 0.4$ is close to 50% for $\epsilon_{\rm t} < 0.8$. However, for $\epsilon_{\rm t}$ very close to unity, irregularity may also slightly increase c due to feedback of energy from rotation (Salo 1987b). For a cool system ("frosty" ice $\epsilon_{\rm n}(v_n)$ model) the effect of irregularity, like that of friction, is much smaller.

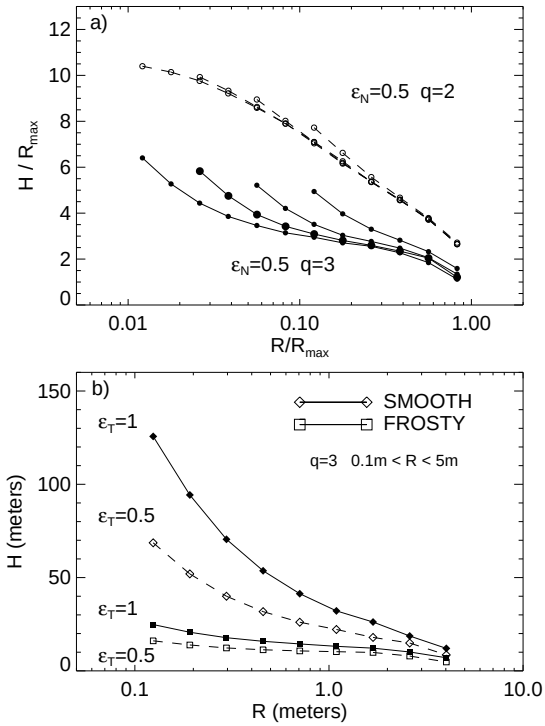

Figure 1.19 In a) the geometric thickness as a function of particle size in simulations with a power law size distribution, $dN/dr \propto r^{-q}$, for $R_{min} < R < R_{max}$. Different widths of the distribution, $W = R_{max}/R_{min}$, in the range $W = 4.64 - 100$ are compared, both for $q = 2$ and $q = 3$. In each case $\tau_D = 1.0$ and a constant $\epsilon_{\rm n} = 0.5$ is used. In b) two different $\epsilon_{\rm n}(v_n)$ models are compared for the same size distribution. Dashed lines show the effect of friction with $\epsilon_{\rm t} = 0.5$.

1.7.1.6 Size distribution

So far all our simulation examples have assumed identical particles. In the more realistic case of size distribution, the energy balance is modified by the energy transfer in impacts (and via gravitational encounters) from larger to smaller particles (see Stewart et al., 1984; Hämeen-Anttila, 1984). However, in contrast to gas dynamical systems this tendency toward energy equipartitioning is opposed by the inelasticity of impacts: simulations indicate that near equipartition is possible only for particle mass ratios below about 10 (Ohtsuki, 1992; Salo, 1992a). In practice the ratio between velocity dispersion of smallest and largest is less than about five, the maximum ratio depending on the functional form of the size distribution and the elasticity model.

Figure 1.19a shows how the vertical thickness H of different sized particles depends on the width $W = R_{max}/R_{min}$ and index q of the power-law size distribution with $dN/dR \propto R^{-q}$. A constant $\epsilon_{\rm n} = 0.5$ is used, in which case all simulation quantities scale with the assumed maximum particle size. Therefore, quantities normalized to R_{max} are shown. For $q = 3$ the maximum ratio in the vertical thickness of the bin of smallest and largest particles ($H_{\rm small}/H_{\rm large}$) depends only weakly on W, while for $q = 2$ it slightly increases with W. For $q = 2$ most of the mass is on the largest particles: consequently the influence of small particles on the largest particles is small and $H_{\rm large}$ is independent of W. For $q = 3$ each logarithmic size increment corresponds to same fraction of total mass, and increasing the width W pushes $H_{\rm large}$ down. The lower panel of Fig. 1.19 compares the two different $\epsilon_{\rm n}(v_n)$ models for $q = 3, W = 50, R_{max} = 5$m, emphasizing how the difference between small and large particles becomes stronger for hot systems. In terms of steady-state velocity dispersion, the $c_{\rm small}/c_{\rm large} \approx H_{\rm small}/H_{\rm large} \approx 10$ for the "smooth" model, and about 3 for the "frosty" ice. For comparison, for a constant $\epsilon_{\rm n} \to 0$, the $c_{\rm small}/c_{\rm large} \approx 1.5$. All simulations of Fig.1.19 have $\tau_D = 1.0$, but the results are only weakly dependent on τ_D (Salo 1992a).

The effect of friction on c is roughly the same on all particle size bins (dashed lines in Fig. 1.19b). Also the equilibrium dispersion of surface spin velocities, $\overline{(R\omega)^2}$ scales with c^2 of the size bin. The relatively weak dependence of c on R thus indicates that the spin dispersion $\sqrt{\overline{\omega^2}}$ is roughly inversely proportional to the particle radius. Therefore, small particles spin much faster than the large ones. This was also confirmed by N-body simulations of self-gravitating rings (Richardson, 1994; Ohtsuki, 2005; Ohtsuki and Toyama, 2005; Morishima and Salo, 2006). On the other hand, the residual mean spin is always a fraction of n independent of particle size. Therefore, while the mean spin of the largest particles can be significant compared to its dispersion, the spin axis of the smallest ones are always practically randomly distributed. For an illustration of progradely rotating large particles embedded in a population of randomly oriented small particles, see Salo(1987b).

1.7.1.7 Adhesive forces

Figure 1.20 displays an example of simulations with surface adhesion. The linear force model is combined with an extra constant attraction between impacting, slightly overlapping particles. With the nominal value $F_{adh} = F_o$ (second row), the critical impact speed v_{adh} which implies sticking in a pairwise impact is about 4-fold compared to the steady-state mean impact speed in the absence of adhesive force (uppermost row). Consequently, the particles experience quite rapid pairwise sticing, leading to small particle aggregates, roughly 4 times larger than individual particles (see the 2D autocorrelation plot in the right). In the successive frames, the increased F_{adh} leads to progressively larger aggregates. Note that the snapshots, corresponding to 30 orbital periods, already represent a new steady-state situation: due to shear the typical impact speeds between the aggregates (or between a free particle and an aggregate) increase when the aggregates grow, and consequently the sticking is eventually hindered when typical speeds approach the sticking threshold value. Note that the example uses parameter values which exaggerate the role of adhesion: the v_{adh} corresponds to sticking of cm-sized particles, while the simulation particles have 1 meter radius. Nevertheless, in real systems significant accretion of cm-size particles can be expected (Albers and Spahn, 2006).

Tremaine (2003) suggested that the B ring irregular structure could manifest a *shear-rate instability*, where the system

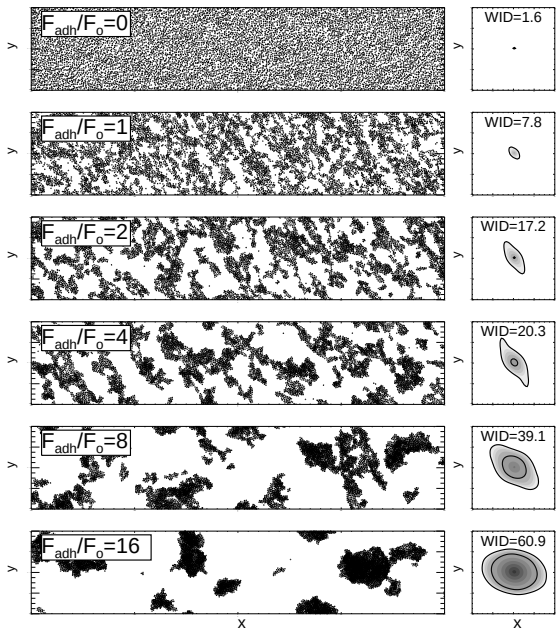

Figure 1.20 Influence of adhesive force in simulations. The linear force model is combined with a constant attractive force F_{adh} affecting between each impacting, slightly overlapping particle pair. The values of F correspond to those of Fig. 1.5. The optical depth $\tau_D = 1$ and $\epsilon_{\rm n} = 0.25$: with $F = 0$ the mean steady-state impact velocity for 1 m particles is $< g_n > \approx 0.04$ cm/sec. The critical velocity for sticking in the case $F_{adh} = F_o$ is 0.17 cm/sec. The left frames show snapshots of the simulation after 30 orbital periods, for $F_{adh}/F_o = 0, 1, 2, 4, 8, 16$: the size of the simulation region is $L_x \times L_y = 400R \times 80R$. The frames in the right display the 2D autocorrelation function of the same snapshot; the black contours corresponds to 10% and 100% overdensities. The labels indicate the full radial width (in particle radii) of the 10% overdensity region.

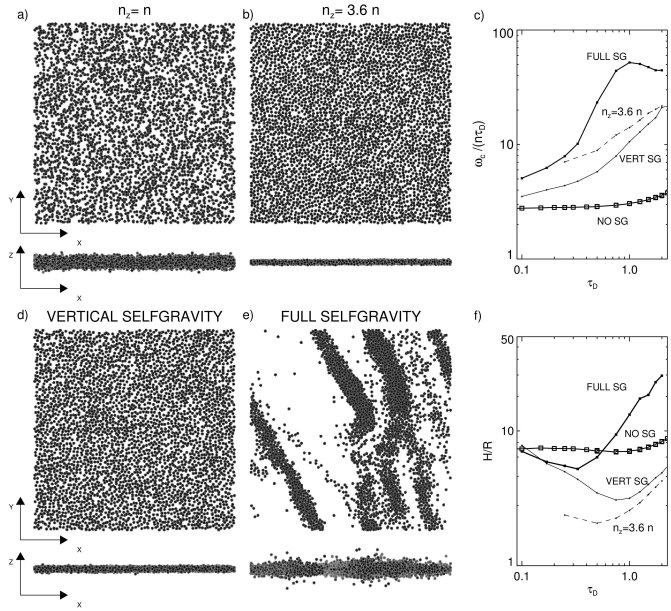

Figure 1.21 Snapshots from $2\lambda_T \times 2\lambda_T$ simulations with $\tau_D = 0.75$, using the "frosty" ice elasticity model. In the upper row non-gravitating simulations with a) $n_z/n = 1$ and b) $n_z/n = 3.6$. In the lower left, in d) the vertical component of self-gravity is self-consistently included, while e) the full self-gravity is taken into account. The internal density $\rho = 900 {\rm kgm}^{-3}$ which corresponds to $r_h = 0.82$ at the simulated Saturnocentric distance 100 000 km (see Eq. 1.129). Also shown in c) is the impact frequency (normalized by $\tau_D n$ and in f) the vertical thickness (averaged over the whole system) as a function of optical depth.

is divided into rigidly rotating zones, separated by zones where the shear-rate locally exceeds the Keplerian value. Such an instability could arise if the dynamic viscosity is a decreasing function of local shear rate. It was envisioned that this might be the case with sufficiently strong cohesive bonds between particles. In the simulations of Fig. 1.20 there is no signs of such instability: instead of forming radial zones with locally reduced shear rate, the system divides into irregular aggregates with roughly equal dimensions in radial and tangential directions (and slightly flattened in the vertical direction).

1.7.2 Self-Gravitating simulations

At low optical depth the main effect of self-gravity is through 2-body scattering in close binary encounters. Although they correspond to completely elastic impacts in the sense that the kinetic energy of the encountering pair is conserved, the deflection of the orbits during encounter leads to energy transfer from systematic to random motions. This extra heating increases c until it becomes roughly comparable to the 2-body escape velocity of the particles (Safranov, 1969; Hämeen-Anttila, 1978; Cuzzi et al., 1979). For larger surface densities, the collective effects become increasingly important. For example, in Saturn's dense B the vertical self-gravity may exceed the vertical component of the central force by a large factor (Wisdom and Tremaine, 1988). Nevertheless, then also the planar components of gravity need to be taken into account, leading to a strongly non-uniform density distribution.

1.7.2.1 Formation of self-gravity wakes

Figure 1.21 compares different ways to approximate ring self-gravity: using in b) the factor $n_z/n > 1$ to mimic the increased vertical field and in d) the self-consistently calculated F_z. Clearly, a right choice of $n_z/n > 1$ (depending on the surface density) would capture quite well the effects of vertical gravity: the flattening of the ring and the strongly enhanced impact frequency. However, with the inclusion of full self-gravity (Fig. 1.21e) the picture is completely different from that when only the vertical component of self-gravity is taken into account. The system now forms gravitational condensations which shear into elongated trailing density enhancements. Such structures, in the context of Saturn's rings, were first simulated in Salo (1992a). However, the phenomenon itself was envisioned already a few decades earlier, in the context of galaxy disks.

Toomre (1964) showed that a self-gravitating differentially rotating disk is locally unstable against the growth of ax-

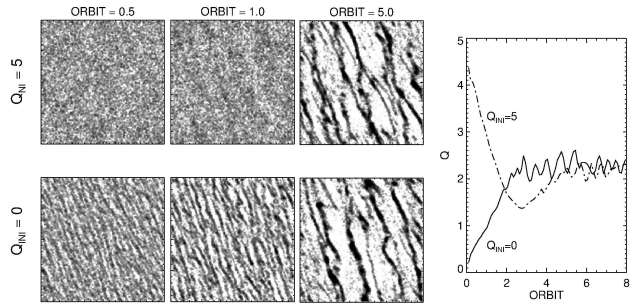

Figure 1.22 Establishment of statistical steady-state in $8\lambda_T \times 8\lambda_T$ simulations starting from a hot ($Q_T = 5$) and cold ($Q_T = 0$) uniform initial state. The parameters are $\tau_D = 0.5$, $r_h = 0.82$, $\epsilon_{\rm n} = 0.5$.

isymmetric disturbances if its radial velocity dispersion c_x falls below a critical value c_{cr}. The closeness to the stability boundary is measured by the Toomre Q_T parameter

$$Q_T = \frac{c_x}{c_{cr}} = \frac{c_x \kappa}{3.36 G\Sigma}. \qquad (1.125)$$

While $Q_T \geq 1$ guarantees stability against the growth of *axisymmetric* perturbations, already for $Q_T \lesssim 2-3$ the system is susceptible to the growth of local *non-axisymmetric* disturbances (Julian and Toomre, 1966; Goldreich and Lynden-Bell, 1965). Such a near-instability manifests as an emergence of trailing filamentary density enhancements just as those seen in the self-gravitating simulations. As was illustrated in Sect. 1.4, in a Keplerian velocity field such wakes form $\sim 15^0 - 20^o$ angle with respect to the tangential direction, and their radial separation is of the order of Toomre's critical wavelength

$$\lambda_T = 4\pi^2 G\Sigma/\kappa^2. \qquad (1.126)$$

Individual filaments are rapidly destroyed by shear, but new condensations are continuously generated. Due to enhanced densities and systematic motions associated with the wakes, the ω_c is even more strongly enhanced than in the case of vertical gravity (Fig. 1.21c). Also, the vertical thickness increases as the scattering by wakes more than compensates the flattening caused by the enhanced vertical field (Fig. 1.21f).

Figure 1.22 illustrates the role of wakes/impacts in establishing a "thermostat" which keeps the system near a constant Q_T regardless of the initial state of the system. In the case of stellar disks, the gravitational scattering accompanying the growing disturbances would heat the system so that the wakes are eventually suppressed. In the case of particulate rings, the collisional dissipation provides a physical regulating mechanism which makes it possible to reach and maintain a statistical steady-state with sufficiently low Q_T, so that new structures continuously emerge and dissolve in a timescale comparable to the orbital period. As emphasized by Toomre and Kalnajs (1991), the gravity wakes do not represent an instability in the sense that there would be a strict threshold for the emergence of the wakes - rather they manifest the enhanced reactivity of the selfgravitating disk whenever Q_T is sufficiently small. In particular, any small

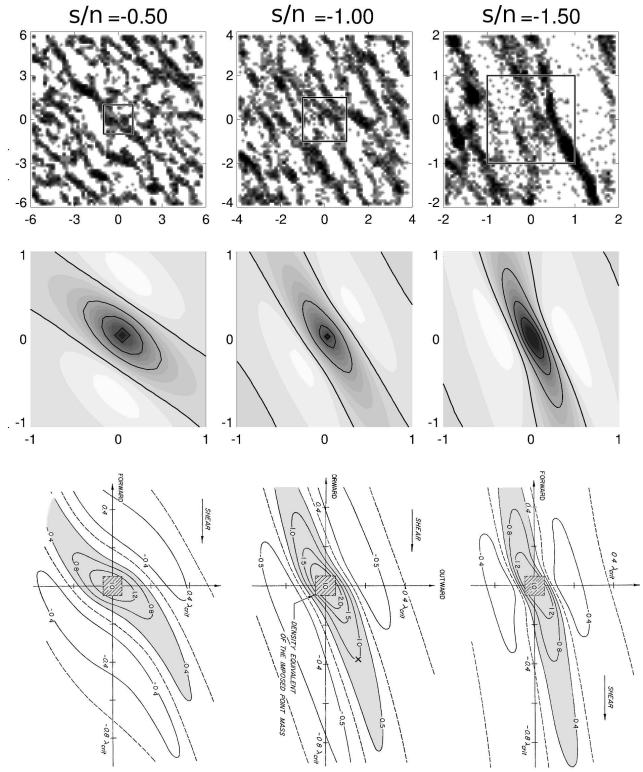

Figure 1.23 The upper row shows snapshots from simulation with different shear rates s: the physical width of the calculation region is fixed (~ 170 particle radii) and corresponds to $12, 8$, and $4\lambda_T$ for $s/n = -0.5, -1.0$ and -1.5. The middle row shows 2D auto-correlation plots from the same simulations, covering $2\lambda_T \times 2\lambda_T$. The lowermost row shows Julian-Toomre (1966) analytic calculations for the same shear rates of the wake response around an orbiting point mass-point: their graphs have been rotated to same orientation as our simulation plots. In the simulations $\tau_D = 0.5$, constant $\epsilon_{\rm n} = 0.5$, $r_h = 0.82$.

leading perturbation, while evolving into a trailing one due to shear, is significantly amplified by the interplay of gravity and differential rotation (the "swing amplification" mechanism (Toomre, 1981; Goldreich and Lynden-Bell, 1965).

The self-gravity structures seen in simulations can be interpreted as a superposition of numerous individual Julian and Toomre (1966) wakes, excited by each particle when other particles flow past it - this justifies the name ('wake') commonly adopted to the phenomenon. This identification is supported by the 2D auto-correlation analysis of the simulated structures (Toomre and Kalnajs, 1991; Salo, 1995; Salo et al., 2004). To further strengthen the argument, Fig. 1.23 compares auto-correlation functions from ring simulations with the Julian and Toomre (1966) theoretical calculations of the density response around an orbiting mass enhancement, performed for different central shear rates. The trend in the pitch angle of the density crest as a function of s/n is strikingly similar. Also as expected, the scale of structures is in all cases proportional to λ_T, which is different by a factor of 3 for the studied shear rates ($\lambda_T \propto (2s/n + 4)^{-1}$ according to Eqs. (1.6) and (1.126). A more quantitative compar-

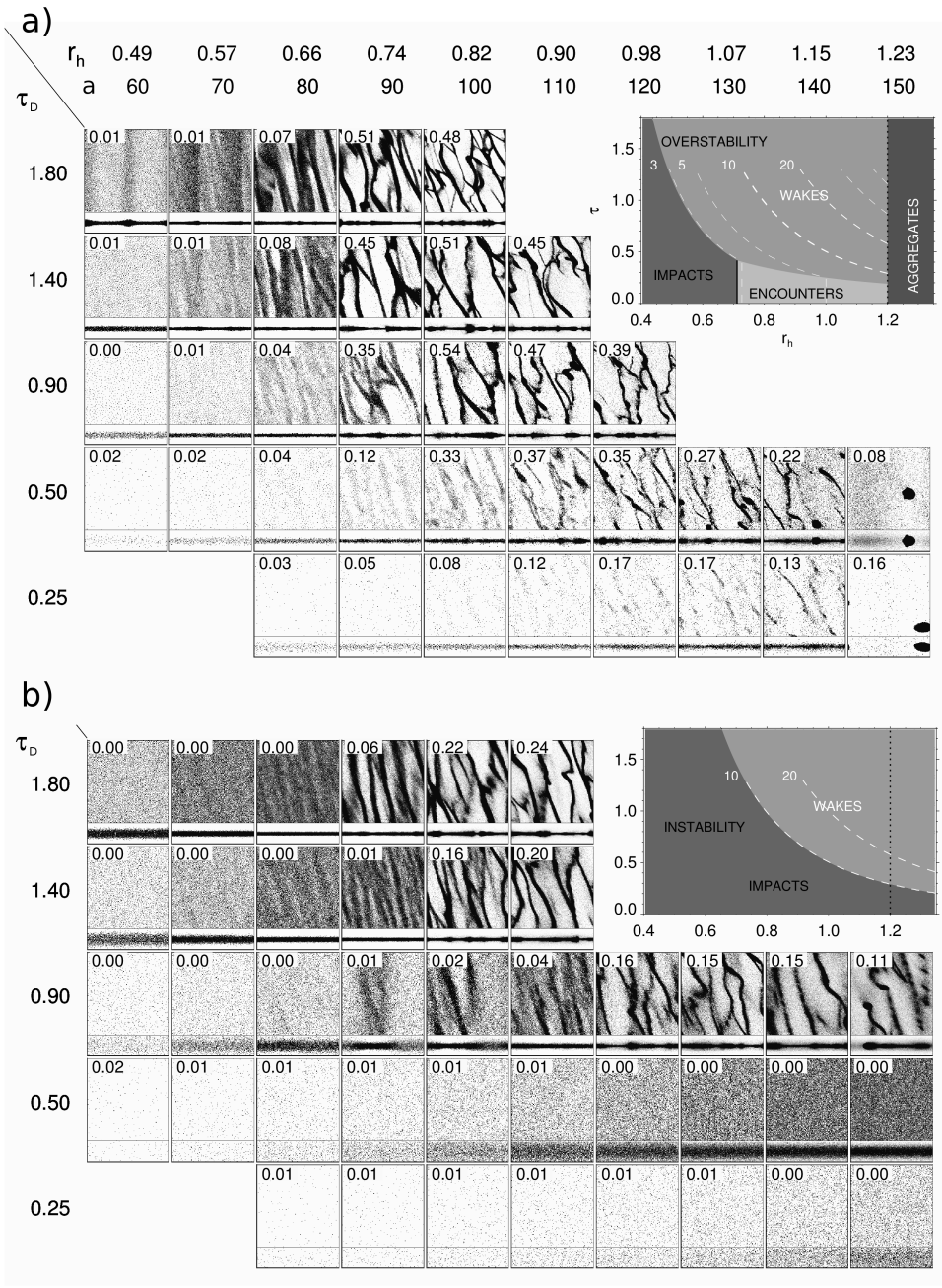

ison is not attempted, since the Julian and Toomre (1966) response-calculations assumed a fixed Q_T for the disk and did not account for the finite particle size - in simulations of Fig. 1.23 the velocity dispersions adjusts self-consistently to balance the dissipation and viscous gain.

1.7.2.2 Survey of self-gravity wakes

In the non-gravitating case the optical depth τ_D and the elasticity model determine the ring steady-state for a given particle size distribution (see Sect. 1.7). When self-gravity is included, just one new parameter is required to characterize both the pairwise and collective gravitational effects. This is the r_h parameter, the ratio of the mutual Hill-radius for

Figure 1.24 Survey of self-gravity wakes as a function of r_h and τ_D. The labels a indicate the Saturnocentric distance (in units of 1000 km) for particles with solid ice internal density: for other densities the distances scale $\propto (\rho/900\mathrm{kgm}^{-3})^{-1/3}$. The size of the simulation system is $4\lambda_T \times 4\lambda_T$, with $\lambda_T/R \approx 150\tau_D {r_h}^3$; the side view covers $4\lambda_T \times 1\lambda_T$. The number of simulation particles $N \approx 116 \cdot 10^3 {\tau_D}^3 {r_h}^6$. In a) the "frosty" ice and in b) the "smooth" ice elasticity model is used. The inserts sketch the regimes where various physical factors dominate, based on the estimates given in the text. The dashed curves indicate what is the radial velocity dispersion which corresponds to $Q_T = 2$. In a) the boundary between wakes and impacts is drawn at $c_r/(nR) = 3$, while in b) $c_r/(nR) = 10$ is assumed. Note the region $\tau_D \gtrsim 1$ and $r_h \lesssim 0.6$ in a) leading to viscous overstability (see Sect. 1.8.1). Similarly in b) simulations with $\tau_D = 0.9$, $r_h \sim 0.8$ show viscous instability (see Sect. 1.8.2). The numbers in the frames indicate the amplitude of azimuthal brightness asymmetry for the simulation (see Sect. 1.11.4).

a pair of particles to the sum of their physical radii,

$$r_h(\mu) = \frac{R_H}{R_1 + R_2} = \left(\frac{\rho}{3\rho_P}\right)^{\frac{1}{3}} \left(\frac{a}{R_P}\right) \frac{(1+\mu)^{\frac{1}{3}}}{1+\mu^{\frac{1}{3}}}, \qquad (1.127)$$

where ρ is the internal density of the particles, and $\mu = M_1/M_2 = (R_1/R_2)^3$ is their mass ratio. Here

$$R_H = ((M_1 + M_2)/3M_P)^{1/3} a \qquad (1.128)$$

is the radius of the Hill-sphere, inside which the pair's mutual gravity dominates over the tidal pull from the planet at the distance a. The M_p,R_p, and ρ_P are the mass, radius, and mean density of the planet. When r_h decreases, the particle pair extends more and more out from its Hill-sphere: $r_h = 0$ corresponds to the non-gravitating case, while if $r_h = 1$ the attraction between two synchronously rotating, radially aligned ring particles in contact equals the disruptive tidal force. For a pair of identical particles $\mu = 1$, and inserting the typical numerical values for Saturn's rings gives

$$r_h(\mu = 1) = \quad 0.82 \left(\frac{M_P}{5.69 \cdot 10^{26}\ \mathrm{kg}}\right)^{-\frac{1}{3}} \left(\frac{\rho}{900\ \mathrm{kgm}^{-3}}\right)^{\frac{1}{3}} \left(\frac{a}{100\ 000\ \mathrm{km}}\right). \qquad (1.129)$$

We will denote $r_h(\mu = 1)$ simply by r_h. For $\mu = 0$ or $\mu \to \infty$ (a test particle attached to surface of a large particle), the r_h would be a factor $2^{2/3} \approx 1.59$ larger. With the formula (1.129), the simulation results for a given r_h can be scaled to any other $\rho^{1/3}a$ combination.

To demonstrate that r_h is the only additional parameter needed to characterize self-gravity wakes.[10], we may write the Toomre critical wavelength and velocity dispersion as

$$\frac{\lambda_T}{R} = 48\pi\ \tau_D {r_h}^3, \qquad (1.130)$$

$$\frac{c_{cr}}{nR} = 12.8\ \tau_D {r_h}^3. \qquad (1.131)$$

Here we have assumed identical particles; in the case of a size distribution the numerical pre-factors would depend on dN/dR. Similarly, the minimum velocity dispersion maintained by gravitational encounters, $c_{enc} \sim v_{esc}$, where $v_{esc} = \sqrt{2GM/R}$ is the 2-body escape speed, can be expressed as

$$\frac{c_{enc}}{nR} = 4.9\ {r_h}^{3/2} \qquad (1.132)$$

Figure 1.24a depicts a simulation survey of wake structures for the "frosty" ice elasticity model. The strength of wakes increases when the optical depth τ_D, or the distance (measured with r_h) increases. The wakes get clumpier and eventually degrade into semi-permanent gravitational aggregates for $r_h \gtrsim 1.2$. Same takes place at low τ_D via pairwise accumulation. The exact boundary for aggregate formation depends on the elasticity of particles and also the particle size distribution (Salo, 1995; Karjalainen and Salo, 2004). The fact that $r_h > 1$ is required for stable aggregates to form is because not only shear, but also particle impacts and velocity dispersion act to destroy any forming condensations.

The insert in Fig. 1.24a sketches the parameter regimes where different factors (impacts, encounters, wakes) dominate the dynamics, based on the velocity dispersion this factor alone would be able to maintain (Salo, 1995; Ohtsuki and Emori, 2000). For the "frosty" ice model (or constant $\epsilon_\mathrm{n} \lesssim 0.5$) the minimum velocity dispersion due to impacts is

$$\frac{c_{imp}}{nR} \sim 2 - 3 \qquad (1.133)$$

Comparing to Eq. (1.132), we may expect that velocity dispersion is governed by gravitational encounters rather than by physical impacts for $r_h \gtrsim 0.7$. A rough criterion for the emergence of collective wake-structure is obtained by assuming that wakes become apparent whenever the minimum velocity dispersion drops below $c_{wake} = Q_T\, c_{cr}$ with $Q_T \sim 2$. According to Eqs. (1.131) and (1.133) this corresponds to $\tau_D {r_h}^3 \gtrsim 0.1$. In the insert figure the condition $c_{wake} > c_{imp}$ (and $c_{wake} > c_{enc}$) defines the sketched boundary between wakes and impacts (or wakes and encounters). The other dashed curves in the insert indicate where $Q_T = 2$ corresponds to $c/(nR) = 5, 10, 20$.

Figure 1.24b shows a similar survey, except with the "smooth" ice elasticity model. No wake structures are visible for optical depths $\tau_D = 0.25$ or $\tau_D = 0.50$ for any r_h, but for higher τ_D the picture is very similar to that in a). The reason for the suppression of wakes at low τ_D is the high velocity dispersion maintained by impacts alone: according to Fig. 1.15, we have $c/(nR) > 10$ for $\tau_D \lesssim 1$. In the inset figure the $Q_T = 2$ line corresponding to this c value is used to delineate the boundary between impacts and wakes. Now the velocity dispersion of the system is too high to allow for bound aggregates to form at any of the studied r_h values.

The wake structure is also affected by the particle size distribution (Fig. 1.25). For example, the average pitch angle increases when size distribution is included (Salo et al., 2004; French et al., 2007b; Michikoshi et al., 2015). Also, although the large particles still form distinct wakes, the overall contrast is reduced due to the more uniform distribution of small particles. This implies that at least in principle a system can exhibit dynamically significant wake structure, though it might be almost hidden in photometric observations (Salo et al., 2004).

1.7.2.3 Gravitational viscosity

The effect of gravity wakes on viscosity is depicted in Fig. 1.26. The upper row compares self-gravitating simulations with constant $\epsilon_\mathrm{n} = 0.5$ as a function of r_h and τ_D. For $\tau_D \gtrsim 0.5$ and $r_h \gtrsim 0.75$, the ν_{grav} contribution associated with the gravitational torques from inclined wakes becomes dominant (Daisaka et al., 2001; Tanaka et al., 2003). Also ν_{local} is strongly enhanced due to systematic motions associated with the wakes, whereas the ν_{nl} has less significance. The results of Fig. 1.26 agree with the trend originally found

[10] This is strictly valid only in the case of constant ϵ_n. If $\epsilon_\mathrm{n} = \epsilon_\mathrm{n}(v_n/v_c)$, with a scale parameter v_c, then the ratio nR/v_c which determines the relative magnitudes of local and nonlocal viscous gains (see Fig. 1.16) will depend on distance via n. However, for example for the "frosty" ice model this dependence is weak and the r_h scaling works well (see Karjalainen and Salo (2004)).

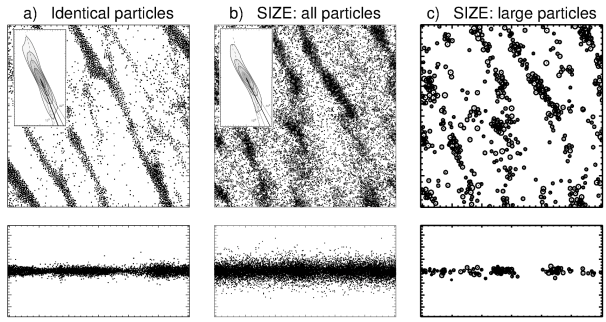

Figure 1.25 a) Identical particle simulation with $\tau_D = 0.5$, $r_h = 0.85$, using "frosty" particle elasticity model and $4\lambda_T \times 4\lambda_T$ calculation region. b) Simulation with same parameters, except having a $q = -3$ power-law size distribution with $R_{max}/R_{min} = 10$. c) Particles with $R > R_{max}/2 = 2.1$ m are shown separately: they comprise 30% of the optical depth and 55% of surface mass density. The inserts in a) and b) display 2D auto-correlations, indicating about 5° larger average pitch angle of wakes in the size distribution simulation.

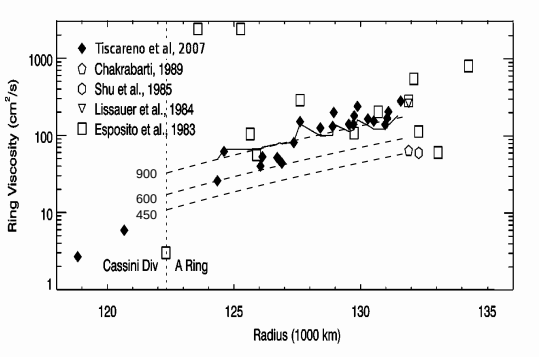

Figure 1.27 Various measurements of the A ring kinematic viscosity, based on damping of density waves (symbols). The thick solid line indicates the viscosity calculated from Eq. (1.134), using the surface densities measured for this distance, and assuming solid ice internal density for the particles. The dashed lines indicate viscosities from the same formula, using $\rho = 900, 600$, and 450 kgm^{-3}, and a fitted surface density (linear rise from 300 kgm^{-2} to 500 kgm^{-2} between 122, 000 km and 132, 000 km). Figure modified from Tiscareno et al. (2007).

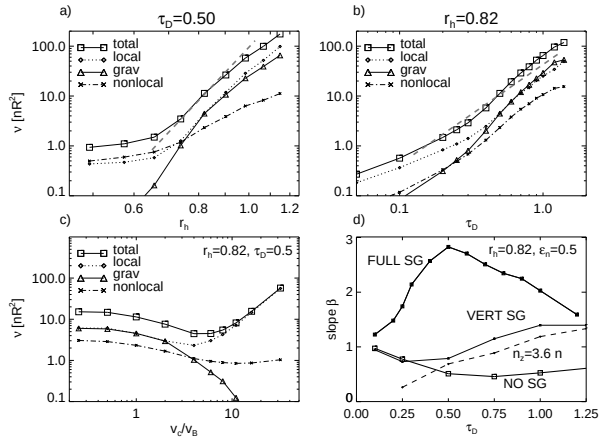

Figure 1.26 Comparison of various contributions to total viscosity, in a) as a function of r_h and b) as a function of τ_D. They are from a constant $\epsilon_n = 0.5$ simulations similar to Fig. 1.24. The light dashed gray lines in a) and b) indicate Eq. (1.134). In c) the viscosity as a function of scale parameter v_c in velocity- dependent elasticity model $\epsilon_n(v_n) = (v_n/v_c)^{-0.234}$: with $v_c = v_B = 0.0077 cm/s$ this corresponds to the Bridges et al. (1984) "frosty" ice model. Frame d) displays the slope of $\nu \propto {\tau_D}^\beta$ in simulations of frame b), reaching values $\beta \approx 2 - 3$ in selfgravitating simulations; also non-gravitating simulations and simulations including only the vertical self-gravity are shown.

in Daisaka et al. (2001),

$$\nu_{tot} \approx (\nu_{grav} + \nu_{local}) \approx 2\nu_{grav} \propto \frac{{r_h}^5 G^2 \Sigma^2}{n^3}. \qquad (1.134)$$

The Σ^2 ($\propto {\tau_D}^2$ in the figure) dependence is similar to the standard continuum fluid formula for spiral torques in galaxy disks (Lynden-Bell and Kalnajs, 1972), while the r_h dependence can be interpreted as an extra effect related to the finite size of particles: the smaller the r_h, the closer is the scale of wakes compared to physical size of particles (see Eq. 1.130). This limits the maximum contrast the wakes can attain as the density of wakes is limited by the internal density of particles. The estimates of Saturn's ring viscosity in Tiscareno et al. (2007), based on the damping of A ring satellite density waves are in good agreement with Eq. (1.134), provided that the internal density of particles is close to that of solid ice (see Fig. 1.27).

The slope of $\nu(\tau_D)$ relation is shown in more detail in Fig. 1.26d and also compared with non-gravitating simulations and to simulations including only the vertical component of self-gravity (compare to Fig. 1.21). With the inclusion of self-consistent vertical gravity the slope $\beta \gtrsim 1$ for $\tau_D \gtrsim 1$, which is higher than in the non-gravitating case ($\beta \approx 0.5$), but clearly smaller than with full-self-gravity ($\beta \approx 2$). Note that when using n_z/n to mimic vertical gravity, the value of β can be increased by choosing a larger enhancement factor.

Based on Fig, 1.24 it is clear that the gravitational viscosity depends strongly on the adopted elasticity model. In Fig.1.26c this is illustrated by comparing simulations with different $\epsilon_n(v_n)$ models, parameterized by the velocity scale factor in the Bridges et al, (1984) type elasticity law ("frosty" ice model has $v_c/v_B = 1$; the "smooth" ice model would correspond to $v_c/v_B \sim 30$). The more inelastic the impacts are, the larger is the contribution from gravitational viscosity. For the simulated $\tau_D = 0.5$, the gravitational viscosity is completely negligible for $v_c/v_B = 30$, in agreement with the total absence of wake structure in the simulations depicted in 1.24b. At the same time for very elastic impacts the local viscosity increases proportional to $(v_c/v_B)^2$. This follows as the system tries to establish a thermal balance with a mean elasticity whose value depends on the optical depth via the Goldreich-Tremaine formula. The resulting steady-state c is proportional to v_c and thus $\nu_{tot} \approx \nu_{local} \propto {v_c}^2$. Because of the opposite trends of ν_{local} and ν_{grav}, and the relatively insignificant role of ν_{nl}, the total viscosity has a minimum at intermediate $v_c/v_B \approx 5$.

1.8 Viscous instability and overstability

The Voyager and Cassini data have revealed an overwhelming amount of structure in Saturn's rings. Some of the structure is unambiguously connected to resonance perturbations by external satellites (in particular in the outer A ring), but the majority of the finest optical depth variations, extending down to shortest resolved length scales, are likely to have some internal origin.

Right after Voyager discoveries *viscous instability* was evoked to explain the intrinsic variations (Lukkari, 1981; Lin and Bodenheimer, 1981; Ward, 1981; Hämeen-Anttila, 1982). In this type of instability (see Fig. 1.28), the collisional flux of particles, proportional to dynamic viscosity $\eta = \nu\tau_D \propto {\tau_D}^{\beta+1}$, is directed toward density maxima (equivalent to $\beta < -1$). Thus any small density fluctuation is amplified by collisional diffusion, in contrast to a stable ring where diffusion smooths density variations. In the nonlinear limit the growth of fluctuations is saturated to a state where the flux from dense but dynamically cool ringlets is balanced by the flux from rarefied, dynamically hot regions. This model was soon discarded, mainly as the first laboratory measurements (Bridges et al., 1984) indicated too dissipative particles for the instability mechanism to work (Wisdom and Tremaine, 1988; Araki and Tremaine, 1986). Also, the observed structures do not quite agree with the predictions of simple instability models, according to which the ring should separate into high τ_D ringlets surrounded by almost empty gaps (Hämeen-Anttila, 1978).

Other alternatives for explaining the ring fine structure gained more attention, among them the possibility that dense rings might be viscously overstable (Borderies et al., 1985; Longaretti and Rappaport, 1995). In the axisymmetric *overstability* the radial particle flux is directed away from density maxima, like in a stable ring (see Fig. 1.28). However, the flux now increases so strongly with density (large β), that the system overshoots in trying to smooth the density variations: this leads to density oscillating with time. Although it appears unlikely that overstability could account for large scale structures in the densest rings (Latter and Ogilvie, 2010), there are clear indications of small-scale $\sim$ 100 meter axisymmetric oscillations in moderate τ locations in the rings (Colwell et al., 2007; Thomson et al., 2007; Hedman et al., 2014) likely to be related to such overstable oscillations.

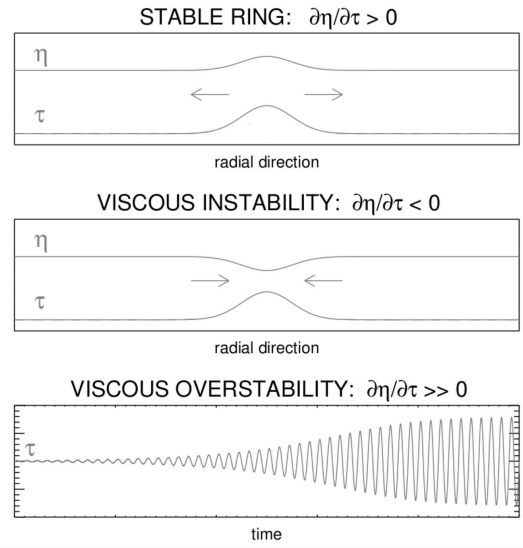

Figure 1.28 Schematic illustration of viscous stability properties. The radial mass flux is proportional to - $\partial\eta/\partial\Sigma$, where η is the dynamic viscosity and Σ is the surface mass density. This indicates that the ring tries to establish a locally constant η profile. In stable ring $d\eta/d\Sigma > 0$ so that local density fluctuation are smoothed, in contrast to $d\eta/d\Sigma < 0$ which leads to *viscous instability*. However, if $d\eta/d\Sigma \gg 0$ the suppression overshoots leading to periodic oscillations with amplitude growing with time until saturated at some finite value (*viscous overstability*). In case of non-selfgravitating system optical depth τ_D replaces Σ and η is obtained from kinematic viscosity as $\eta = \tau_D\nu$.

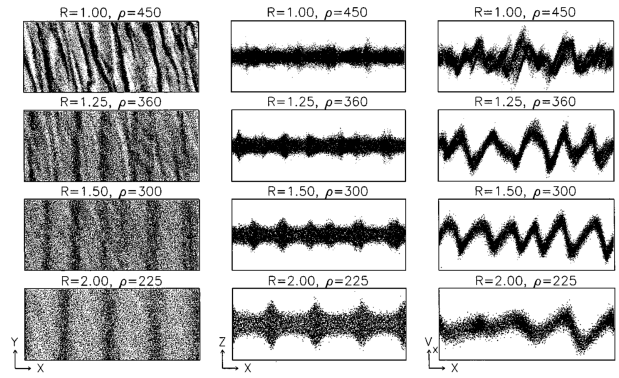

Figure 1.29 Snapshots from self-gravitating simulations for $\tau_D = 1.4$, "frosty" ice elasticity model, using a $10\lambda_T \times 4\lambda_T$ calculation region. The top and side snapshot of the system and the radial velocity profile after 50 orbital periods are shown, for four simulations with $\rho = 450, 360, 300, 225$ kgm^{-3}. For the Saturnocentric distance $a = 100\,000$ km these correspond to $r_h = 0.651, 0.605, 0.569, 0.517$, respectively. Figure from Salo et al. (2001).

1.8.1 Viscous overstability (Oscillatory instability)

Early hydrodynamical models for Saturn's rings predicted that practically any flattened ring system with $\beta \gtrsim 0$ should be overstable (Schmit and Tscharnuter, 1995, 1999), manifesting as axisymmetric oscillations in density and velocity components. The mechanism itself can be confirmed in direct N-body simulations (Fig. 1.29, Salo et al., 2001; Daisaka et al., 2001), which however indicate considerably more stringent conditions for the onset of overstability.

In non-gravitating simulations, and in simulations including vertical self-gravity, the condition (Salo et al., 2001; Schmidt et al., 2001)

$$\beta \gtrsim 1 \qquad \text{overstability condition (non} - \text{gravitating)}$$

seems to provide a sufficient condition for the onset of overstability, provided that the size of the system exceeds the shortest scale of overstable oscillations, about 100 particle radii. For example, in the non-gravitating simulations with

the "frosty" ice elasticity model have $\beta > 1$ if $\tau_D \gtrsim 4$ (Fig. 1.15d). Similarly, simulations where vertical self-gravity is approximated with $n_z/n = 3.6$, fulfill this condition for $\tau_D \gtrsim 1$ (Fig. 1.26d). Indeed, in both cases simulations with sufficiently large calculation regions lead to spontaneous growth of overstable oscillations (Salo et al., 2001).[11]

Transport coefficients derived from simulations with different values of n_z/n, in combination with improved hydrodynamical models (Salo et al., 2001; Schmidt et al., 2001), have been useful in analyzing the linear growth rates of oscillations, and also in allowing analytic treatment of saturation in weakly nonlinear case (Schmidt and Salo, 2003). Significant progress has also been made using the kinetic theory approach (Latter and Ogilvie, 2008). Recently, nonlinear hydrodynamical analysis (Latter and Ogilvie, 2009, 2010) has shown that the wavelength growth of overstable oscillations is limited via interactions of traveling wavetrains at a few hundred meter to kilometer range, the maximum scale increasing with β. The non-gravitating, very large-scale simulations in Rein and Latter (2013) confirm this, and also demonstrate the richness of structures that result from the non-linear interaction of such wavetrains.

However, it is still unclear what the overstability condition for a fully self-gravitating ring is. The simulations in Salo et al. (2001) indicate that self-gravitating systems may exhibit overstability for $\tau_D \gtrsim 1$, but *only if the wake-structure is not too strong*. For example, in the survey of Fig. 1.24a, overstability is seen only in the upper left corner with $r_h \lesssim 0.6$. For stronger wakes the overstability is clearly suppressed (see also Fig. 1.29), although the overstability condition for non-gravitating rings, $\beta \gtrsim 1$, should be satisfied with ample margin (see Fig. 1.26d). This suppression might be related to different phase and pitch angle of the velocity and density oscillations for overstability and wakes, combined with the fact that they occur at practically similar wavelength range. In any case, even an approximate analytic theory is missing, making fully self-gravitating numerical simulations indispensable for looking at the interplay of wakes/overstability.

As mentioned above Rein and Latter (2013) recently carried out simulations with radially very extended calculations regions (radial width even 50 km), facilitating the detailed study of interactions between non-linear wavetrains. However, these simulations use the $n_z/n > 1$ approximation, and it is not clear how realistically they describe self-gravitating rings. Fig. 1.30 compares this approximation with the fully self-consistently calculated gravity, in moderately large-scale simulations (radial width 2 km). In the former case the evolution is similar to Rein and Latter (2013) simulations, leading to formation of traveling wavetrains with increasing wavelengths, until a maximum scale of $\sim$ 400 meters is reached after about 1000 orbital periods. In the beginning several left and right traveling waves compete, but after about 500 orbits a single traveling mode starts to dominate. The amplitude spectrum indicates that no further wavelength evolution takes place during the span of the simulation (10000 orbits): the shorter modes represent the harmonics of the prevailing mode, related to its non-sinusoidal waveform.

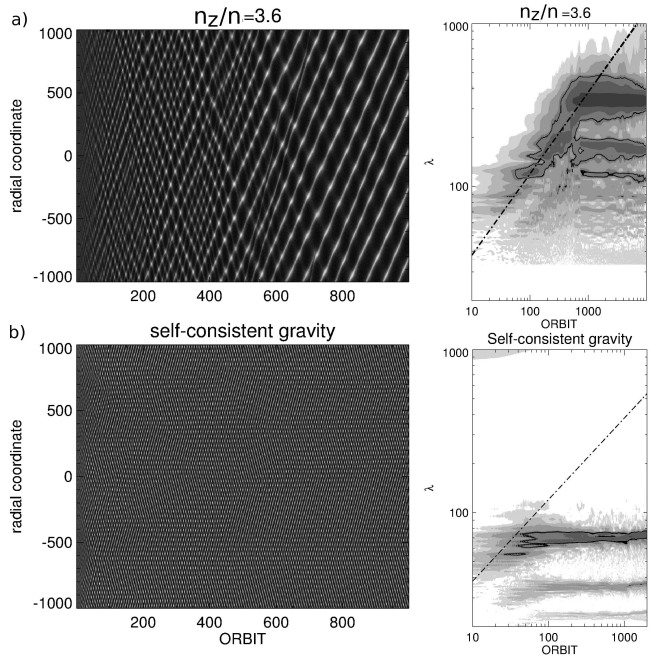

Figure 1.30 Comparison of overstable oscillations in $L_x = 2$ km wide non-gravitating (upper frames) and self-gravitating (lower frames) simulations ($\tau_D = 1.2$, "frosty" ice elasticity). The frames in left show the evolution of the density profile with time, while in the right the corresponding amplitude spectrum is shown ($A_m(\lambda)$; see Eq. (1.76)). In a) vertical self-gravity is mimicked with an enhanced $n_z/n = 3.6$. This leads to overstable oscillations whose radial wavelength grows until $\sim$ 400 meters; before saturation the $\lambda_{\max}$ grows proportional to $\sqrt{t}$. In b) gravity is treated self-consistently ($r_h = 0.57$), and now the growth of overstable oscillations is limited to less than 100 meters. In the amplitude spectra the 10% contour is indicated with a thick line. The dashed line in a) indicates the radial wavelength with the largest amplitude during the initial growth period. For comparison, the same line is also shown in b).

In the self-gravitating simulation with same parameter values (Fig. 1.30b), the initial evolution is quite similar, in addition to weak wakes being superposed with the rapidly evolving axisymmetric overstable oscillations. However, the wavelengths of oscillations do not grow beyond about 100 meter level, although there should be enough time and spatial room for further growth (see the amplitude spectrum). Unfortunately, such self-gravitating simulations are much more time-consuming than non-gravitating runs, since they must have also a tangential width sufficiently large to allow the gravity wakes properly evolve (at least 2 λ_T): the non-gravitating simulations with $n_z/n > 1$ stay axisymmetric so their tangential width can be very narrow (even just few particle diameters).

[11] The same condition, $\beta \gtrsim 1$ holds also in non-gravitating 2D simulations where the steep rise of ν_{nl} when the close-packing limit is approached, makes the system strongly overstable already for $\tau_D \gtrsim 0.4$. This fact was utilized in Salo (2001) to directly demonstrate the overstability mechanism, before it was technically feasible in 3D simulations. In all these cases the large value of β is related to high impact frequency.

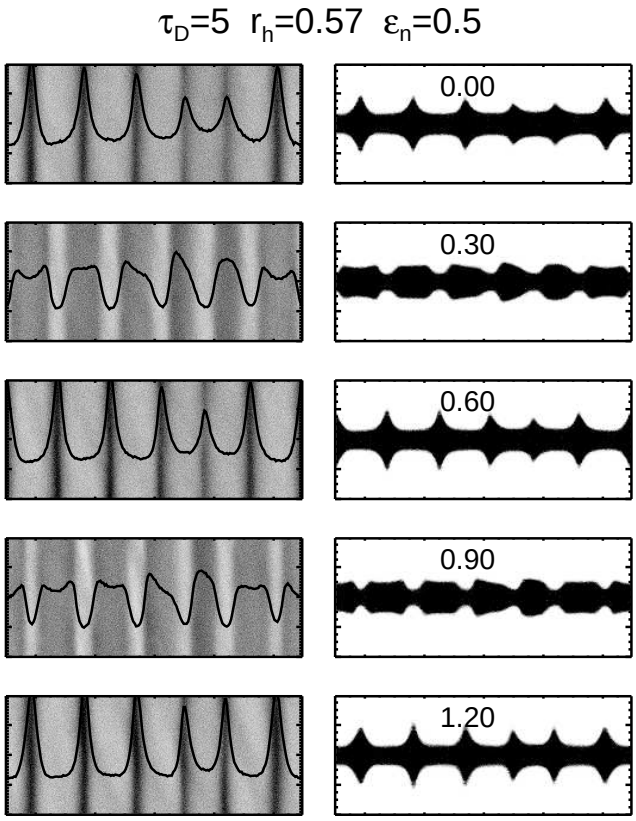

Figure 1.31 Overstable oscillations followed over one full oscillation cycle (~ 1.2 orbital periods; the prolongation over one orbital period is due to self-gravity). The $10\lambda_T \times 2\lambda_T$ calculation region is shown from the top (left; the curve indicates the optical depth profile in the range from 0 to 10) and from the side (right; vertical scale exaggerated by a factor of 5). Note the strong vertical "splashing" (Borderies et al., 1985) associated with the density crests: the ring behaves in a nearly incompressible manner. Constant $\epsilon_{\rm n} = 0.5$ with mean $\tau_D = 5, r_h = 0.57$.

Figure 1.31 illustrates overstable oscillations over one oscillation period in a very dense system ($\tau_D = 5$) with moderate strength of self-gravity ($r_h = 0.57$). Unlike strong self-gravity wakes at larger r_h, both the maximum and minimum optical depths stay very high (minimum $\tau_D \gtrsim 2-3$ and maximum $\tau_D \gtrsim 10$). If this type of oscillatory behavior is typical to the densest part of the B ring ($\sim 110,000$ km), then according to the survey of Fig. 1.24 the internal density $\rho \sim 300$ kgm^{-3}, in order to yield $r_h \approx 0.6$. This would require the ring particles to be quite porous. Moreover, the presence of overstabilities would seem to rule out very elastic particles. Even smaller internal densities ($\rho \sim 225$ kgm^{-3}) are suggested by the presence of axisymmetric overstable oscillations in the innermost A ring at 124, 000 -125, 000 km (Thomson et al., 2007; Hedman et al., 2014). A remarkable observation is the very long azimuthal coherence length of the oscillations, over thousands of kilometers, verified by the Hedman et al. (2014) high radial resolution stellar occultation observations with the Cassini VIMS (see Fig 1.32).

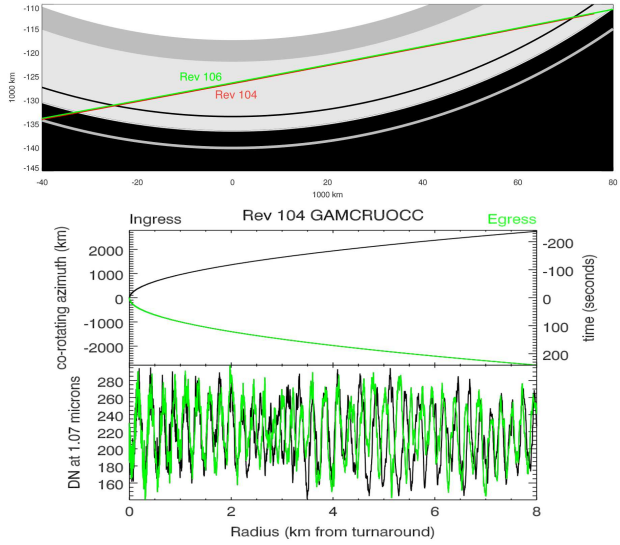

Figure 1.32 Cassini VIMS stellar occultation measurements of viscous overstability in the inner A ring. The upper frame illustrates the γ Crucis occultation track behind the ring, with a radial turnaround at 124, 413 km. The lowermost frame displays the radial profiles of the transmitted signal, both before ("ingress") and after ("egress") the turnaround point. The middle frame indicates the co-rotating azimuthal location corresponding to each radial distance around the turnaround point. The radial profiles align up to 2 km from the turnaround point, indicating that the pattern must be coherent and axisymmetric over 2500 km in the azimuthal direction. Figures from Hedman et al. (2014).

1.8.2 Viscous instability

In the case of viscous instability, the hydrodynamic stability criterion

$$\beta < -1 \quad \text{instability condition}$$

is fully consistent with direct N-body simulations (Salo and Schmidt, 2010), although the shortest unstable wavelengths ($\sim$ 200 particle radii) are about a factor of ten larger than what a simple hydrodynamical linear stability analysis predicts. Figure 1.33 displays large scale (radial width 1 km) simulations, which illustrate how the non-gravitating "smooth" ice elasticity model leads to spontaneous amplification of density fluctuations for $0.75 \lesssim \tau_D \lesssim 2$, in very good agreement with the range of τ_Ds where the steady-state $\beta < -1$ in the small scale simulations of Fig. 1.15. The system is initially uniform and it takes about 100-500 orbital periods for random fluctuations to amplify to a non-linear regime. Fig. 1.24b illustrated that viscous instability may arise also when self-gravity is included provided that $\beta < -1$ (see the snapshots with $\tau_D = 0.9, r_h \sim 0.7$). [12]

[12] The same instability condition applies to 2D systems. Due to different functional form of impact frequency (see Sect. 1.7.1.1) hot 2D systems have $\beta < -1$ at the limit $\tau_D \to 0$, which makes direct demonstrations of viscous instability numerically much easier than in 3D systems where $\tau_D \sim 1$ is required (Salo, 2001; Salo and Schmidt, 2010).

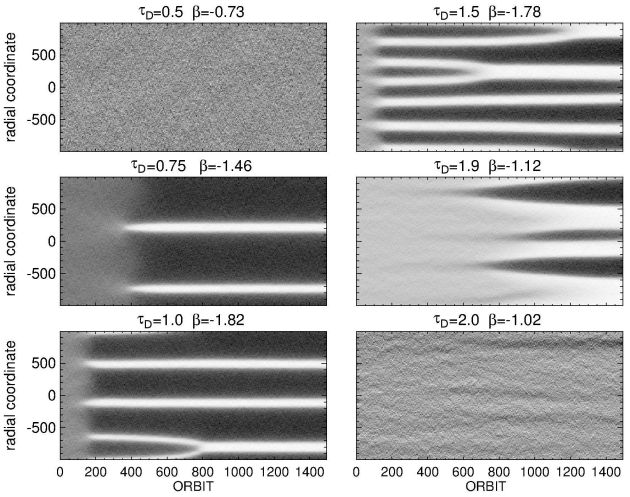

Figure 1.33 Emergence of viscous instability in large-scale simulations (2km radial extent) using the "smooth" ice elasticity model. The value of β is for the uniform initial state, $\beta \leq -1$ indicates linear instability. Figure from Salo and Schmidt (2010)

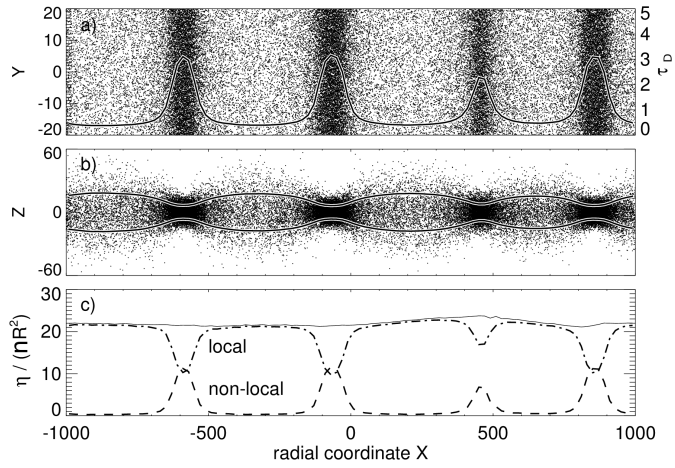

Figure 1.34 Nonlinear radial balance between dense and rarefied regions resulting from viscous instability. The upper two frames show a) the top and b) side views of a simulation with $\tau_D = 0.92$, using the "smooth" ice elasticity model. The frame c) depicts the dynamic viscosity profile (solid curve), showing separately the local (dash-dotted) nonlocal (dashed) contributions. Figure from Salo and Schmidt (2010).

Figure 1.34 depicts in more detail the nonlinear steady-state after the saturation of viscous instability. The state is characterized by a balance of radial particle flux between flattened dense ringlets surrounded by rarefied, large velocity dispersion regions, exactly as envisioned in Hämeen-Anttila (1978). The dynamic viscosity (obtained by tabulating pressure tensor separately at different radial zones) has a nearly constant value through the simulation system. Note that one of the ringlets has a slightly lower τ_D than the other three. This ringlet corresponds to a small bump in η and is accordingly slowly dissolving. With time, the ringlets slowly merge (see Fig 1.33), their typical separation growing $\propto \sqrt{t}$. In contrast to overstability, there is no mechanism known which would stop this growth. Thus at least in principle, large scale structure may emerge as a result of viscous instability.

Viscous instability is typically not regarded as a candidate for the ring fine-structure, basically since it requires fairly elastic particles in order to operate. In such a case the self-gravity wakes are harder to form. Also, the basic instability model in its simplest forms always requires a balance between a rarefied and a dense region, and thus, does clearly not apply, say, to the structure of the dense B ring.

1.8.2.1 Selective viscous instability

There is a variant of the standard instability model that would allow both the minimum and maximum optical depths to be high, namely the possibility of a selective instability of small particles against the more uniform background of larger ones (Stewart et al., 1984). Direct simulations (Salo and Schmidt, 2010) indicate that under certain conditions such a behavior occurs if the coefficient of restitution is smaller in mutual impacts between small particles, than in impacts involving large particles. Such size-dependence of $\epsilon_{\rm n}$ adds a new degree of freedom to the system, and in principle allows a balance of radial flux also between two dense regions, provided that they have a different mixture of small and large particles. Importantly, the contrast can also have very different values depending on the details of the elasticity model assumed (Fig. 1.35). Nevertheless, this mechanism has yet been very little studied, and due to lack of relevant laboratory measurements it remains unclear whether real particles possess suitable size dependence of $\epsilon_{\rm n}$ required by this type of instability.

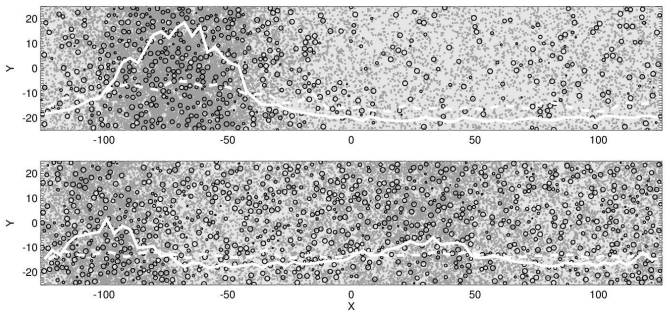

Figure 1.35 Two examples of *selective viscous instability* in simulations (after 700 orbital periods). The systems consist of two particle sizes with R_2/R_1=3, and both population have $\tau_D = 0.5$. Small (large) particles are indicated by gray (black) color, and the solid (dashed) white curve indicates their radial density profile. In the upper frame the impacts between small particles are much more inelastic than those between large particles, leading to strong density contrast among the small particles. In the lower frame the size-dependence of elasticity is weaker, leading to less pronounced variations. For exact parameter values, see Figs. 21 and 22 in Salo and Schmidt (2010).

1.9 Three-body and N-body simulations of particle and aggregate dynamics

In dilute rings where collision frequency is sufficiently smaller than the orbital frequency, particles' orbits evolve through successive two-body collisions and gravitational encounters. Dynamical evolution of such a system can be described by the formulation based on the three-body problem (Petit and Hénon, 1987; Ohtsuki, 1992, 1999, 2012). This approach is useful to understand the orbital behavior of dilute rings where both collisional and gravitational encounters are important. When particles' velocity dispersion is sufficiently large to neglect their mutual gravity ($c \gg c_{enc}$) and the extent of their radial excursion is much larger than their physical size ($c \gg nR$), their orbital change due to inelastic collision for a given restitution coefficient can be calculated analytically, and the stirring rates of their velocity dispersion can be obtained (Ohtsuki, 1992, 1999). For example, when particles are smooth spheres and their normal restitution coefficient is independent of impact velocity, the critical value of the restitution coefficient for the energy balance can be obtained as $\varepsilon_{\rm crit} = 0.627$ (Ohtsuki, 1999), which perfectly agrees with the low-optical-depth limit of the results obtained by solving the Boltzmann equation (Goldreich and Tremaine, 1978b; Hämeen-Anttila, 1978, Figure 1.14). Collision frequency can also be obtained as (Ohtsuki, 1999)

$$\omega_c = \frac{16I(c_3/c_1)}{\pi^2} n\tau_D, \tag{1.135}$$

where I is expressed in an integral form as a function of the ratio of the vertical velocity dispersion to the radial velocity dispersion. In dilute rings in the steady state, $c_3/c_1 = 0.653$ (Goldreich and Tremaine, 1978b; Ohtsuki, 1999) and $\omega_c \simeq 2.87 n\tau_D$, which agrees with Eq.(1.116).

The effects of particles' mutual gravity on the velocity stirring rates can be evaluated using orbital integration for the three-body problem. Each orbit is integrated starting and ending at positions sufficiently far from the interacting particle, and the stirring rates are calculated from the change of orbital eccentricity and inclination. Using these stirring rates, the evolution of velocity dispersions in dilute rings is calculated, and an agreement with N-body simulation is confirmed (Ohtsuki, 1999; Ohtsuki and Emori, 2000). A similar approach has been used to show that the equilibrium velocity dispersion in dilute rings can be approximately given as $c_{\rm eq} \sim \max(Rn, v_{\rm esc})$, where R is the particle radius and $v_{\rm esc}$ is the particles' mutual escape velocity. Taking account of surface friction with the tangential restitution coefficient $\varepsilon_{\rm t}$ in the hard-sphere model, the above three-body approach can also be used to examine coupled evolution of velocity dispersion and particle spin, as well as the equilibrium spin rates of moonlets embedded in dilute rings. Again, stirring rates for the velocity dispersion and spin rates, as well as the equilibrium spin rates can be obtained analytically when mutual gravity is neglected (Ohtsuki, 2004a, 2006a), and the effects of mutual gravity are examined by three-body orbital integrations (Morishima and Salo, 2004; Ohtsuki, 2004b, 2005, 2006a,b). For example, the dispersion in the particle spin rates for dilute rings with a relatively narrow size distribution obtained by this method agrees with N-body simulations (Ohtsuki and Toyama, 2005; Morishima and Salo, 2006). This approach can also be used to examine dynamical behavior of dilute rings with a more extended size distribution, as is done in the study of velocity dispersion of planetesimals in the early solar system (Ohtsuki et al., 2002). Viscosity of dilute rings can also be obtained from the calculation of the change of particles' semi-major axes by three-body calculation (Tanaka et al., 2003; Yasui et al., 2012). However, the three-body approach cannot describe the collective effects that become essential in dense rings, for which direct N-body simulations are required.

At radial locations sufficiently far from the central planet, the gravitational accretion of colliding particles becomes possible. When two spherical particles with identical internal density ρ are in contact and in synchronous rotation, with their line of centers pointing to the planet, they become gravitationally bound if they are located outside the critical distance defined as

$$\frac{a}{R_P} = \alpha \left(\frac{\rho_P}{\rho} \right)^{1/3}, \tag{1.136}$$

where a is the distance from planet, and R_p and ρ_P are the mean radius and density of the central planet, respectively. The factor $\alpha = 2.29$ for a pair of identical sizes, $\alpha = 1.44$ when one of the particles is much larger than the other (Weidenschilling et al., 1984), and $\alpha = 2.456$ corresponds to the expression for the classical Roche limit (Chandrasekhar, 1969). The probability of gravitational accretion of colliding ring particles depends on their impact velocity and impact orientation. Three-body orbital integrations (Ohtsuki, 1993; Morishima and Salo, 2004; Ohtsuki et al., 2013) show that the efficiency of accretion depends on the ratio of the sum of the physical radii of the particles to their mutual Hill radius, i.e., $r_{\rm p} \equiv (R_1 + R_2)/R_{\rm H}$, which is the inverse of r_h defined by Eq. (1.127). Equation (1.136) with $\alpha = 2.29$ and 1.44 are equivalent to $r_{\rm p} = 1$ with $R_1 = R_2$ and with $R_1 \gg R_2$, respectively.

Although gravitational accretion is possible when $r_{\rm p} < 1$, three-body calculations show that accretion efficiency decreases abruptly when $r_{\rm p}$ exceeds ~ 0.7, because a part of the particles' surfaces is outside of their mutual Hill sphere (Ohtsuki, 1993; Ohtsuki et al., 2013); while the semi-axis of the Hill sphere in the radial direction is $R_{\rm H}$ by definition, the semi-axis lengths in the azimuthal and vertical directions are $(2/3)R_{\rm H}$ and $\gamma_z R_{\rm H}$, respectively, where $\gamma_z = 3^{2/3} - 3^{1/3} \simeq 0.638$ (Yasui et al., 2014). Karjalainen and Salo (2004) performed N-body simulation and examined the dependence of the critical radial distance for gravitational accretion of particles in Saturn's rings on various parameters, such as the elastic properties of particles and the rings' optical depth. For example, in their standard case of rings of equal-sized particles with $\rho = 900$ kg m^{-3} and $\tau_D = 0.25$, temporary aggregates and stable aggregates can form in the inner and the outer A ring, respectively, with exact radial boundaries depending on elastic properties of particles (see Figs. 1.24 and 1.38). The above dependence of the critical distances on the elastic properties implies that the actual efficiency of gravitational accretion can also be

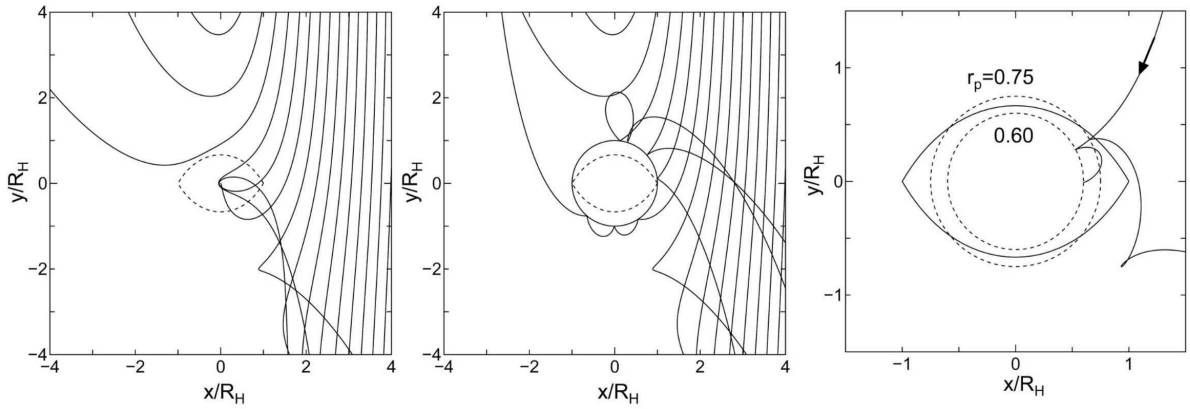

Figure 1.36 Examples of orbits of particles in the case of $r_{\rm p} = 10^{-3}$ (left panel) and 1 (middle panel); note that $r_{\rm p}$ is the inverse of the parameter r_h used in the previous Section. In both cases, Hill's equation for the relative motion is numerically solved for initially circular, coplanar orbits, and the interacting particle is at the origin of the coordinate system. The dashed line represents the two interacting particles' mutual Hill sphere. In the case of the left panel, which corresponds to orbits of planetesimals at a radial location 1AU from the sun, no direct collisions are detected and the orbital changes are caused by the mutual gravitational interaction alone. The solid circle in the middle panel shows the physical size of the colliding particles. In the case shown here, four orbits lead to direct collision, and the orbital changes are calculated assuming that particles are perfectly, elastic smooth spheres. The right panel shows examples of orbits leading to collision with another particle (smooth spheres with $\varepsilon_{\rm n} = 0.5$), for two different values of $r_{\rm p}$; the difference in $r_{\rm p}$ corresponds to, for example, changing the distance from the central body for a given internal density of the particles. In the case of $r_{\rm p} = 0.75$, the orbit results in escape after the first collision, while the orbit in the case of $r_{\rm p} = 0.6$ leads to accretion after the second impact (Ohtsuki, 1992, 1993, 2012).

limited by velocity dispersion of particles, because more kinetic energy needs to be dissipated for gravitational accretion to occur. The shapes of the simulated aggregates in Karjalainen and Salo (2004) are close to Roche ellipsoids (Chandrasekhar, 1969) near the critical distance, getting progressively rounder at larger distances (Fig. 1.37).

When porous, low-density particles coexist with dense bodies such as collisional shards, particles can gravitationally accrete onto such dense bodies even at radial locations where the low-density particles alone cannot form gravitational aggregates (Porco et al., 2007). When the surface of the dense "core" is not yet significantly covered by particles, accretion of particles proceeds at a nearly constant rate that is determined by two-body collision rate between the core and accreting particles (Ohtsuki et al., 2013). With the growth of the aggregate (the dense core surrounded by the low-density particles) its Hill radius increases, but the bulk density of the aggregate as a whole gradually decreases. As a result, the physical size of the aggregate increases faster than its Hill radius, and accretion stalls when particles fill the slowly-growing Hill sphere. Afterwards, the aggregate repeats accretion and shedding of particles (Lewis and Stewart, 2009; Yasui et al., 2014).

The bulk density of a body (satellite) that entirely fills its Hill sphere defines a critical density $\rho_{\rm Roche}$ at its radial distance a from the planet as (Porco et al., 2007; Tiscareno et al., 2013a)

$$\rho_{\rm Roche} = \frac{3M_P}{\gamma a^3}, \tag{1.137}$$

where γ is a dimensionless shape parameter so that $\gamma R_{\rm sat}^3$ is the volume of the satellite with $R_{\rm sat}$ being its long semi-axis ($\gamma = 4\pi/3$ for a spherical satellite, and $\gamma \simeq 1.509$ for a body with a shape of the Hill sphere; Leinhardt et al. (2012)). Observations by Cassini show that the Hill radii of the small moons in the outer A ring and those near the ring outer edge are very close to the observed long axes of these satellites, and their densities ($400 - 600$ kg m^{-3}) are also very close to the above critical density at the radial location of each satellite (Porco et al., 2007).

These observations suggest that those small moons near the outer edge of Saturn's main rings formed by gravitational accretion of small particles, and support the recent models for the formation of ring-satellite systems of giant planets from an ancient ring that was much more massive than the current ring system (Charnoz et al., 2010; Canup, 2010; Salmon et al., 2010; Charnoz et al., 2011; Crida and Charnoz, 2012; Hyodo et al., 2015a). The originally massive disk radially spreads through collision and gravitational interactions among particles. Those particles spreading beyond the Roche limit gravitationally accrete to form small satellites, and the formed satellites migrate outward due to torques induced by the disk and the planet (Charnoz et al., 2010; Crida and Charnoz, 2012). Satellites produced from a disk with a larger surface density tend to be more massive, while the disk surface density gradually decreases as the radial spreading proceeds. Also, more massive satellites migrate more rapidly because the torques are an increasing function of mass, and the different migration rates lead to orbital crossings and merging (Charnoz et al., 2010). As a result, the outer satellites tend to be more massive, which explains the observed trend of the satellite systems of Saturn, Uranus, and Neptune (Charnoz et al., 2010; Canup, 2010; Crida and Charnoz, 2012). As for the origin of such a massive circumplanetary particle disk, in addition to the classical model for the ring origin by impact disruption of a satellite (Harris, 1984; Charnoz et al., 2009), tidal stripping

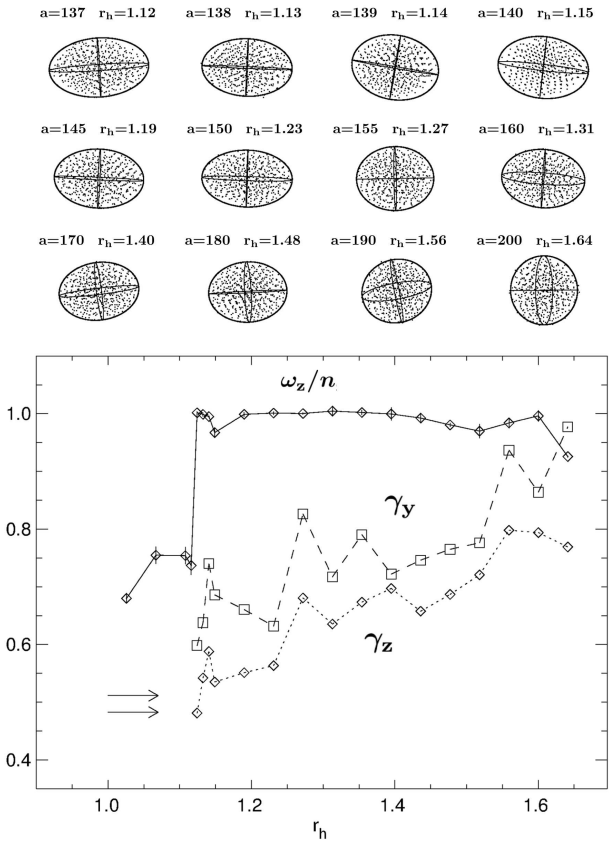

Figure 1.37 Examples of gravitationally bound aggregates forming in numerical simulations of identical particles ($\tau_D = 0.25$, "frosty" ice $\epsilon_{\rm n}(v_n)$). The projections of aggregates to the equatorial plane are shown, together with a fitted 3-axial ellipsoid: the labels indicate the r_h parameter, and the corresponding distance for $\rho = 900$ kgm^{-3}. The lower frame indicates the vertical-to-radial (γ_z) and tangential-to-radial (γ_y) axial ratios of the aggregate, and the spin of the aggregate ω_z/n. The jump of ω_z/n to unity (synchronous rotation) corresponds to the transition from self-gravity wakes to bound aggregates. The arrows indicate the axial ratios of the most elongated stable Roche-ellipsoid for a gravitating fluid body (Chandrasekhar, 1969) . These simulations correspond to Fig. 1.24a, except that fiction with $k_f = -0.1$ (see Eq. 1.61) was included: this shifts the boundary of accretion inward by about 5000 km. Redrawn from Karjalainen and Salo (2004).

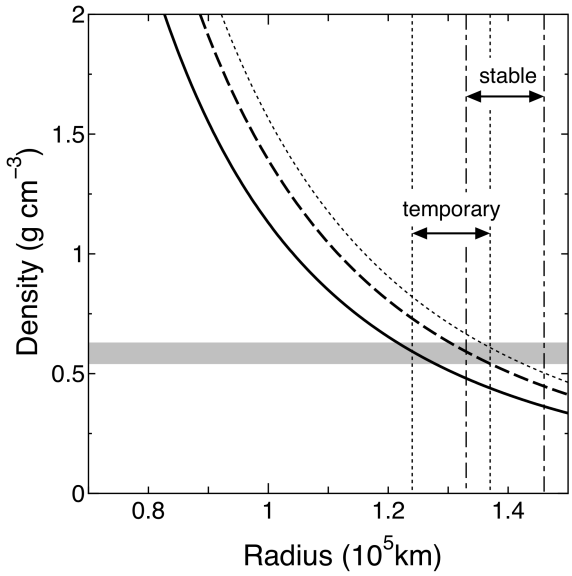

Figure 1.38 Critical densities as a function of the distance from Saturn. The solid line represents $\rho_{\rm Roche}$ (Eq. (1.137)). The dashed line represents the critical bulk density of gravitational aggregates consisting of equal-sized particles against tidal disruption ($\rho_{\rm tidal}$; Eq. (1.138)) obtained by Leinhardt et al. (2012). The thin dotted curve represents $\rho_{\rm core,crit}$ (Eq. (1.140)) derived from the condition $r_{\rm h,core} = {\gamma_z}^{-1}$ (Yasui et al., 2014). The radial locations of the inner boundary for the formation of temporary aggregates and those of stable aggregates obtained by N-body simulations (Karjalainen and Salo, 2004) are shown by the vertical dotted lines and the vertical dot-dashed lines, respectively. The horizontal shaded band shows the range of the bulk density of gravitational aggregates obtained by N-body simulations ($540 - 630$ kg m^{-3}), corresponding to the filling factor of $0.6 - 0.7$. Redrawn from Yasui et al. (2014)

.

of icy mantle layers of a differentiated satellite migrating in a circumplanetary gas disk (Canup, 2010) and tidal disruption of a passing Kuiper-belt object (Dones, 1991; Charnoz et al., 2009) have been proposed, and simulations of tidal disruption of a passing differentiated Kuiper-belt object using the smoothed particle hydrodynamics method shows that the latter model seems to naturally explain the small size of ring particles and even the compositional difference between rings of Saturn and Uranus (Hyodo et al., 2015b). More detailed discussion on the origin of ring-satellite systems of giant planets are described in Chapter by Charnoz et al.

We plot $\rho_{\rm Roche}$ defined by Equation (1.137) as a function of the distance from Saturn in Figure 1.38. Note that the filling factor in gravitational aggregates obtained by N-body simulation with identical particles typically takes on $0.6 - 0.7$, yielding a bulk density $\rho_{\rm bulk} = 540 - 630$ kg m^{-3} when the density of constituent particles is 900 kg m^{-3} as was assumed in Karjalainen and Salo (2004). We find that the inner boundary for the formation of temporary aggregates obtained by N-body simulation approximately corresponds to the location of $\rho_{\rm bulk} = \rho_{\rm Roche}$. That is, temporary aggregates would form at the radial locations corresponding to $\rho_{\rm bulk} \geq \rho_{\rm Roche}$ when collisions are sufficiently dissipative, but due to finite impact velocities, the critical radial distance shifts outward if energy dissipation at collision is insufficient. The above correspondence also shows difficulty in forming stable aggregates without dense cores even at the radial location corresponding to $\rho_{\rm bulk} = \rho_{\rm Roche}$.

On the other hand, Leinhardt et al. (2012) examined tidal disruption of gravitational aggregates placed at different radial distances from a planet, and obtained the critical bulk density of aggregates as a function of the distance. For example, in the case of aggregates consisting of identical particles, the critical density for stability against tidal disruption ($\rho_{\rm tidal}$) can be written as

$$\rho_{\rm tidal} = \frac{7.7 M_P}{\pi a^3}, \tag{1.138}$$

which is shown in Figure 1.38 with the dashed line. The formation of stable aggregates obtained by Karjalainen and Salo (2004) approximately corresponds to the above critical distance for the stability against tidal disruption.

When particles accrete onto large cores, an important quantity is the ratio of the Hill radius of the core ($R_{\rm H,core}$) to its physical size ($R_{\rm core}$),

$$r_{\rm h,core} \equiv R_{\rm H,core}/R_{\rm core}. \tag{1.139}$$

The core's Hill sphere covers the entire surface of the core when $r_{\rm h,core} \geq \gamma_z^{-1} \simeq 1.57$ while particles accrete only part of the core surface when $1 < r_{\rm h,core} < \gamma_z^{-1}$ (Yasui et al., 2014, Figure 1.9), and gravitational accretion does not tale place when $r_{\rm h,core} < 1$ as mentioned above. Thus, the condition $r_{\rm h,core} = \gamma_z^{-1}$ gives another critical density as a function of radial distance as

$$\rho_{\rm core,crit} = \frac{9M_P}{4\pi\gamma_z^3 a^3}, \tag{1.140}$$

which is shown by the thin dotted curve in Figure 1.38. The critical density $\rho_{\rm core,crit}$ at a given radial distance is larger than $\rho_{\rm Roche}$, because the Hill radius of a Hill-sphere-filling body (with its bulk density given by $\rho_{\rm Roche}$) is equal to the body's semi-axis in the radial direction, while the core's Hill radius needs to be larger than the core radius by a factor of $\gamma_z^{-1} \simeq 1.57$ when $r_{\rm h,core} = \gamma_z^{-1}$ (or $\gamma_z R_{\rm H,core} = R_{\rm core}$). If the density of a core placed at a certain radial distance is larger than $\rho_{\rm core,crit}$, the entire surface of the core can be covered by accreting particles. As accretion of particles onto the core proceeds, the bulk density of the formed aggregate would continue decreasing until it reaches $\rho_{\rm Roche}$ for the radial location. However, actual accretion would not proceed to this point because of limited energy dissipation and/or finite impact velocities, as mentioned above.

Snapshots of the spatial distribution of particles in the vicinity of the moonlet core. The rings are seen from the vertical direction against the plane of orbital motion. Saturn is to the left, and orbital motion is upward. The optical depth of unperturbed rings is 0.5, and particles have a size distribution with $q = 3$, $R_{\rm max} = 500$ cm, and $R_{\rm min} = 30$ cm, respectively. ($R_{\rm core} = 1250$ cm, the densities of the core and the particles are 900 and 400 kg m^{-3}, respectively, and the normal restitution coefficient is 0.5.) The left panel shows the case with $r_{\rm h,core} = 1.5$ (corresponding to $a = 1.15 \times 10^5$ km from Saturn when the density of the core is 900 kg m^{-3}), where particles can accrete only part of the surface of the core. The right panel shows the case with $r_{\rm h,core} = 1.69$ (corresponding to $a = 1.3 \times 10^5$ km from Saturn when the density of the core is 900 kg m^{-3}), where accreting particles can completely cover the surface of the core. Blue particles are those regarded as members of the aggregate, while red ones are not. A particle is regarded as a member of the aggregate if it is practically in contact (within 1% particle radii) with at least one of the members of the aggregate including the core. Redrawn from Yasui et al. (2014).

Aggregates formed by gravitational accretion of particles in the Roche zone have a Hill sphere comparable to their physical size. In this case, even a slight deformation from its stable shape due to collision with other particles or aggregates would lead some particles to become gravitationally unbound, which would then result in total disruption of the aggregate. Thus, even stable aggregates are likely vulnerable to collisional disruption. In fact, transient brightening was observed in Saturn's F ring by Voyager (Showalter, 1998), and shedding of small particles by disruption of embedded bodies has been proposed as the cause of such events (Barbara and Esposito, 2002). More recently, small protrusions from the core of the F ring, called "mini-jets," have been observed by Cassini, and they are regarded as showing low-velocity collisions within the ring (Attree et al., 2012).

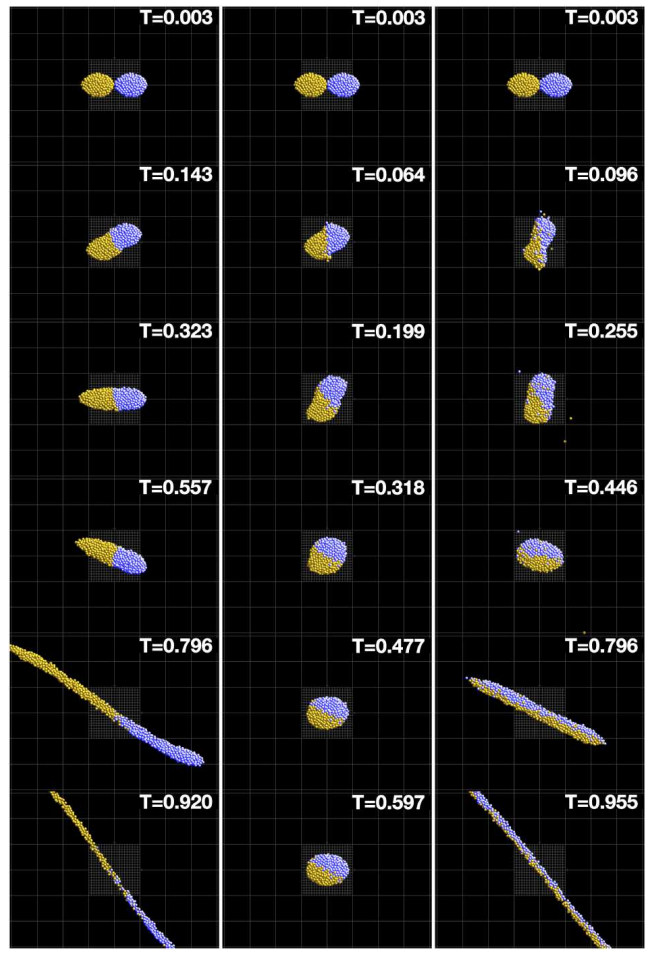

Figure 1.39 Time series of simulations of collisions between aggregates in the tidal environment corresponding to the radial location of Saturn's F ring ($a = 140,000$ km). Saturn is to the left, and orbital motion is upward. Two aggregates collide with each other from the radial direction. Three cases of different impact velocities ($v_{\rm imp}$) are shown. Left: Case with $v_{\rm imp}/v_{\rm esc} = 0.69$, which results in total disruption of the colliding aggregates. Middle: Case with $v_{\rm imp}/v_{\rm esc} = 1.14$, which results in total accretion. Right: Case with $v_{\rm imp}/v_{\rm esc} = 1.52$, which results in total disruption. Impacts with still higher impact velocity result in total disruption. Numbers in each panel represent the time elapsed since the start of the simulation, in units of the orbital period at the radial location of the origin of the system. Redrawn from Hyodo and Ohtsuki (2014).

Impacts between gravitational aggregates in the tidal environment have been examined by local N-body simulations. In the case of collisions of aggregates initially on circular orbits at the radial location of the F ring, N-body simulations confirmed that colliding aggregates that greatly differ in mass can more easily accrete as expected (Karjalainen, 2007), while the accretion efficiency was found to be higher than the results obtained by three-body calculations that treat the ring particles as hard spheres (Ohtsuki, 1993). The degree of disruption in collisions in free space is determined by specific impact energy, and the mass fraction of the largest remnant body is a monotonically decreasing function of impact energy. In fact, the mass fraction can be approximated by a linear function of impact energy, which is known as "the universal law" (see, e.g. Stewart and Leinhardt, 2009). However, N-body simulations show that this law is not applicable to impacts between aggregates in the Roche zone (Hyodo and Ohtsuki, 2014). Outcomes of collisions in the tidal environment sensitively depend on the impact velocity and the direction of impact, and a complete disruption of aggregates can occur even in impacts with velocity much lower than their escape velocity (Figure 1.39). In such low-velocity collisions, the deformation of colliding aggregates plays an essential role in determining collision outcomes, while the dependence of collision outcomes on impact velocity becomes similar to the case in free space when the distance from the planet is sufficiently large. Furthermore, in the case where each of the colliding aggregates has a dense core as suggested by the Cassini observations of small moons, for a wide range of parameters an impact results in only partial disruption of the aggregates and the formation of a narrow ring of particles sandwiched between two remnant aggregates (Hyodo and Ohtsuki, 2015). According to the recent model of satellite system formation from ancient massive rings, multiple small satellites are expected to coexist near the disk's outer edge for a significant period of time during the final stage of satellite system formation (Charnoz et al., 2010; Hyodo et al., 2015a). Thus, the above results of impact simulations suggest that the system of a narrow ring accompanied with small satellites near the outer edge of the main ring system is a natural outcome at the final stage of the formation process of the ring-satellite system of giant planets (Hyodo and Ohtsuki, 2015).

1.10 Rings with Nearby Moons

Many narrow rings and ring gaps have moons that orbit near the ring material. For broad rings, this leads to the formation of moon wakes (Showalter et al., 1986). In the F ring, these perturbations appear as more complex features (Kolvoord et al., 1990). The perturbations from a nearby moon destroy the symmetries that allow for the local cell simulation techniques described in section 1.2. To get around this, one can do more global simulations, or use modified boundary conditions that preserve the orbital properties of the ring particles that are induced by passing by the moon.

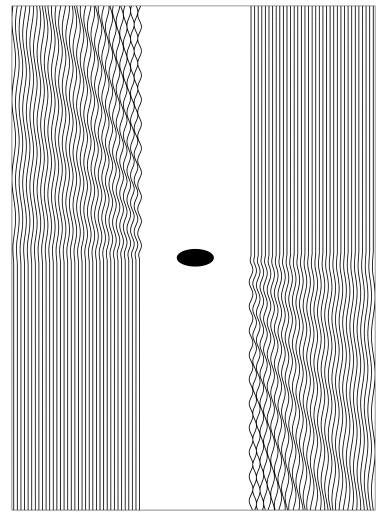

Figure 1.40 Particle paths are perturbed by the passage of a nearby moon. Keplerian shear causes the particles further from the moon to have a faster relative drift rate. The difference in wavelength of the oscillations leads to regions of compression and rarefaction referred to as moon wakes. Orbital motion is up. Particles interior to the moon, left, are drifting upward, while those exterior, right, are drifting downward relative to the moon.

1.10.1 Small Local Cell Simulations

When particles pass near a moon, they receive a forced eccentricity. Showalter et al. (1986) explored the impact of this perturbation using a simple kinematic streamline model. Their predictions led to the later discovery of Pan in the Encke gap (Showalter, 1991). The approach they took was to view particle motion as streamlines that have a zero eccentricity upstream of the moon, and which then are given a forced eccentricity by the moon. Due to Keplerian shear, the wavelength of the oscillations grows with distance from the moon. This leads to the regions of compression and rarefaction shown in Fig. 1.40.

A more complete kinematic model of the particle motion was developed by Stewart (1991) using what he refers to as guiding center coordinates, which are effectively a simplified version of the solution of the Hill's equation given in Eq. (1.5), with the perturbing moon at the origin. To simplify the discussion of the following sections, we present those equations here in the form

$$\begin{aligned} \frac{x}{a_m} &= X - e\cos(\phi), \\ \frac{y}{a_m} &= Y + 2e\sin(\phi), \\ \frac{z}{a_m} &= I\cos(\zeta), \end{aligned} \tag{1.141}$$

where

$$\begin{aligned} Y(t) &= Y_0 - \frac{3}{2} X n t, \\ \phi(t) &= \phi_0 + nt, \\ \zeta(t) &= \zeta_0 + nt. \end{aligned} \tag{1.142}$$

The use of guiding center coordinates $(X, Y, e, I, \phi, \zeta)$ led to the development of a set of local cell boundary conditions that can be applied to these perturbed systems (Lewis and Stewart, 2002). The key observation for these boundary conditions is that the value of ϕ, the angle of the particle motion around the drifting guiding center, is set by the pass by the moon and that it is not significantly altered by collisions during the time it takes the particle to drift across the simulation cell. The reason this is true is that the relative velocity differences of the particles are very small compared to their systematic velocities associated with the satellite-forced eccentricities and inclinations. Given that, when a particle drifts out of the edge of the local cell, it can be brought back on the other side by altering the y value by the width of the cell, and pulling back the ϕ angle by the amount that it would normally advance crossing the cell.

One can view this as replacing a particle that moves out of the downstream edge of the cell by an earlier image of itself entering on the upstream edge. If the azimuthal length of the cell is L_y, then the time it would take the guiding center of the particle to move across the cell is

$$\Delta t = \frac{2L_y}{3Xn} \tag{1.143}$$

and the angle should be decremented by $n\Delta t$. The systems being simulated typically have at least one real radial edge, either at the inside or outside of the cell. For that reason, the radial boundaries are left open. In addition, while the "sliding brick" boundary conditions discussed in section 1.2 remain stationary over the course of the simulation and particles move through them, in the local cell method for perturbed rings, the calculation region moves azimuthally downstream, typically at the drift rate of the inner edge. Note that these boundary conditions can be applied independent of whether or not gravity or collisions are considered, and do not depend on how gravity or collisions are calculated in the simulation.

This local cell approach has been applied to both the Encke gap region and narrow rings with a single nearby satellite (Lewis and Stewart, 2000, 2005; Lewis et al., 2011). Figure 1.41 shows a simulation that reproduces a number of the results of those papers.

The strip down the right side shows geometric optical depth. Each row in the figure represents one time step. The values were calculated every 20 time steps by breaking the simulation into radial bins and adding the cross sectional surface area of the particles whose centers are in each bin. The cell began the simulation at the top of this strip, a few thousand kilometers before encountering Pan. It then moved down the plot during the simulation as the material is radially exterior to the moon. Note the wavy edges produced by the eccentric motion of the particles after passing by the moon, and the moon wakes that form from the streamline compression. Also present at this scale is the radial migration of particles that begins around 10 degrees downstream from the moon. This is the location where the streamlines begin to intersect on the inner edge of the particle distribution in this simulation. This critical angle where streamlines shear through was called θ_{crit} by Showalter et al. (1986). Using Eq. 1.141, Lewis et al. (2011) express it as

$$Y_{crit} = -\frac{3X^2}{2e}. \tag{1.144}$$

Note that this derivation assumes a constant e, and eccentricity gradients can alter the exact location at which streamlines cross. For this simulation, the forced eccentricity after passage by the moon is 1.3×10^{-5} on the inner edge, $X = (a - a_m)/a_m = 1.21 \times 10^{-3}$, and 1.2×10^{-5} on the outer edge, $X = (a - a_m)/a_m = 1.29 \times 10^{-3}$. Plugging these values into Eq. (1.144) gives -0.169 radians or -9.7° at the inner edge and -0.208 radians or -11.9° at the outer edge.

Beginning at Y_{crit}, the material at the inner edge undergoes orbital alterations that moves it outward, into the main body of the ring. Angular momentum has to be conserved, so an equal mass of particles shifts inward radially. Most of the mass movement that balances the motion of the inner edge comes from the middle of the distribution, not the outer edge. This is due to the fact that this migration is powered by the forced eccentricity, and can only "reach out" a distance roughly equal to the forced eccentricity. The magnitude of the forced eccentricity corresponds to 1.7 km; see the amplitude of the edge waves in Fig. 1.41. This migration leads to a peak in the density of particle semimajor axes, X around 165 km from Pan and then a trough around 167 km. This trough is most pronounced around 35° downstream from the moon. At that point, the particles at the inner edge have lost roughly 60% of their initial forced eccentricity and those at the outer edge have lost over 80% of their initial forced eccentricity.

Figure 1.41, left side, shows individual particles at a few selected locations downstream from the moon. The locations of these regions are marked by horizontal lines across the surface density plot in the right. Interesting interactions between the gravity wakes and the Pan wakes are seen. As was discussed in section 1.7.2 and shown in Eq. 1.126, the wavelength of gravity wakes $\propto \lambda_T \propto \Sigma$, so the natural wavelength of gravity wakes would be larger in high density regions and smaller in low density regions. However, the Pan wakes exist because the large scale motion of the particles causes high densities where material is pushed together and lower density where it is pulled apart. The structures in the gravity wakes are compressed to have smaller wavelength, to the extreme of having no separation, moving into the moon wakes, and then they are pulled back apart leaving the peak of the moon wake and going back into the rarefied region. This causes the two structures to be at odds with one another.

The first highlighted region in Fig. 1.41, at $\phi = 9^\circ$ downstream from the moon, is an early snapshot from the simulation, just as the moon wakes are becoming strong. The second ($\phi = 14^\circ$) is after Y_{crit} has been passed and some particle migration has occurred. The third ($\phi = 33^\circ$) is after

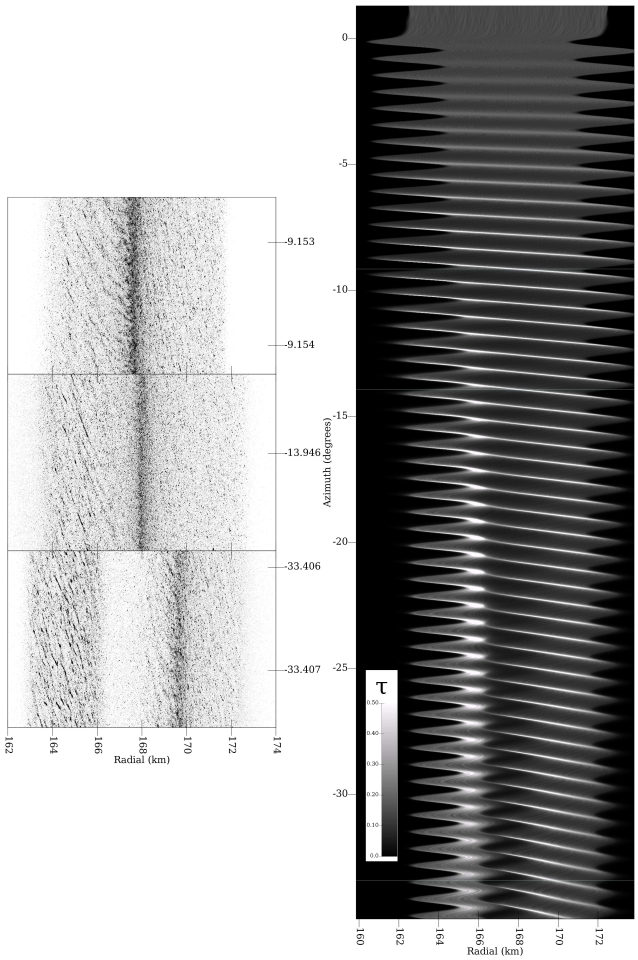

Figure 1.41 This figure shows the particle densities for a simulation of the outer edge of the Encke gap. The initial particle distribution was 10 km × 10 km. The particles have a power law size distribution with a differential slope of $q = 3$ ranging from 1.3 m to 13 m in radius. The particles have $\rho = 500$ kg/m^3 and the distribution has $\Sigma = 500$ kg/m^2 and $\tau_D = 0.14$ with roughly 0.55 million particles. The origin of the coordinate system is on Pan, which is assumed to have a perfectly circular orbit with a semimajor axis of $a_m = 133,584$ km and a mass of 4.95×10^{15} kg. Collisions are calculated using the Bridges et al. (1984) velocity dependent coefficient of restitution. Particle self-gravity if calculated using a tree method. Pan perturbs the particles, producing wavy edges in the large-scale view on the right. Streamline compression leads to moon wakes. Collisions in the wakes prevent streamlines from shearing through and modify particle orbits, leading to particle migration and increased optical depth of material at the inner edge. The frames on the left show the actual particles at specific time steps marked by lines on the right. Note the formation of oversized gravity wakes in the inner edge region.

there has been substantial damping of the forced eccentricities and significant particle migration. At the last snapshot the inner edge has an enhanced density due to particle migration, and the gravity wakes in this region have become much larger, thick, ropey structures. This is due to more than just the high density. The regular motion caused by having higher eccentricities and a strong eccentricity gradient also play a role. They are not static structures with a

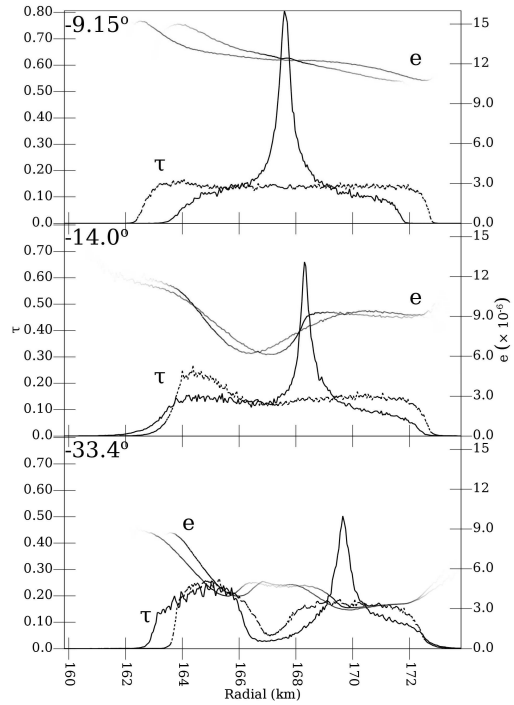

Figure 1.42 Radial slices through the simulation region for the highlighted locations in Fig. 1.41. The plot shows the τ_D and e values both as a function of radial location x, with a solid line, and as a function of mean distance X, with a dotted line.

fixed angle. They go from being almost azimuthal in a wake peak to being slightly closer to radial than what is shown in Fig. 1.41. These oversized gravity wakes have been compared to images of "straw" seen in high resolution Cassini images of nonlinear density waves. The low density region from 166 to 168 km was depleted in the formation of the high density edge region, and is thus not just caused by orbital motion. At $\phi = 33°$, very few particles have semimajor axes in that area.

Figure 1.42 shows both eccentricity and optical depth at the three locations highlighted in Fig. 1.41. In the top frame, we see an eccentricity distribution that has only been slightly modified from that induced by the passage of the moon with the value gently decreasing with radial distance. At $\phi = 14°$ the eccentricities have damped significantly interior to 168 km, and a concentration of particles has begun to build at the inner edge. This trough in eccentricity leads to a steep negative gradient near the edge and an inversion outside that. At $\phi = 33°$, the particle density between 166 and 168 km is near a low point, and the only particles in that area are those with large eccentricities. The steep eccentricity gradient across the high density region persists. This is significant as it effectively moves the location of Y_{crit}, the azimuthal location at which streamlines cross, downstream, which allows this region to maintain a high eccentricity for longer. Without this, the streamlines would shear through, which leads to more energetic collisions what would damp the eccentricity much more quickly.

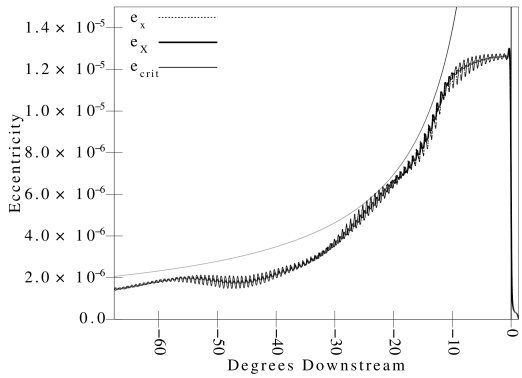

Figure 1.43 The average eccentricity of the particles for an azimuthal slice at 170 km radial distance from Pan. The eccentricity is drawn for both as a function of radial location x and as a function of mean distance X. The former oscillates around the latter as the particles orbit due to the eccentricity gradient in e over radial distance. Plotted along with this is an analytic expression for the eccentricity value that would cause streamlines to shear through one another at those locations.

In these simulations, particle streamlines never shear through one another by more than a tiny amount, even in rather low average optical depth simulations, as low as 0.01 average optical depth. This is the root cause of the particle migration seen here, and why it doesn't begin until Y_{crit} is reached. This fact is highlighted by Fig. 1.43, which shows the eccentricity values in the actual simulation compared to what ones gets solving Eq. (1.144) for e for a cut through the simulation. Note that the eccentricity is consistently damped just enough to keep it below the level that would cause the streamlines to shear through one another.

The boundary conditions described earlier in this section have the advantage that they allow a small cell and fewer particles. However, they have a limitation in that there can only be a single perturber on a circular orbit. If there are multiple perturbing moons, then the drift rate that is used for Eq. (1.143) differs between the moons. If the moon is on an eccentric orbit, then the magnitude of the forced eccentricity varies with azimuth, breaking the assumptions needed for wrapping particles.

The circular orbit restriction can be lifted by using a larger cell whose size is determined by the length of the synodic period of the ring particles relative to the perturbing moon. This approach was used by Lewis and Stewart (2005) to look at the dynamics of the F ring, ignoring the influence of Pandora. These boundary conditions have open edges on the radial bounds, and the azimuthal bounds are pure periodic, but they are not parallel. The length of a synodic period from Eq. 1.142 is given by how long it takes for ϕ to advance 2π, or $\Delta t = 2\pi/n$. The azimuthal length of the simulation cell needs to be

$$L_y = 3\pi X \tag{1.145}$$

in order for periodic bounds to make sense. Using this azimuthal length guarantees that particles at opposite ends of the cell pass by the moon when it is at the same point in its orbit, so particles can be wrapped around without having a discontinuity in their eccentricity.

These extended boundary conditions work very well except for the period of time when the cell is close to the moon, as particles at the front edge will get a forced eccentricity before those at the back edge, and if they are wrapped during that time, there will be a sharp, and non-physical discontinuity in the particle distribution. For this reason, the boundary conditions should be turned off completely before the cell reaches the moon, and they should remain off until after the cell is sufficiently past the moon for the back edge to be clear of the perturbations of the moon. At that point, they can be turned back on. During the time they are off, the cell will shear out. This is acceptable in practice because the cell is broad enough that the amount of shear is relatively small compared to the azimuthal length of the cell. In addition, the cell shape is a trapezoid to begin with, and it is easy to make it so that the edge that is not oriented along the radial axis shears toward the radial axis during this time.

Lewis and Stewart (2005) used these boundary conditions in simulations of F ring-like systems with an eccentric Prometheus and no Pandora. This work showed that a variety of different structures, including braid-like structures, could be created by a single eccentric perturber. By altering the radial distance between the perturbing moon and the center of the ring particle distribution, it was found that rings centered on resonance tended to have their material collapse to a small azimuthal extent, effectively forming arcs.

1.10.2 Global and Semi-Global Simulations

Neither of the local cell methods work when there are two perturbing satellites as having a second perturbing satellite breaks all the symmetries that are assumed by the boundary conditions. As a result, the simulation cell must be large enough to be effectively global. The term "effectively" is used because for some systems, the dynamics can be explored in a time scale on the order of 10-20 orbital periods, and the cell only needs to be larger than the azimuthal drift of the particles over that period of time.

Perhaps the first simulations of perturbed rings performed by Hänninen and Salo (1994) used this approach. More recently, these types of simulations have been performed for the Keeler gap (Perrine and Richardson, 2006, 2007; Lewis and Stewart, 2006a,b; Hansen and Lewis, 2015) and the F ring (Lewis and Stewart, 2007).

Due to the proximity of the moon in the Keeler gap, the synodic period is extremely long, and the streamlines collide almost instantly, leading to very rapid damping of the forced eccentricity. As a result, the simulation cell need only be azimuthally long enough to cover the shear of 20 orbits in order to see the dynamics that one is interested in.

Figure 1.44 shows the rapid change in the edge features caused by particle collisions in the moon wakes in the 3-4 orbits after passing the moon. As in the Encke gap simulation, an edge region builds up with an enhanced surface density. This also leads to the material pulling back radially

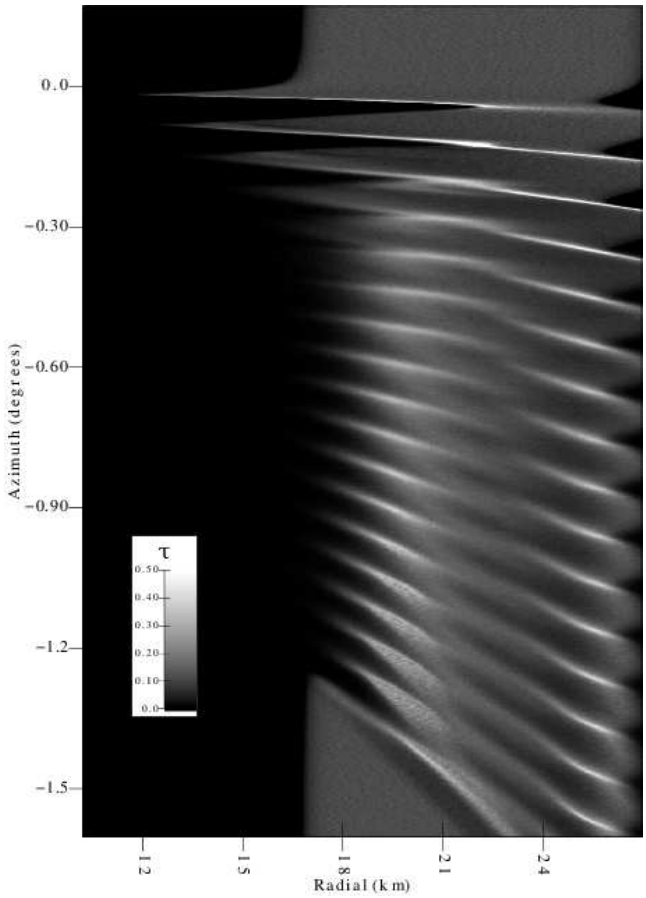

Figure 1.44 This figure shows a large section of a Keeler gap simulation using a semi-global boundary condition. The full cell is larger than what is shown here. This simulation used roughly 80 million particles, each with a radius of 5.5 m and $\rho = 700$ kgm^{-3}. The simulation region has $\Sigma = 600$ kgm^{-2} and $\tau_D = 0.12$. Other aspects of the simulation are the same as for the Encke gap simulation described in section 1.10.1. At the bottom of the figure, one can see a triangular region of particles with a smooth distribution. These particles began the simulation downstream of the moon, and were never perturbed during the simulation. Note that the aspect ratio of this figure is compressed in the azimuthal direction.

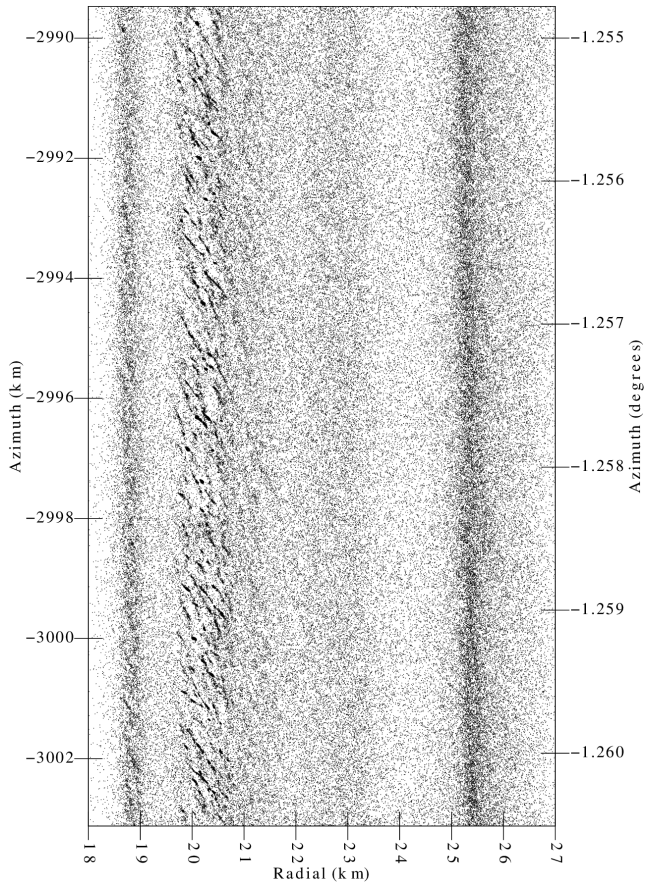

Figure 1.45 Individual particles from one small region of a Keeler gap simulation of Fig. 1.44, where oversized gravity wakes have begun to form in the inner edge region.

from the moon in a manner that is consistent with what is seen in Cassini observations.

The surface density used in this simulation is higher than what is inferred for this region based on density wave measurements. The reason for this choice was to see if we could induce the straw-like extended wakes shown in Fig. 1.41 for the Encke gap as a possible alternate explanation for observations of gaps near gap edges in Cassini occultations (Albers et al., 2015). Figure 1.45 shows a small section of this simulation where these structures did indeed form. Their presence is indicated in figure 1.44 by the grainy appearance of some of the later moon wakes. These extended gravity wakes do not work as an explanation for the observations of Albers et al. (2015). Those observations show regions with a radial extent for a kilometer or more that have no material in them at the level of sensitivity of the Cassini occultation measurements. Synthetic occultations of this simulation fail to reproduce that type of structure.

1.10.3 Single-sided Shepherding (Negative Diffusion)

Many of the previous sections have shown material getting more dense in various radial regions after passing by the moon. This type of behavior is seen in most of the simulations that have been done of rings with nearby perturbers going back to Hänninen and Salo (1994, 1995). It explains observed features like the enhanced optical depth of material at gap edges. It can also be used to explain the confinement of narrow rings in a way that is less dependent on the details of the perturbing moons than resonant models based on the ideas of Borderies et al. (1989) and Goldreich et al. (1995).

A full discussion of this process is laid out in Lewis et al. (2011). The basic idea is that collisions tend to prevent streamlines shearing through, and in order to do that, particle eccentricities damp and their semimajor axis values migrate, typically moving up density gradients. Figure 1.46 shows a simulation created just to explore this process. The left side of Fig. 1.46 shows the physical optical depth. The right side shows the semimajor axis distribution to highlight how much the radial distribution compressed. Note

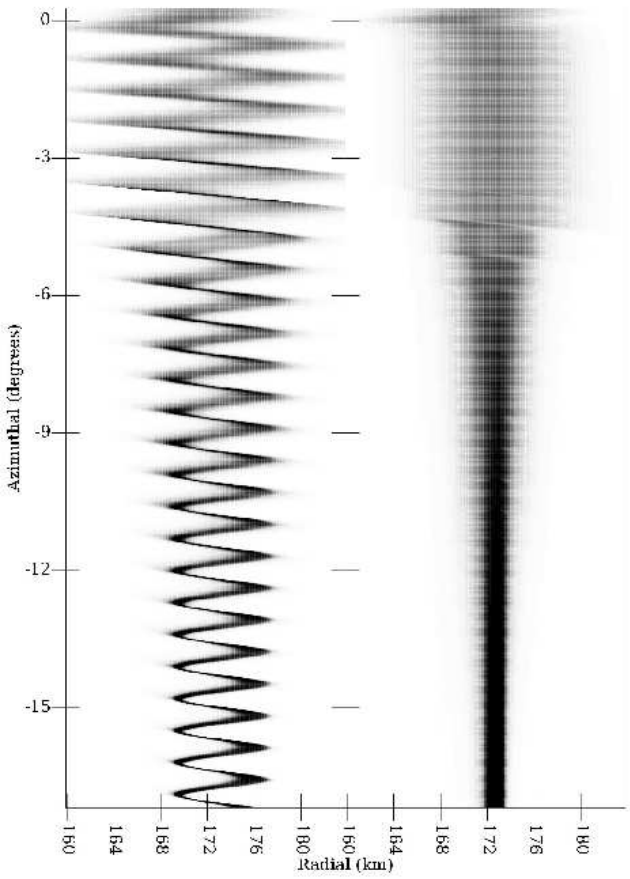

Figure 1.46 This figure shows the negative diffusion process in a narrow ring with a single perturber after one pass by the moon. The simulation included roughly 300,000 particles with radii between $4m$ and $13m$ pulled from a power law distribution with a differential slope of $q = 3$. It used the local cell boundary conditions (Sect. 1.10.1) with a Gaussian particle distribution in the radial direction with an average $\tau_D = 0.1$. Collisions were calculated, but not particle self-gravity. The left section shows optical depth of the physical particles. The right section shows density in (X, Y) or semimajor axis and mean anomaly. This shows how an initial distribution that was initially over 10 km in radial width can collapse by more than a factor of 5 just from organized particle collisions after being perturbed by a moon.

that this occurs after a single pass by the moon, so there can be no resonant effects. The value of Y_{crit} in this simulation is around 3.5°. That happens to be the location where we first see the modification in the semimajor axis distribution. Note that the streamline do not shear through. Instead, they consistently pile on top of one another in orbit after orbit. For 10-20 orbits after Y_{crit}, this leads to migration of semimajor axes and damping of eccentricities. Unlike with the inner edge region of the Encke gap simulation in section 1.10.1, the eccentricity gradient in the simulation becomes very strongly positive. This configuration remains roughly stable with almost no further damping of the eccentricity for many orbits.

1.11 Photometric modeling of dynamical simulations

The dynamical simulations described in above sections operate with surface density and particle number densities. However, these are not directly observable quantities, as the observations give the amount of sunlight reflected or transmitted through the rings, and the attenuation of stellar light when observed through the ring. The ring brightness is measured with I/F, the observed brightness in comparison to an ideal Lambert surface illuminated with the incident solar flux πF. In general, the I/F for a given ring region depends on the illumination elevation $B_\odot$, the viewing elevation B, and the corresponding azimuthal angles θ_0 and θ. Often the phase angle α between the illumination and viewing directions is specified instead of azimuthal angles,

$$\alpha = \cos^{-1}\left[\cos(\theta - \theta_0)\cos B \cos B_\odot + \sin B \sin B_\odot\right]. \quad (1.146)$$

In case of homogeneous systems this angle is sufficient. However, in case of self-gravitating systems also the direction with respect to self-gravity wakes matters, so that the azimuths themselves need to be specified. The line-of-sight optical depth relates to the fraction of light I/I_0 passing through the ring at a given direction (B, θ), with

$$\tau_{\rm LOS} = -\ln I/I_0 \quad (1.147)$$

Usually $\tau_{\rm LOS}$ is converted to the normal optical depth, corresponding to $B = 90^\circ$ with the formula

$$\tau_\perp = \tau_{\rm LOS} \sin B. \quad (1.148)$$

A quantitative comparison of dynamical models to observations requires calculating the photometric properties $(I/F, \tau_\perp)$ of the simulated particle fields for various illumination and observing geometries. A large amount of modeling has been done in the framework of classical radiative transfer, which however is strictly applicable only to low filling factor rings ($D_3 \to 0$) where particle separations are much larger than their sizes. If the rings are densely-packed and highly inhomogeneous, as suggested by dynamical models and many observations (see Dones et al. (1993)), an efficient modeling method is to use radiative ray tracing. Since the ring particles are much larger than visible light wavelength geometric optics can be used. For example the effects of dense packing (Salo and Karjalainen, 2003; Porco et al., 2008) and self-gravity wakes (Salo and Karjalainen, 2003; French et al., 2007b; Porco et al., 2008) have been studied with a combination of photometric and dynamical simulations.

1.11.1 Photometric ray tracing method

The idea in photometric ray-tracing simulations is to shoot a large number of photons (N_{phot}) from the light source and follow their paths through successive scatterings from particle surfaces until they leave the particle layer (Fig. 1.47). The simplest way to obtain the brightness would be to count the number of photons N_{obs} which escape to the solid angle $d\Omega_s$ around the observer's direction. However, even if relatively large $d\Omega_s$ is used (poor angular resolution), $N_{obs} \propto \Omega_s N_{phot}$

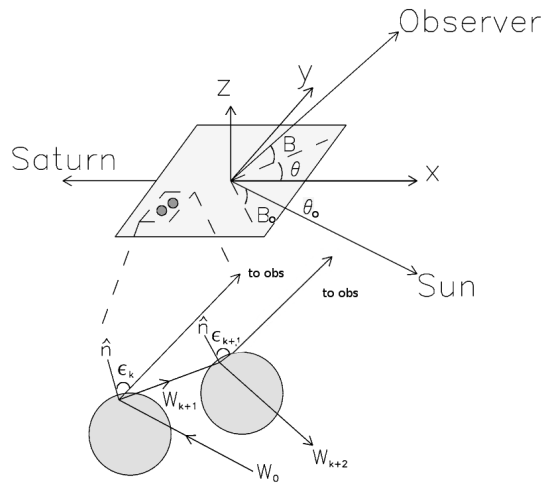

Figure 1.47 Schematic illustration of Monte Carlo ray tracing: a path of a photon, initially arriving from the direction of the sun, is shown through two successive scatterings from the surfaces of dynamical simulation particles. The post-scattering direction is Monte Carlo sampled from the single scattering phase function. In each scattering event also the probability of being scattered toward the observer is stored (taking into account the visibility of the observer's direction). Figure from Salo and Karjalainen (2003).

would be very small. Since the relative error in I/F is proportional to ${N_{obs}}^{-1/2}$, such a calculation would be very inaccurate even for a large N_{phot}. It is therefore crucial to combine such direct ray tracing with an indirect ("backward") method, where each scattering event, regardless of the direction of the post-scattering photon, is registered also from the viewpoint of the observer. If the scattering point is not blocked behind any ring particle, then the contribution of the scattering is added to the observed brightness by calculating what the probability of scattering to the direction of the observer would be. Now in principle every initial photon and scattering event contributes to the obtained I/F, and the relative uncertainty in I/F becomes proportional to ${N_{phot}}^{-1/2} << {N_{obs}}^{-1/2}$. Salo and Karjalainen (2003) estimated that the use of indirect method can speed-up the calculations by a factor > 1000, for the same accuracy of the results.

The obtained I/F will depend on the spatial distribution of particles, and on how the individual particles absorb and scatter light. The scattering can be defined either by specifying the surface element's reflection law [13] , or alternatively, via a particle phase function $P(\alpha)$ which describes the phase angle distribution of emerging photons from a particle as a whole; this corresponds to integrating over the surface elements of the illuminated hemi-sphere. The particle albedo A gives the total fraction of scattered radiation over all angles.

Photometric ray tracing methods applied to Saturn's rings have been described in detail in Salo and Karjalainen (2003) and in Porco et al. (2008). The main difference of the methods is in the handling of multiple scattering: in the former study in each scattering event a single photon is Monte Carlo sampled from the particle phase function (or surface element's scattering law) to represent the scattered light, whereas in the latter study the light ray is divided in a deterministic fashion into a bundle of rays after each scattering, and each of these new light rays is then followed (and redivided in the next scattering etc.). The two methods yield similar results, and they have both been verified by extensive comparisons to classical results in the low filling factor limit, both with Chandrasekhar (1960) analytic al single and multiple scattering results and with Dones et al. (1993) calculations with the doubling method. However, the method of Porco et al. (2008) is much more CPU-intensive for a given accuracy since it spends most of the time in the calculation of the higher scattering orders whose contribution to the total I/F is very small. Since the former Monte Carlo method spends less and less CPU time on each higher scattering order (or at most an equal amount), it can be extended to very high orders of scattering with very little extra CPU-time consumption. The same MC method has been recently adopted in Ciarniello et al. (2014) for testing Hapke (2008) theoretical models.

With the indirect method one can tabulate separately the contributions of different orders of scattering. There is thus no need to specify the albedo before the calculations, but instead one can re-construct the final I/F for any choice of albedo (Salo and Karjalainen 2003),

$$I = \sum_{k=1}^{max} A^k \Delta I_k, \tag{1.149}$$

where ΔI_k is the tabulated contribution from photons after k'th scattering and A is the particle albedo; during the calculation itself the albedo has been treated as unity so that the "weight" of the photon is kept constant over its path.

The calculation of the photon path through successive scatterings involves finding the intersection points with all particles along the current photon direction, and then choosing the closest intersection for the next scattering. If no intersections are found then the photon leaves the ring layer. The calculation has many similarities with the finding of particle impacts in dynamical simulations. In particular, if the simulated particle field contains a large number of particles it is crucial not to check every particle for a possible intersection. A simple but very efficient solution is to place a 2D grid on top of the particle field, and find first the grid cells the current photon path is crossing, and then search intersections only among the particles in these cells. A 3D grid can also be used, but since the systems of interest are

[13] The surface element's reflection law gives the probability $S(\mu_i, \phi_i, \mu_e, \phi_e) d\mu_e d\phi_e$ that a photon arriving the surface from the direction (μ_i, ϕ_i) will scatter to an interval $d\mu_e, d\phi_e$ around the direction (μ_e, ϕ_e), where $\mu_i = cos(i)$ and $\mu_e = cos(\epsilon)$, with i and e denoting the angles of incident and emergent rays with respect to the local normal of the surface element at the scattering point, and ϕ_i and ϕ_e are the corresponding azimuthal directions. A simple example is the Lambert reflection law, $S = S_L(\mu_i, \mu_e) = \mu_e/\pi$, which corresponds to a diffusively scattering surface whose brightness ($\sim S/\mu_e$) is independent of viewing direction. For a spherical particle the integration over the illuminated hemisphere gives the corresponding spherical particle Lambert phase function $P(\alpha) = (8/(3\pi)[\sin\alpha + (\pi - \alpha)\cos\alpha]$.

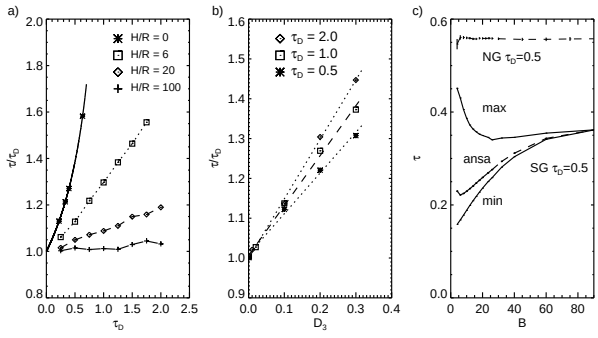

Figure 1.48 Relation between dynamical and photometric optical depth. In a) and b) homogeneous particle fields were simulated with various τ_D and H/R; the curve labeled $H/R = 0$ refers to a 2D monolayer. In c) the self-gravitating simulation depicted in Fig. 1.53 was analyzed, both along the wake major axis direction ("min"), perpendicular to it ("max"), and at the ring ansa. The curve labeled "NG" refers to a corresponding non-gravitating simulation with $\tau_D = 0.5$, yielding practically constant $\tau_\perp \approx 0.55$ for all B's. Redrawn from Salo and Karjalainen (2003); Salo et al. (2004).

usually very flattened this does not yield significant improvement over a 2D grid.

It is important to take accurately into account the periodic boundaries of the dynamical simulations: when the photon leaves the actual calculation region through its radial or tangential boundaries, it enters an identical copy of the particle field (see Eq. 1.8). Thus the photon should leave or enter the particle field only from below or above. In practice it is easier to handle the periodic image particles in terms of an image-photon re-entering the original particle field, so that there is no need to store any extra particle locations. The correct treatment of boundaries is particularly important in case of shallow illumination/viewing angles, where the light rays can, at least in principle, travel very long horizontal distances before leaving the particle layer. Similarly, taking into account periodic images is essential for the calculation of $\tau_{\rm LOS}$, in particular when the true probability of passing the particle layer is small: even a few missed intersections might then bias the result.

The brightness due to the illumination by the planet can be calculated in a similar manner as that due to Sun, except that the directions of the incoming photons are sampled from the solid angle extended by the planet at the distance and longitude of the dynamical simulation. A model for the brightness distribution of the planet's globe is needed: both in Salo and Karjalainen (2003) and in Porco et al. (2008), the Dones et al. (1993) model based on Barkstrom (1973) law was used.

1.11.2 Examples of photometric modeling

1.11.2.1 Dynamical and photometric optical depth

In low volume filling factor rings the vertical thickness of the system is much larger than particle radius: for a planarly homogeneous, vertically uniform system of identical particles we have $H/R = 4\tau_D/(3D_3)$. At the limit $D_3 \to 0$ the photometric and dynamical optical depths are equal. However, for vertically flattened systems the photometric $\tau_\perp$ exceeds τ_D. To justify these assertions, consider a vertically extended ring, and divide it into k layers each contributing $\Delta\tau_D = \tau_D/k$ to the total dynamical optical depth. The fraction of flight passing through a single layer is $1 - \Delta\tau_D$, and assuming that the layers are independent, the fraction of light passing through all layers is $(1 - \tau_D/k)^k \to \exp(-\tau_D)$ as $k \to \infty$. Clearly the two definitions of optical depth are then equal. On the other extreme, consider a 2D monolayer with $k = 1$. Now $\tau_\perp = -\ln(1 - \tau_D) > \tau_D$.

Figure 1.48, based on quantitative ray tracing calculations (Salo and Karjalainen, 2003), illustrates the dependence of $\tau_\perp/\tau_D$ on D_3 and τ_D. The particle fields in a) and b) were constructed by random placing of identical non-overlapping particles into a cuboidal volume. In the case of many particle thick layer ($H/R = 100$ in the figure; implies $D \sim 0.01$) we have $\tau_\perp \approx \tau_D$, but as H/R is reduced $\tau_\perp/\tau_D$ increases. Similar result holds also for realistic dynamical simulations with vertically non-uniform particle distribution, although in the case of size distribution the difference between $\tau_\perp$ and τ_D is somewhat decreased with increasing $R_{\rm max}/R_{\rm min}$. As a rule of thumb,

$$\tau_\perp/\tau_D \approx 1 + kD_3, \quad \text{with } k = 0.7 - 1.5, \tag{1.150}$$

in good agreement with the theoretically estimated enhancement factor of $1/(1 - D_3)$ (Esposito, 1979).

Photometric simulations also show that Eq. (1.148) for converting slanted $\tau_{\rm LOS}$ to $\tau_\perp$ works well for non-gravitating simulation systems, regardless of their vertical flattening (excluding strict monolayers, see Salo and Karjalainen (2003)). On the other hand, in the case of self-gravity (Fig. 1.48c), the deduced $\tau_\perp$ depends on the observing elevation and the direction with respect to wakes (Salo et al., 2004; Robbins et al., 2010; Tiscareno et al., 2010).

1.11.2.2 Non-zero volume density and enhanced single-scattering

Besides optical depth, non-zero volume density has a significant effect on the observed I/F. In general, a reduced ring vertical thickness leads to brightening of the reflected component and reduction of the transmitted one. In Fig. 1.11.2.1 the upper row shows the reflected and transmitted single scattering components for various values of D_3, in comparison to theoretical values at the limit $D_3 \to 0$,

$$\begin{aligned}
\left(\frac{I_{ss}}{F}\right)_{refl} &= \frac{AP(\alpha)\mu_0}{4(\mu+\mu_0)}\left(1 - \exp\left[-\tau_\perp(\frac{1}{\mu}+\frac{1}{\mu_0})\right]\right), \\
\left(\frac{I_{ss}}{F}\right)_{trans} &= \frac{AP(\alpha)\mu_0}{4(\mu-\mu_0)}\left(\exp\left[-\frac{\tau_\perp}{\mu}\right] - \exp\left[-\frac{\tau_\perp}{\mu_0}\right]\right) \\
&= \frac{AP(\alpha)\tau_\perp}{4\mu_0}\exp\left[-\frac{\tau_\perp}{\mu_0}\right], \ (\mu = \mu_0)
\end{aligned} \tag{1.151}$$

where $\mu_0 = |\sin B_\odot|$ and $\mu = |\sin B|$. The calculations in the figure use perpendicular illumination $B_\odot = 90^\circ$, but similar qualitative results hold for slanted illumination geometries. Also, Lambert phase function is assumed, although

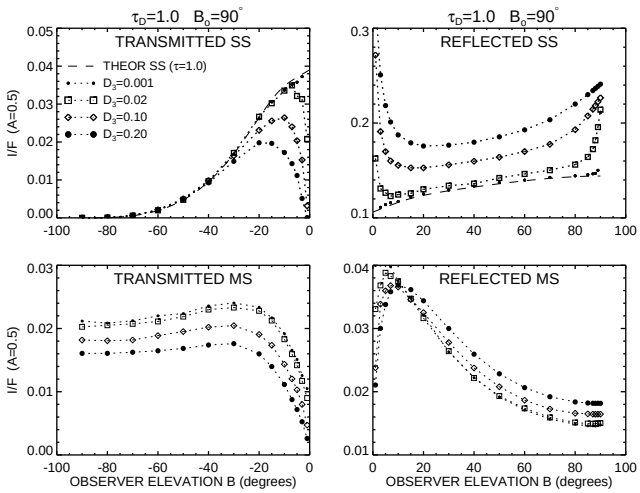

Figure 1.49 The effect of non-zero D_3 on the brightness of perpendicularly illuminated layer. Lambert phase function is used with A=0.5. Monte Carlo simulations with $\tau_D = 1$ for four different non-zero filling factors ($D_3 = 0.001, 0.02, 0.10, 0.20$) are compared. Single scattering and and multiply scattered fluxes are shown separately. Also shown are theoretical $I_{ss}(D_3 = 0)$ for $\tau_\perp = 1.0$. Figure from Salo and Karjalainen (2003).

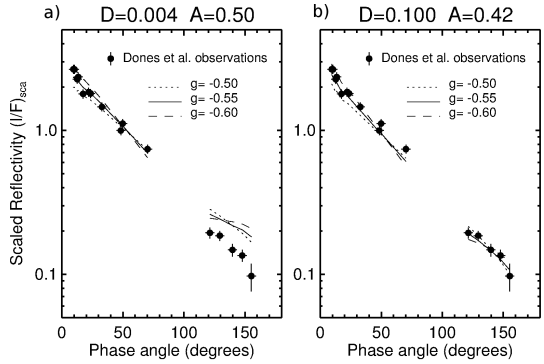

Figure 1.50 In a) Voyager observations at 122 500 km are compared with $D_3 \approx 0$ models, using same power-law phase functions as the classical radiative models in Dones et al. (1993). The anisotropy parameter $-1 \le g \le 1$ describes how strongly backward scattering the particles are: $g = -1$ means perfectly backscattering particle. A particle albedo $A = 0.5$ matches well the low α brightness but overestimates the high α brightness by a factor of 2. In b) $D_3 = 0.1$ and the models can now match both low and high α, provided that a somewhat smaller albedo is assumed. The plot uses scaled reflectivity $4(\mu + \mu_0)/\mu_0 \times (I/F)$, so that observations with different μ, μ_0 can be combined. Figure from Salo and Karjalainen (2003).

the ring particles are known to be more strongly backward-scattering (see Dones et al. 1993); the used phase function does not affect the relative change of I_{ss}. According to the figure, the calculated I_{ss} agrees with the theoretical value at $D_3 \approx 0$ but is significantly different for non-zero D_3: for homogeneous systems the enhancement in reflected I_{ss} at intermediate viewing elevations is about 30% for $D_3 = 0.2$. The enhancement is particularly strong at small phase angles (here close to $B = 90^\circ$), which is the well-known shadow-hiding opposition effect: as the zero phase angle is approached, the shadows cast by particles are hidden by the particles themselves. The shadow-hiding opposition peak extends to larger phase angles as D_3 increases, in good agreement with theoretical models in Lumme and Bowell (1981). The figure also shows an enhancement of I_{ss} near $B = 0^\circ$: this is somewhat specific to the perpendicular illumination assumed in the figure, and follows from the fact that at low viewing angles mainly the illuminated upper surfaces of the outermost particles are visible.

In simulations with realistic size distributions the enhancement of reflected I_{ss}/I_{theory} is somewhat smaller than with identical particles. This is related to the effective volume filling factor at the vertical layer where $\tau_{\rm LOS} \sim 1$ is achieved, which layer is responsible for most of the reflected light. As illustrated in Salo and Karjalainen (2003), the effective $D_3(\tau_{\rm LOS} = 1)$ gets smaller when more extended distributions are simulated. Because of this, the angular width of the opposition brightening is reduced, in good agreement with Hapke (1986) theoretical estimates. For the same reason, the opposition peak becomes narrower for lower viewing elevations: $\tau_{\rm LOS} \sim 1$ along shallow viewing is achieved at more rarefied outermost particle layers. In practice, dynamical/photometric simulations indicate that for the inter-particle shadow hiding (Salo and French, 2010)

$$HWHM \propto B, \tag{1.152}$$

where $HWHM$ is the Half-width half-maximum of the opposition peak. For example, assuming a "frosty" ice elasticity law, $\tau_D = 1.5$, $q = 3$ power law size distribution from 0.01 to 5 meters, implies $HWHM \approx 1.5^\circ$ and 3° for $B = 10^\circ$ and 25°, respectively. For a narrower distribution, with $R_{min} = 0.1$ meters, the simulated $HWHM$ is about a factor of 4 wider.[14]

Dones et al. (1993) pointed out problems when trying to explain Voyager observations of Saturn's ring photometry in the framework of classical radiative transfer, such as matching simultaneously the low and high phase angle I/F of the B and the inner and middle A ring: the rings appeared too dark at high α compared to what the classical models fitted at low α predicted (Fig. 1.50a). They proposed that the discrepancies stem from vertical flattening of the rings. Indeed, when including the enhancement of I_{ss} due non-zero D_3, the fit to the observed low phase I/F indicates a smaller A. This leads to reduced multiple scattering and thus smaller high phase brightness since this is mainly due to I_{ms}. Also, the nonzero D_3 itself reduces the high α multiple scattering compared to that in the classical limit: together these two effects bring the model and observations to a good match (Salo and Karjalainen, 2003, Fig. 1.50b). A similar conclusion was reached by Porco et al. (2008).

[14] The modeled $HWHM$ is sensitive to the way how it is determined: the numbers given in the text refer to simulated opposition enhancement for $0^\circ \le \alpha \le 90^\circ$. Fitting a linear-exponential model to $\alpha \le 10^\circ$ would yield 2-3 times narrower $HWHM$ (see Fig. 8 in Salo and French (2010)). Similar uncertainties can be even more severe when analyzing observed phase curves with sparse or uneven coverage of phase angles.

1.11.3 Opposition brightening

Saturn's rings show a strong opposition effect: a steep rise in I/F when the Sun-observer phase angle $\alpha \to 0^\circ$. Hubble Space Telescope observations during the 2005 opposition (French et al., 2007a) indicated that the brightness increase continues all the way to zero phase angle: the I/F increases by about 2/3 for $\alpha < 6^\circ$, half of this increase taking place within $\alpha < 0.5^\circ$. Most strikingly the opposition "spike" is demonstrated by the zero-phase Cassini images (Déau et al., 2013), which show a bright localized spot on the ring location centered at exact opposition.

Two main explanations for the Saturn ring's opposition brightening are i) the reduced amount of mutual *interparticle* shadowing, and ii) the *intrinsic* brightening of the ring particles themselves. As demonstrated by Fig. 1.11.2.1, the mutual shadow hiding effect is inevitable in a densely packed ring, although it depends on the spatial and size distribution of ring particles whether the brightening is as strongly peaked at $\alpha = 0^\circ$ as observed. Similarly, theoretical and laboratory studies suggest that icy particles exhibit a significant intrinsic brightening at $\alpha \to 0^\circ$ due to constructive interference between the incoming and outgoing light rays (coherent backscattering (CB), see e.g. Hapke, 1990; Muinonen et al., 1991; Mishchenko, 1992; Nelson et al., 2000). The expected magnitude and width of CB depends on the surface structure and optical properties of particles. Rough particle surfaces can also exhibit an intrinsic shadow hiding effect.

A long-term challenge has been to separate interparticle and intrinsic contributions to the opposition effect: unless this can be done it is not possible to extract reliable information of the particle surface properties by fitting the observed curves with theoretical CB models (e.g. Poulet et al., 2002; Déau, 2015), without including the interparticle shadow. Likewise, the early volume density estimates for Saturn's rings ($D_3 \approx 0.02$, Lumme et al. (1983)), based on interpreting the brightening solely in terms of interparticle shadow hiding were prone to lead to wrong answers.

The expected functional forms of the intrinsic and interparticle opposition effects are very similar (see e.g. Hapke, 1986, 1990), so that their contributions can not be entangled based on an individual phase curve. However, such a separation becomes possible with multi-wavelength observations covering a whole range of observing/illumination elevations. Namely, while the interparticle shadowing effect depends on B (Eq. (1.152)), it should be independent of the wavelength λ. On the other hand, CB is expected to depend on λ but not on B.

Salo and French (2010) exploited the full set of Saturn ring phase curves obtained with the Hubble Space telescope WFPC2 instrument during 1996-2005 (Cuzzi et al., 2002; Poulet et al., 2002; French et al., 2007a). In this data set, covering $4.5^\circ < B_{\rm eff} < 26^\circ$ in 5 broadband filters, the opposition brightening gets significantly more pronounced as $B_{\rm eff}$ decreases, confirming the expected contribution of interparticle shadowing.[15]. Fig. 1.51 illustrates this in terms of

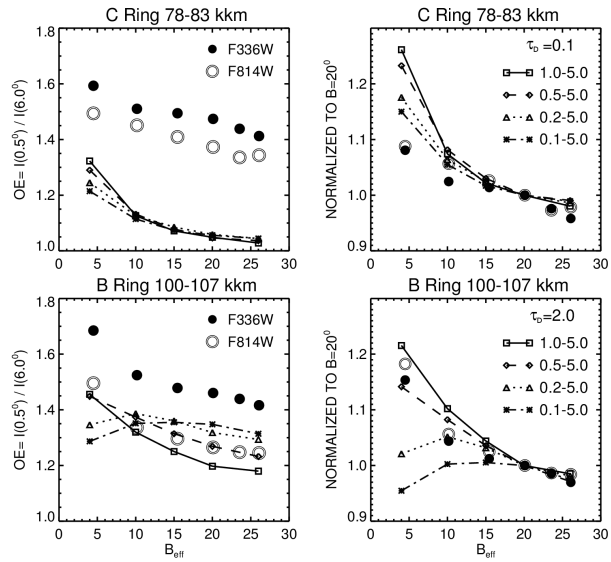

Figure 1.51 In the left: The symbols show the near-opposition brightness enhancement in HST observations of Saturn's C and B rings, measured in terms of $OE = I(\alpha = 0.5^\circ)/I(\alpha = 6^\circ)$. Lines indicate the modeled OE in size distribution simulations with different R_{min} (all have $R_{\rm max} = 5$m and $q = 3$). For the C ring model $\tau_D = 0.1$ and for the B ring models $\tau_D = 2$. In the right, the OE is normalized with that at 20° opening angle: note that normalized OE is practically independent of the wavelength. Figure from Salo and French (2010).

$OE = I(0.5^\circ)/I(6^\circ)$ for ring regions selected from the C and B rings. Both rings exhibit clearly larger OE at $B_{\rm eff} = 4.5^\circ$ compared to larger opening angles (left frames). The relative increase of OE with elevation is also independent of wavelength, as seen when OE is normalized to its value at $B_{\rm eff} = 20^\circ$ (right frames).

Fig. 1.51 shows also results from a grid of dynamical/photometric simulations performed for different τ_D's and different size distributions. For example, the $B_{\rm eff}$ dependence of the C ring OE is best matched with $\tau_D \sim 0.1$ and a wide size distribution with $R_{min}/R_{max} \lesssim 0.01$. On the other hand, the B ring comparisons suggest $\tau_D \gtrsim 2$ and a much narrower distribution $R_{min}/R_{max} \gtrsim 0.1$.

Figure 1.52 summarizes the results of photometric modeling of opposition brightening based on the Hubble Space telescope observations (Salo and French, 2010). When the ring opening angle is large (here 23°), the reflection is mainly due to particles in the densely packed equatorial plane: consequently the inter-particle shadow hiding contribution to the peak in I/F is relatively wide. For low $B_{\rm eff}$, the reflection is mainly due to the uppermost, low filling factor layers, which produce a stronger peak. The insert figures illustrate the final separations of observed phase curves into interparticle shadow hiding (dependent on $B_{\rm eff}$) and intrinsic contributions (same for all $B_{\rm eff}$). The intrinsic component is also separated to CB and surface shadow hiding components, using the Hapke (2002) models which are commonly applied

[15] The HST observations at slightly different B,$B_\odot$ are reduced to a geometrically corrected $(I/F)_{\rm corr}$ corresponding to an effective common elevation angle $B_{\rm eff}$, defined by $\mu_{\rm eff} = 2\mu\mu_0/(\mu+\mu_0)$ and $(I/F)_{\rm corr} = \mu_{\rm eff}/\mu\ (I/F)$. With this transformation the theoretical $(I/F)_{\rm corr}$ depends only on $B_{\rm eff}$.

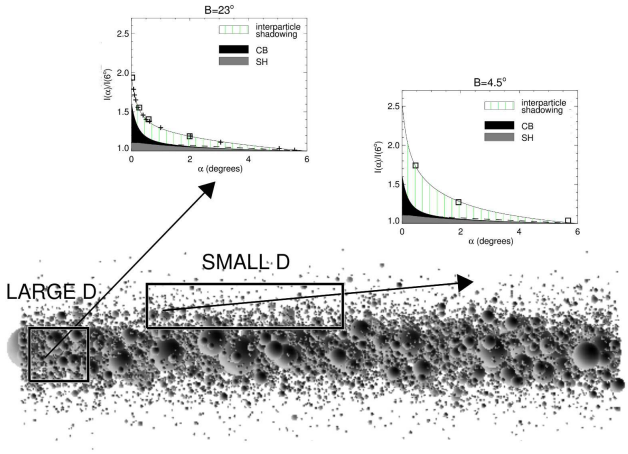

Figure 1.52 Illustration of the opening angle dependence of opposition phase curves (normalized by $I/F(\alpha = 6^\circ)$). A sideview of a dynamical $\tau_D = 1.25$ model is displayed, together with HST phase curves (symbols) observed at $B_{\rm eff} = 23^\circ$ and 4.5°. The modeled contributions of intrinsic (filled; both CB and SH) and interparticle contributions (hatched lines; mutual shadowing) are shown separately. In the fits, the intrinsic contribution is assumed to be independent of $B_{\rm eff}$, and the opening angle dependent part is fitted by comparison to a grid of simulation models. Figure from Salo and French (2010).

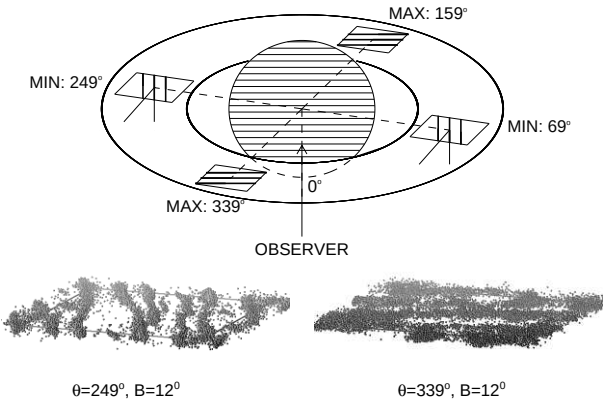

Figure 1.53 The effect of unresolved self-gravity wakes on global brightness: at intermediate ring opening angles the reflecting surface area has a minimum at longitudes where the rings are viewed along the average major axis of wakes, and correspondingly a maximum when wakes are viewed perpendicularly. Figure from Salo et al. (2004).

for the whole phase curve, without taking into account the mutual shadow hiding between particles. Since the interparticle shadow hiding accounts about half of the total opposition brightening, its inclusion has an effect on the estimated CB parameters.

The opposition effect has also been detected in the thermal phase curves obtained with the Cassini CIRS instrument (Altobelli et al., 2007; Altobelli et al., 2009). Such "thermal beaming" provides very important constrains for the shadow hiding models (both inter-particle and intrinsic) since there is no CB contribution (no phase coherence between illuminating photon and thermally re-radiated IR photons). Unfortunately, the analysis of observations (separating temperature effects from beam filling factor and IR-emissivity effects) and their modeling are very complicated (thermal models need to account, besides the instantaneous illumination and viewing geometries, also the thermal history of the ring layer and its constituent particles; see e.g Morishima et al. (2010, 2011). Therefore it not yet certain how the HWHM and amplitude of thermal opposition effect compare with the visual opposition effect.

1.11.4 Self-gravity wakes and azimuthal brightness asymmetry

Several types of observations support the existence of self-gravity wakes in Saturn's rings. Due to their small scale, $\lambda_T \sim 100$ meters, they are unresolved in direct images. Nevertheless, the wakes have a global signature on how the rings reflect and transmit light, since the reflecting surface area will depend on the viewing direction with respect to the average direction of wakes (see Fig. 1.53). Similarly, the illumination of wakes will depend on the longitude with respect to solar longitude.

The wakes provide a natural explanation to the A ring *azimuthal brightness asymmetry*, discovered already in 1950's (Camichel, 1958), intensively studied in the pre-Voyager era (Ferrin, 1975; Reitsema et al., 1976; Lumme et al., 1977; Thompson et al., 1981). In the ground-based observations the brightness at the mid A ring exhibits two symmetrical minima at the ring longitude $\theta_{min} \sim 70^\circ$ and $\sim 250^\circ$ with respect to sub-observer direction. The detailed analysis of low-phase Voyager images (Dones et al., 1993) showed that the amplitude of variations peaks very strongly in the mid-A ring, reaching a full amplitude $\approx 35\%$ in reflected light at the Saturnocentric distance of 128,000 km. The A ring asymmetry was also seen in Voyager transmitted light images (Franklin et al., 1987), whereas for the B ring no asymmetry was detectable. Wakes have also been inferred from the radar echo of rings (Nicholson et al., 2005), and from the way how Saturn's microwave radiation is transmitted through the rings (Dunn et al., 2004). Wakes also affect the ring opacity: the most detailed observations of wakes have been made with the Cassini stellar (Colwell et al., 2006, 2007; Hedman et al., 2007, 2014) and radio occultation measurements (Thomson et al., 2007). Wakes have also a clear signature on the ring's thermal emission probed with the Cassini CIRS instrument (Ferrari et al., 2009; Morishima et al., 2014).

The likely connection of azimuthal brightness asymmetry to Goldreich and Lynden-Bell (1965) and Julian and Toomre (1966) type self-gravity structures was pointed out already by Colombo et al. (1976) (see also Franklin et al., 1987; Dones and Porco, 1989; Dones et al., 1993). The first detailed comparisons between dynamical self-gravitating simulations and Voyager observations were made in Salo et al. (2004), using the photometric Monte Carlo method described above.

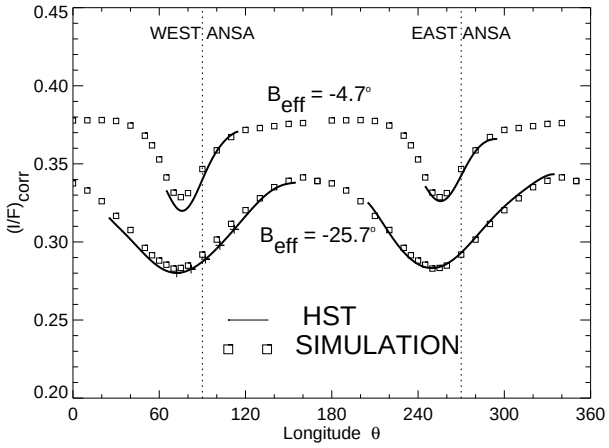

Figure 1.54 HST observations of the A ring azimuthal asymmetry at two different ring opening angles, with corresponding simulation models assuming identical "frosty ice" particles. Note the narrower minimum and the increased overall I/F for $B_{\rm eff} = 4.5°$. Figure from French et al. (2007b).

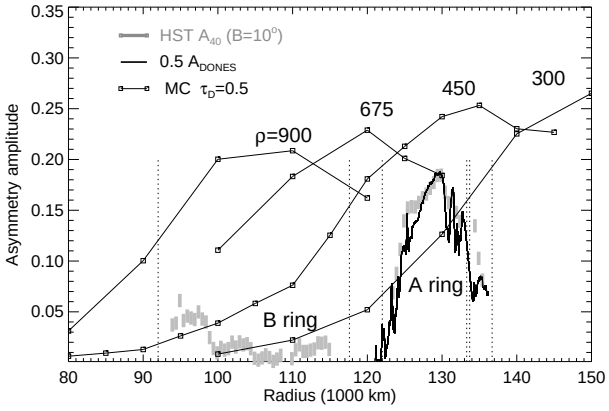

Figure 1.55 The observed radial dependence of the asymmetry amplitude is compared with dynamical simulations performed for various internal particle densities (labels indicate ρ in units of kgm^{-3}). Simulations assumed $\tau_D = 0.5$ and the "frosty ice" $\epsilon_{\rm n}$ model. Both the Hubble Space Telescope observations (filled light gray squares) and models correspond to $B_{\rm eff} = 10°$. The asymmetry amplitude from Voyager images (Dones et al., 1993) is shown as a solid line, multiplied by a factor of 0.5 to account for the difference in definitions of asymmetry amplitude. Figure from French et al. (2007b).

It was shown that the trailing self-gravity wakes, systematically tilted by about 20° with respect to the local tangential direction can explain in a quantitative way the A ring asymmetry amplitude and longitude of minimum, both in the reflected and transmitted light observations (in the latter case one also needs to take into account the Saturn-shine contribution which also depends on ring longitude). A somewhat surprising result was (and still is) that the observed θ_{min} is better matched by dynamical models consisting of identical particles, than by the presumably more realistic models with an extended size distribution. The shift $\Delta\theta_{min} \approx 5°$ between size distribution and identical particle models, is the same as the difference in the wake pitch angle implied by the auto-correlation analysis of simulated wakes (see Fig. 1.25). Same conclusion was reached in French et al. (2007b) when comparing identical particle and size distribution simulations with the HST observations; similar shift is also seen in Porco et al. (2008) models of Cassini phase curves.

French et al. (2007b) carried out detailed analysis of the azimuthal brightness variations on the above described Hubble Space Telescope data set, covering the full elevation and phase angle ranges accessible from Earth. The change in the asymmetry amplitude, and the width and location of the brightness minima were all found to be in accordance with the predictions of the dynamical wake models (see Fig. 1.54). For example, the asymmetry amplitude is largest at $B_{\rm eff} \sim 10°$: when $B_{\rm eff} \to 0°$ the sparse inter-wake regions are not anymore visible, while for larger $B_{\rm eff}$ the reflecting surface area is less sensitive to azimuthal orientation. The observed width of minimum gets narrower at small $B_{\rm eff}$ which is expected since then the inter-wake gaps are visible only when viewed very precisely along the major axis of wakes. Similar very narrow peak is seen in the amount transmitted light in the low elevation (3.45°) VIMS stellar occultations (Hedman et al., 2007). Moreover, the HST observations made it possible to fully separate the dependence of θ_{min} on the sun-earth longitude difference.

The presence of self-gravity wakes explains also the A-ring *inverse tilt effect* (the overall I/F drops with $B_{\rm eff}$; Cuzzi et al., 2002): with increasing opening angle more light leaks through the gaps between the wakes. In contrast to the A ring, the B ring has a strong *positive tilt effect*, its brightness increasing by $\sim 30\%$ between $B_{\rm eff} = 4° - 26°$. Early on, this increase was interpreted in terms of enhanced contribution from multiple scattering at higher $B_{\rm eff}$ (Esposito and Lumme, 1977; Lumme et al., 1983), but as shown in detail in Salo and French (2010) the observed positive tilt effect follows naturally by the same models which account for the elevation angle dependent opposition effect: in ground-based observations at fixed small α, the brightness increases with opening angle since the opposition brightening extends to larger α for larger $B_{\rm eff}$ (see Eq. 1.152).

The Hubble Space telescope observations in French et al. (2007b) confirmed the very strong peaking of asymmetry amplitude in the mid A-ring, matching very well the Dones et al. (1993) measurements. Weak asymmetry was also discovered in the inner B ring, consistent with the UVIS stellar occultation observations (Colwell et al., 2007). Fig. 1.55 shows the observed HST asymmetry amplitude as a function of Saturnocentric distance, and also compares it to a set of dynamical and photometric simulation models. The simulations assume different internal densities of particles (varying from solid ice density 900 kgm^{-3} to 1/3 of solid ice density), while all the other simulation parameters are kept fixed. Depending on the assumed internal density of the particles, the self-gravity wake structure emerges at different distances (at certain r_h, so that $a \propto \rho^{-1/3}$, see Fig. 1.24) leading to growth of asymmetry amplitude. With increasing distance, the wakes become clumpier, eventually degrading into par-

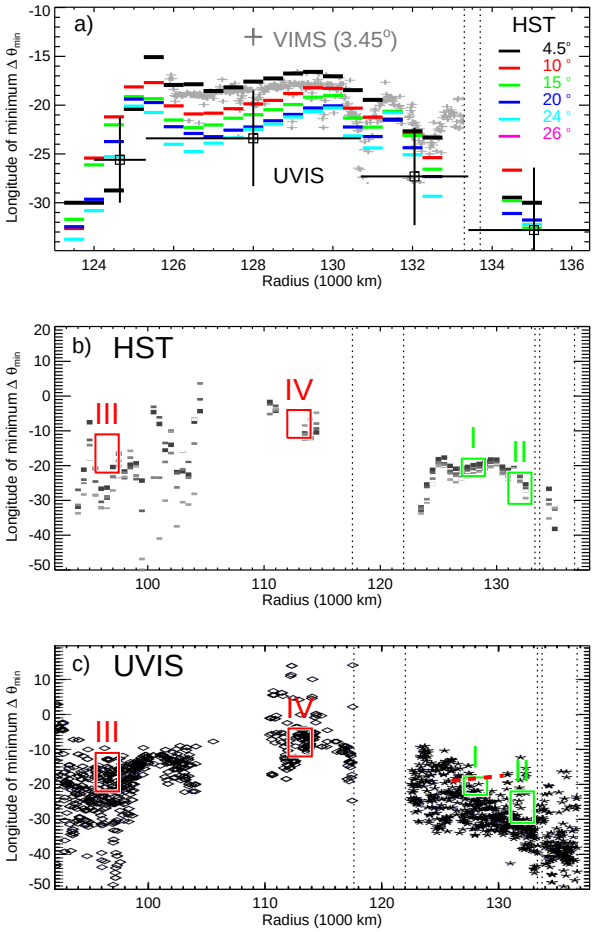

Figure 1.56 a) The longitude of brightness minimum (wrt ring ansa) in the Hubble Space Telescope observations of the A ring (French et al., 2007b), for different ring opening angles $B_{\rm eff}$. Also shown are wake orientations derived from VIMS (grey symbols; Hedman et al., 2007) and UVIS (large crosses; Colwell et al., 2006) occultation measurements. In b) a similar plot of HST, and in c) of UVIS observations, covering both the B and A rings. The labeled boxes indicate four simulation models explored in (French et al., 2007b): the models are illustrated in Fig. 1.57. The height of the box indicates the range of simulated $\Delta\theta_{min}$ for $4^\circ < B_{\rm eff} < 26^\circ$. Figure redrawn from French et al. (2007b), Colwell et al. (2007), and Hedman et al. (2007).

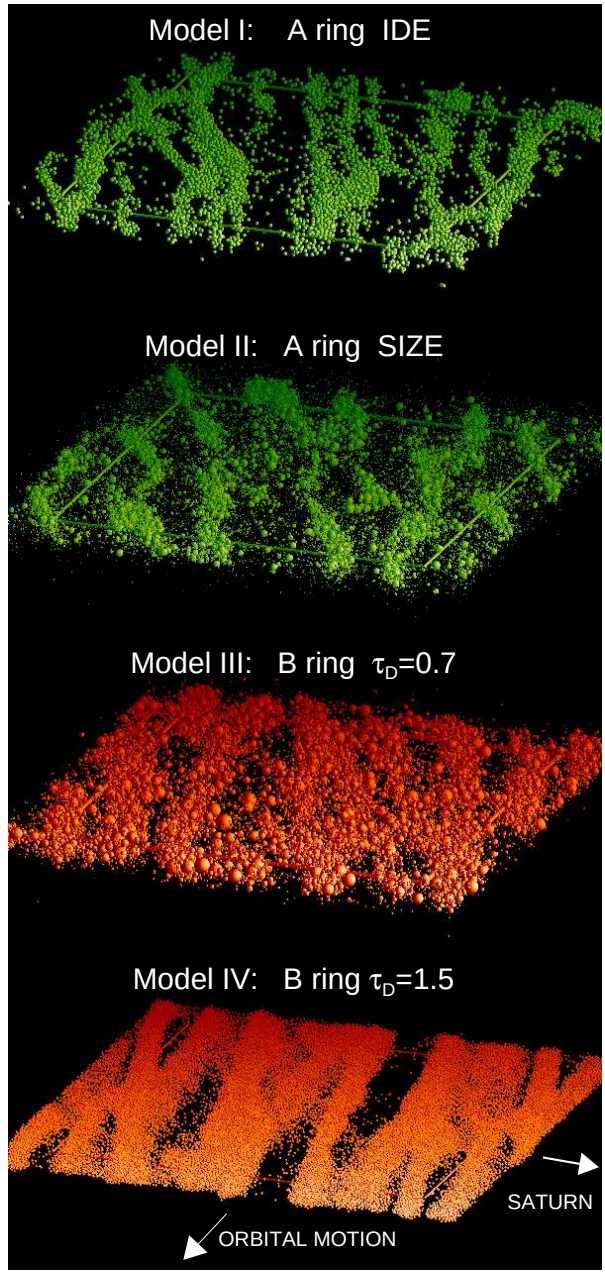

Figure 1.57 Four different dynamical simulations models (viewed from 20° elevation) illustrating the possible self-gravity wake structure at various Saturn ring locations. Photometric modeling of these simulations yield the longitude of asymmetry minima indicated in Fig. 1.56. Model I is for the peak of the A ring azimuthal brightness asymmetry, and Model II for the region beyond the maximum asymmetry; the models differ only in the adopted size distribution (identical particles vs. a size distribution with $R_{max}/R_{min} = 10$; in both models $\tau_D = 0.5$; calculations carried out for $a = 130,000$ km.) Models III and IV are for the B ring: size distribution with $\tau_D = 0.7$, and identical particles with $\tau_D = 1.5$, respectively (calculations for $a = 100,000$ km). All models assume ρ=450 kgm^{-3} and "frosty" ice elasticity. Redrawn from French et al. (2007b).

ticle aggregates. This reduced the longitude-dependence of the reflecting area and thus the amplitude of asymmetry.

Clearly, the distance dependence of the asymmetry amplitude in the simulation models of Fig. 1.55, following solely from the slow change in the tidal environment, is much too weak compared to the observed strong peaking of amplitude at the mid A-ring. As demonstrated in French et al. (2007b), using higher τ_D, different $\epsilon_{\rm n}(v_n)$ or different size distributions would modify the trends, if the parameters are allowed to vary with distance. For example, the rapid drop of the asymmetry amplitude at the outer A-ring could be related to a rapid increase in the fractional amount of small particles, suggested to rise due to higher impact speeds associated with the stronger perturbations by external satellites

(Dones et al., 1993), or perhaps by the self-gravity wakes themselves (Salo and Schmidt, 2007).

The longitude of brightness asymmetry minimum provides information of the properties of the self-gravity wakes, and also gives clues of the possible co-existence of wakes and overstable oscillations, even when the latter ones can not be directly resolved. Namely, while the pitch angle of wakes is limited to values larger than $\phi_{pitch} \approx 14^\circ$ (the asymptotic value in Keplerian velocity field, see Fig. 1.9), the overstable oscillations are very accurately axisymmetric ($\phi_{pitch} = 0^\circ$). Therefore, any effective pitch angle between these values is likely to indicate the presence of both wakes and overstability. Figures 1.56 and 1.57 illustrate the trends of ϕ_{pitch} with distance: the former figure collects wake orientation estimates from HST (French et al., 2007b), UVIS (Colwell et al., 2006, 2007), and VIMS (Hedman et al., 2007) measurements, while the latter figure shows models more or less matching the wake orientation (and the amplitude of HST brightness asymmetry amplitude) at four selected locations.

The uppermost frame in Fig. 1.56 shows the longitude of minimum brightness in the A ring, for HST observations with different ring opening angles. The longitude is given with respect to the ring ansa, thus measuring the pitch angle of the trailing wakes ($\phi_{pitch} = -\Delta\theta_{\rm min}$). The minimum moves closer to ansa when moving toward the distance where the wakes are most prominent (the asymmetry amplitude has its maximum at $a \sim 130{,}000$ km). There is a also a systematic shift in longitude toward ansa with decreasing $B_{\rm eff}$: the outer portions of wakes, with smaller ϕ_{pitch} become then more dominant. The model I in Fig. 1.57 reproduces these trends. Beyond $a = 130{,}000$ km, the minimum moves rapidly away from the ansa, which is consistent with an increased width of the particle size distribution (Model II in Fig. 1.57). The HST observations are in good agreement with the stellar occultation measurements, where the wake orientation is deduced by fitting the transmission profiles from several occultations with those implied by a geometric slab models (either with rectangular, Colwell et al. (2006), or elliptical cross-sections, Hedman et al. (2007)). The apparent difference between ϕ_{pitch} deduced from VIMS and UVIS is likely to follow solely from the different elevation angles of the analyzed occultations: the VIMS results indicated in the figure are from an elevation of 3.45°, and they agree very well with the low $B_{\rm eff}$ HST measurements; UVIS occultations corresponds typically to $B > 20^\circ$ and are consistent with high $B_{\rm eff}$ HST measurements.

The lower frames of Fig. 1.56 show the $\Delta\theta_{\rm min}$ for both B and A rings, the HST (b) and UVIS measurements (c) showing good general agreement. In the inner B ring the deduced wake orientation is more or less similar to the mid A ring, though the amplitude is smaller; the reduction is amplitude is consistent with the reduced role of self-gravity when closing the planet (Model III in Fig. 1.57). Interestingly, in both dataset the region at 110,000 km - 115,000 km has $\phi_{pitch} \approx 10^\circ$. This is consistent with higher τ_D B ring simulations (Model IV) where overstable oscillation are superposed on self-gravity wakes.

1.12 Summary

1.12.1 What has been covered

In this chapter we have reviewed the basic ingredients of local planetary ring simulations: the use of linearized dynamical equations in a co-moving coordinate system, the shearing periodic boundaries, the modeling of particle impacts, and the calculation of self-gravity. Impacts were treated both as instantaneous velocity changes ("hard sphere" collisions), and in terms of visco-elastic forces affecting partially overlapping colliding particles ("soft spheres"). We described different methods for calculating the ring self-gravity, including the often-used approximation in terms of enhanced n_z/n. The establishment of local energy balance between collisional dissipation and viscous gain (including local, nonlocal and gravitational contributions) was discussed in quite some detail, as well as how to measure from simulations various pressure tensor related quantities characterizing this steady state.

Extensive numerical simulation examples were given, and our aim was to go systematically through the main free parameters of the models, the elasticity and friction in impacts, the size distribution of particles, and their internal density. When possible, the results were given a hydrodynamic interpretation (see Stewart et al., 1984; Schmidt et al., 2009) The central theme was to illustrate how the ν vs. τ_D relation, deduced from small scale simulations, can be used to make predictions concerning the viscous stability properties of the ring system. We then gave examples of how the predicted viscous overstabilities and instabilities manifest in larger-scale simulations. Also, we presented a systematic survey of the expected self-gravity wake structure, when using two quite different elasticity laws representing the range of uncertainty for the ring particle physical properties. The Bridges et al. (1984) "frosty ice" models implies strongly flattened rings ($H \sim 10$ m at all τ_D) susceptible to oscillatory instability (viscous overstability) and the formation of gravitational wakes, whereas the Hatzes et al. (1988) "smooth ice" model leads to multilayer rings ($H \sim 100$ m at low τ_D) where self-gravity wake structure is harder to obtain, but which might be susceptible to viscous amplification of fluctuations (viscous instability). The conditions for the formation of gravitationally bound particle aggregates were also reviewed in detail, and several simulation examples were given of the behavior ring edges near perturbing moons residing in ring gaps.

Finally, we discussed the photometric ray tracing modeling of the particle fields produced by dynamical simulations, and illustrated how the dynamical models for dense flat rings (with $D_3 \sim 0.1$) explain in a natural manner many photometric observations of the rings, like the azimuthal brightness asymmetry related to self-gravity wakes, and the overall deviations from classical radiative transfer theory applicable at the limit $D_3 = 0$. Also, we demonstrated the importance to take into account the mutual shadow hiding effect when deducing particle intrinsic properties from the modeling of opposition brightening.

1.12.2 Material not covered

Several important aspects of ring dynamics have not been covered by this review, both related to physical mechanisms operating in planetary rings, and to technical aspects of simulations. For example, we have not discussed in any detail the effects of adhesive forces and particle coagulation and fragmentation (see e.g. Albers and Spahn, 2006; Perrine et al., 2011; Perrine and Richardson, 2012): such processes might have a fundamental role in determining the ring's particle size distribution (Brilliantov et al., 2015). Also, while the influence of moons for the gap edges has been treated, we have not described dynamical/photometric simulations of propeller structures around embedded moonlets (Sremčević et al., 2007), or simulations addressing rings perturbed by satellite resonance perturbations, either by using azimuthally complete rings (Hänninen and Salo, 1994, 1995) or with local calculation regions with a time-variable radial width (Mosqueira, 1996), or by applying streamline formalisms (Hahn and Spitale, 2013). On the technical side, while we have briefly mentioned parallelization and tree method for gravity calculations, we have not described in detail current codes utilizing such methods, like *pkdgrav* (Richardson et al., 2000; Porco et al., 2008), or the publicly available *rebound* code (Rein and Liu, 2012). Similarly, we have not covered simulations addressing the large scale evolution of rings, in terms of viscous radial evolution (Charnoz et al., 2010), or via ballistic transport of mass and angular momentum (Durisen et al., 1989; Estrada et al., 2015). Some of these aspects are covered in more details in the other chapters.

1.12.3 Some open questions

There are several open problems in the ring dynamics, which in principle can be tackled by improved local simulations.

• *What is behind the ubiquitous fine-structure observed in Saturn's rings?*

The viscous overstability of dense, strongly flattened systems is the leading candidate for the regular axisymmetric density variations seen in the inner A ring and the B ring. As such, this would favor dissipative particle impacts ("frosty ice") and a very low internal density of particles ($\rho \lesssim 300$ kgm^{-3}). Nevertheless, viscous instability might provide an attractive alternative for the almost bimodal variations seen in many locations of the B ring. In its simplest form it would seem to require very elastic particles and dynamically hot rings, which is not easy to reconcile with the existence of self-gravity wakes. However, the size-dependent viscous instability, observed in N-body simulations under certain conditions (smaller particles more dissipative than larger ones) can lead to a much richer structure. This mechanism is certainly worth a deeper study.

• *What is the interplay between self-gravity wakes and viscous overstability?*

Inclusion of self-gravity leads to steeper density-viscosity relation, and is thus expected to promote viscous overstability. Indeed, this is seen when the effect of self-gravity is approximated via enhanced n_z/n. However, when full self-gravity is included the inclined self-gravity wakes, which have roughly the same radial scale, seem to suppress the growth of axisymmetric overstable oscillations. Is this due to the limitations in the current fully self-gravitating simulations? Another intriguing aspect of overstable oscillations is their azimuthal coherence length: do the oscillation wavetrains extend continuosly over the whole circumference of the rings? Clearly, local simulations are not suitable for answering this - further theoretical work is needed.

• *What is the relation between ring optical depth and surface mass density variations?*

Several recent studies have indicated that there is a poor correlation between ring optical depth and surface density (Baillié et al., 2011; Tiscareno et al., 2013b; Hedman and Nicholson, 2016). For example, the C ring plateaus are found to have similar Σ as the background ring, regardless of having a factor of four larger $\tau_\perp$ (Hedman and Nicholson, 2014). The easiest explanation would be a larger fraction of smaller particles in the plateau: such a difference might arise due to size-selective viscosity instability described in Sect. 1.8.2.1. However, this is not supported by the radio occultation measurements, which indicate that the plateaus have a larger average particle size (Cuzzi et al., 2009). Differences in particle densities and compositions have been suggested (Hedman and Nicholson, 2014) but no definite model yet exists.

• *Why does the amplitude of azimuthal asymmetry peak so strongly in the mid A ring?*

The effective viscosities obtained from the damping of the A ring weak density waves (Tiscareno et al., 2007) are consistent with the viscosities estimated from self-gravitating simulations (Daisaka et al., 2001, Sect. 1.7.2.2) performed with solid ice density. Likewise, the outer edge of the A ring fits well to the distance where frosty ice particles with $\rho \approx 900$ kgm^{-3} start rapidly collapsing into gravitationally bound aggregates. Still, such parameters would imply much stronger self-gravity wake structure than deduced from photometric modeling, with a maximum brightness amplitude attained much closer to planet, and with a much shallower dependence on distance. Indeed, modeling of azimuthal asymmetry seems to work best for internal density $\rho \approx 450$ kgm^{-3}. Another puzzle with azimuthal asymmetry is the longitude of brightness minimum, which matches very well with models of identical particles, but deviates clearly from that currently predicted by size distribution models.

• *The combination of photometric and dynamical simulations is a very powerful modeling tool, which needs to be applied to Cassini data in a similar manner as the HST data has been analyzed.* The superior imaging resolution ($\sim$ *km* in comparison to $\sim 10^3$ km in HST) and coverage of wide range of geometries provides extremely strong constraints for any dynamical model.

Improved simulation models, including both adhesion and fully consistent self-gravity, and allowing for the possibility of size-dependent or otherwise variable particle properties (elasticity, friction, internal density) are clearly needed for better understanding of the real planetary rings.

REFERENCES

Albers, N., and Spahn, F. 2006. The influence of particle adhesion on the stability of agglomerates in Saturn's rings. *Icarus*, **181**, 292–301.

Albers, N., Sremcevic, M., and Esposito, L. W. 2015. A new moon-induced structure. Page 874 of: *European Planetary Science Congress 2015*, vol. 10.

Altobelli, N., Spilker, L., Pilorz, S., Brooks, S., Edgington, S., Wallis, B., and Flasar, M. 2007. C ring fine structures revealed in thermal infrared. *Icarus*, **191**, 691–701.

Altobelli, N., Spilker, L., Pilorz, S., Leyrat, C., Eddgington, S., Wallis, B., and Flandes, A. 2009. Thermal phase curves observed in Saturn's main rings by Cassini-CIRS: Detection of an opposition effect? *Geophys. Res. Lett.*, **36**, L10105.

Araki, S. 1988. The dynamics of particle disks. II. Effects of spin degrees of freedom. *Icarus*, **76**, 182–198.

Araki, S. 1991. The dynamics of particle disks III. Dense and spinning particle disks. *Icarus*, **90**, 139–171.

Araki, S., and Tremaine, S. 1986. The dynamics of dense particle disks. *Icarus*, **65**, 83–109.

Attree, N. O., Murray, C. D., Cooper, N. J., and Williams, G. A. 2012. Detection of Low-velocity Collisions in Saturn's F Ring. *Astrophys. J. Lett.*, **755**, L27.

Baillié, K., Colwell, J. E., Lissauer, J. J., Esposito, L. W., and Sremčević, M. 2011. Waves in Cassini UVIS stellar occultations. 2. The C ring. *Icarus*, **216**, 292–308.

Barbara, J. M., and Esposito, L. W. 2002. Moonlet collisions and the effects of tidally modified accretion in Saturn's F ring. *Icarus*, **160**, 161–171.

Barkstrom, B. R. 1973. A comparison of the Minneart reflectance law and the reflectance from a nonconservative isotropic scattering atmosphere. *J. Geophys. Res.*, **78**, 6370–6372.

Barnes, J., and Hut, P. 1986. A hierarchical $O(N \log N)$ force-calculation algorithm. *Nature*, **324**, 446–449.

Belleman, Robert G., Bdorf, Jeroen, and Zwart, Simon F. Portegies. 2008. High performance direct gravitational N-body simulations on graphics processing units II: An implementation in CUDA. *New Astronomy*, **13**(2), 103 – 112.

Borderies, N., Goldreich, P., and Tremaine, S. 1985. A granular flow model for dense planetary rings. *Icarus*, **63**, 406–420.

Borderies, N., Goldreich, P., and Tremaine, S. 1989. The formation of sharp edges in planetary rings by nearby satellites. *Icarus*, **80**, 344–360.

Brahic, A. 1977. Systems of colliding bodies in a gravitational field. I - Numerical simulation of the standard model. *Astron. & Astrophys.*, **54**, 895–907.

Bridges, F.G., Hatzes, A.P., and Lin, D.N.C. 1984. Structure, stability and evolution of Saturn's rings. *Nature*, **309**, 333–338.

Brilliantov, N., Krapivsky, P.L., Bodrova, A, Spahn, F, Hayakawa, H., Stadnichuk, V., and Schmidt, J. 2015. Size distribution of particles in Saturn's rings from aggretion and fragementation. *PNAS*, **112**, 9536–9541.

Brilliantov, N. V., Albers, N., Spahn, F., and Pöschel, T. 2007. Collision dynamics of granular particles with adhesion. *Phys. Rev. E*, **76**(5), 051302.

Brilliantov, N.V., Spahn, F., Hertzsch, J.-M., and Pöschel, T. 1996. Model for collisions in granular gases. *Phys. Rev. E*, **53**, 5382–5392.

Burns, J.A., and Cuzzi, J. N. 2006. Our local astrophysical laboratory. *Science*, **312**, 1753–1755.

Camichel, H. 1958. Mesures photométriques de Saturne et de son anneau. *Annales d'Astrophysique*, **21**, 231–242.

Canup, R. M. 2010. Origin of Saturn's rings and inner moons by mass removal from a lost Titan-sized satellite. *Nature*, **468**, 943–946.

Chandrasekhar, S. 1960. *Radiative transfer*. New York: Dover.

Chandrasekhar, S. 1969. *Ellipsoidal Figures of Equilibrium*. Yale Univ. Press.

Charnoz, S., Morbidelli, A., Dones, L., and Salmon, J. 2009. Did Saturn's rings form during the Late Heavy Bombardment? *Icarus*, **199**, 413–428.

Charnoz, S., Salmon, J., and Crida, A. 2010. The recent formation of Saturn's moonlets from viscous spreading of the main rings. *Nature*, **465**, 752–754.

Charnoz, S., Crida, A., Castillo-Rogez, J. C., Lainey, V., Dones, L., Karatekin, Ö., Tobie, G., Mathis, S., Le Poncin-Lafitte, C., and Salmon, J. 2011. Accretion of Saturn's mid-sized moons during the viscous spreading of young massive rings: Solving the paradox of silicate-poor rings versus silicate-rich moons. *Icarus*, **216**, 535–550.

Ciarniello, M., Capaccioni, F., and Filacchione, G. 2014. A test of Hapke's model by means of Monte Carlo ray-tracing. *Icarus*, **237**, 293–305.

Colombo, G., Goldreich, P., and Harris, A. W. 1976. Spiral structure as an explanation for the asymmetric brightness of Saturn's A ring. *Nature*, **264**, 344–345.

Colwell, J. E., Esposito, L. W., and Sremčević, M. 2006. Self-gravity wakes in Saturn's A ring measured by stellar occultations from Cassini. *Geophys. Res. Lett.*, **33**, L07201.1–L07201.4.

Colwell, J. E., Esposito, L. W., Sremčević, M., Stewart, G. R., and McClintock, W. E. 2007. Self-gravity wakes and radial structure of Saturn's B ring. *Icarus*, **190**, 127–144.

Crida, A., and Charnoz, S. 2012. Formation of Regular Satellites from Ancient Massive Rings in the Solar System. *Science*, **338**, 1196.

Cundall, P. A., and Strack, O. D. L. 1979. A discrete numerical model for granular assemblies. *Geotechnique*, **29**, 47–65.

Cuzzi, J., Clark, R., Filacchione, G., French, R., Johnson, R., Marouf, E., and Spilker, L. 2009. Ring Particle Composition and Size Distribution. Page 459 of: Dougherty, M. K.,

Esposito, L. W., and Krimigis, S. M. (eds), *Saturn from Cassini-Huygens*.

Cuzzi, J. N., Durisen, R. H., Burns, J. A., and Hamill, P. 1979. The vertical structure and thickness of Saturn's rings. *Icarus*, **38**, 54–68.

Cuzzi, J. N., French, R. G., and Dones, L. 2002. HST Multicolor (255-1042 nm) Photometry of Saturn's Main Rings. I: Radial Profiles, Phase and Opening Angle Variations, and Regional Spectra. *Icarus*, **158**, 199–223.

Cuzzi, J. N., Burns, J. A., Charnoz, S., Clark, R. N., Colwell, J. E., Dones, L., Esposito, L. W., Filacchione, G., French, R. G., Hedman, M. M., Kempf, S., Marouf, E. A., Murray, C. D., Nicholson, P. D., Porco, C. C., Schmidt, J., Showalter, M. R., Spilker, L. J., Spitale, J. N., Srama, R., Sremčević, M., Tiscareno, M. S., and Weiss, J. 2010. An Evolving View of Saturn's Dynamic Rings. *Science*, **327**, 1470–1475.

Daisaka, H., and Ida, S. 1999. Spatial structure and coherent motion in dense planetary rings induced by self-gravitational instability. *Earth, Planets, and Space*, **51**, 1195–1213.

Daisaka, H., Tanaka, H., and Ida, S. 2001. Viscosity in a dense planetary ring with self-gravitating particles. *Icarus*, **154**, 296–312.

Déau, E. 2015. The opposition effect in Saturn's main rings as seen by Cassini ISS: 2. Constraints on the ring particles and their regolith with analytical radiative transfer models. *Icarus*, **253**, 311–345.

Déau, E., Dones, L., Charnoz, S., West, R. A., Brahic, A., Decriem, J., and Porco, C. C. 2013. The opposition effect in Saturn's main rings as seen by Cassini ISS: 1. Morphology of phase functions and dependence on the local optical depth. *Icarus*, **226**, 591–603.

Dilley, J.P. 1993. Energy loss in collisions of icy spheres: Loss mechanism and size-mass dependence. *Icarus*, **105**, 225–234.

Dones, L. 1991. A recent cometary origin for Saturn's rings? *Icarus*, **92**, 194–203.

Dones, L., and Porco, C. C. 1989. Spiral density wakes in Saturn's A ring? Page 929 of: *Bull. American Astron. Soc.*, vol. 21.

Dones, L., Cuzzi, J. N., and Showalter, M. R. 1993. Voyager Photometry of Saturn's A Ring. *Icarus*, **105**, 184–215.

Dunn, D. E., Molnar, L. A., Niehof, J. T., de Pater, I., and Lissauer, J. J. 2004. Microwave observations of Saturn's rings: anisotropy in directly transmitted and scattered saturnian thermal emission. *Icarus*, **171**, 183–198.

Durisen, R. H., Cramer, N. L., Murphy, B. W., Cuzzi, J. N., Mullikin, T. L., and Cederbloom, S. E. 1989. Ballistic transport in planetary ring systems due to particle erosion mechanisms. I - Theory, numerical methods, and illustrative examples. *Icarus*, **80**, 136–166.

Esposito, L. W. 1979. Extensions to the classical calculation of the effect of mutual shadowing in diffuse reflection. *Icarus*, **39**, 69–80.

Esposito, L. W., and Lumme, K. 1977. The tilt effect for Saturn's rings. *Icarus*, **31**, 157–167.

Estrada, P. R., Durisen, R. H., Cuzzi, J. N., and Morgan, D. A. 2015. Combined structural and compositional evolution of planetary rings due to micrometeoroid impacts and ballistic transport. *Icarus*, **252**, 415–439.

Ferrari, C., Brooks, S., Edgington, S., Leyrat, C., Pilorz, S., and Spilker, L. 2009. Structure of self-gravity wakes in Saturn's A ring as measured by Cassini CIRS. *Icarus*, **199**, 145–153.

Ferrin, I. 1975. On the structure of Saturn's rings and the 'real' rotational period for the planet. *Astrophys. Space Sci.*, **33**, 453–457.

Franklin, F. A., Cook, A. F., Barrey, R. T. F., Roff, C. A., Hunt, G. E., and de Rueda, H. B. 1987. Voyager observations of the azimuthal brightness variations in Saturn's rings. *Icarus*, **69**, 280–296.

French, R. G., Salo, H., McGhee, C. A., and Dones, L. 2007a. HST observations of azimuthal asymmetry in Saturn's rings. *Icarus*, **189**, 493–522.

French, R. G., Verbiscer, A., Salo, H., McGhee, C., and Dones, L. 2007b. Saturn's Rings at True Opposition. *Publ. Astron. Soc. Pacific*, **119**, 623–642.

Goldreich, P., and Lynden-Bell, D. 1965. II. Spiral arms as sheared gravitational instabilities. *Mon. Not. R. Astron. Soc.*, **130**, 125–158.

Goldreich, P., and Tremaine, S. 1978a. The excitation and evolution of density waves. *Astrophys. J.*, **222**, 850–858.

Goldreich, P., and Tremaine, S. 1978b. The velocity dispersion in Saturn's rings. *Icarus*, **34**, 227–239.

Goldreich, P., Rappaport, N., and Sicardy, B. 1995. Single sided shepherding. *Icarus*, **118**, 414–417.

Hahn, J. M., and Spitale, J. N. 2013. An N-body Integrator for Gravitating Planetary Rings, and the Outer Edge of Saturn's B Ring. *Astrophys. J.*, **772**, 122.

Hämeen-Anttila, K. A. 1978. An improved and generalized theory for the collisional evolution of Keplerian systems. *Astrophys. Space Sci.*, **58**, 477–519.

Hämeen-Anttila, K. A. 1982. Saturn's rings and bimodality of Keplerian systems. *Earth, Moon & Planets*, **26**, 171–196.

Hämeen-Anttila, K. A. 1984. Collisional theory of non-identical particles in a gravitational field. *Earth, Moon & Planets*, **31**, 271–299.

Hämeen-Anttila, K. A., and Lukkari, J. 1980. Numerical simulations of collisions in Keplerian systems. *Astrophys. Space Sci.*, **71**, 475–497.

Hämeen-Anttila, K. A., and Salo, H. 1993. Generalized Theory of Impacts in Particulate Systems. *Earth, Moon & Planets*, **62**, 47–84.

Hänninen, J., and Salo, H. 1994. Collisional simulations of satellite Lindblad resonances. 2: Formation of narrow ringlets. *Icarus*, **108**, 325–346.

Hänninen, J., and Salo, H. 1995. Formation of isolated narrow ringlets by a single satellite. *Icarus*, **117**, 435–438.

Hansen, Alexander K, and Lewis, Mark C. 2015. Simulating"Straw"in the Keeler Gap Region. In: *AAS/Division for Planetary Sciences Meeting Abstracts*, vol. 47.

Hapke, B. 1986. Bidirectional reflectance spectroscopy. IV - The extinction coefficient and the opposition effect. *Icarus*, **67**, 264–280.

Hapke, B. 1990. Coherent backscatter and the radar characteristics of outer planet satellites. *Icarus*, **88**, 407–417.

Hapke, B. 2002. Bidirectional Reflectance Spectroscopy. 5. The Coherent Backscatter Opposition Effect and Anisotropic Scattering. *Icarus*, **157**, 523–534.

Hapke, B. 2008. Bidirectional reflectance spectroscopy. 6. Effects of porosity. *Icarus*, **195**, 918–926.

Harris, A. W. 1984. The origin and evolution of planetary rings. Pages 641–659 of: Greenberg, R., and Brahic, A. (eds), *Planetary Rings*. Tucson Arizona: Univ. of Arizona Press.

Hatzes, A., Bridges, F. G., and Lin, D. N. C. 1988. Collisional properties of ice spheres at low impact velocities. *Mon. Not. R. Astron. Soc.*, **231**, 1091–1115.

Hedman, M. M., and Nicholson, P. D. 2014. More Kronoseismology with Saturn's rings. *Mon. Not. Royal Astron. Soc.*, **444**, 1369–1388.

Hedman, M. M., and Nicholson, P. D. 2016. The B-ring's surface mass density from hidden density waves: Less than meets the eye? *ArXiv e-prints 1601.07955*.

Hedman, M. M., Nicholson, P. D., Salo, H., Wallis, B. D., Buratti, B. J., Baines, K. H., Brown, R. H., and Clark, R. N. 2007. Self-gravity wake structures in Saturn's A ring revealed by Cassini VIMS. *Astron. J.*, **133**, 2624–2629.

Hedman, M. M., Burns, J. A., Evans, M. W., Tiscareno, M. S., and Porco, C. C. 2011. Saturn's Curiously Corrugated C Ring. *Science*, **332**, 708–711.

Hedman, M. M., Nicholson, P. D., and Salo, H. 2014. Exploring Overstabilities in Saturn's A Ring Using Two Stellar Occultations. *Astron.J*, **148**, 1–9.

Hernquist, L., and Katz, N. 1989. TREESPH - A unification of SPH with the hierarchical tree method. *Astrophys. J., Supp.*, **70**, 419–446.

Hertz, H. 1882. Über die Berührung fester elastischer Körper. *J. f. Reine Angew. Math.*, **92**, 156.

Hyodo, R., and Ohtsuki, K. 2014. Collisional Disruption of Gravitational Aggregates in the Tidal Environment. *Astrophys. J.*, **787**, 56.

Hyodo, R., and Ohtsuki, K. 2015. Saturn's F ring and shepherd satellites a natural outcome of satellite system formation. *Nature Geoscience*, **8**, 686–689.

Hyodo, R., Ohtsuki, K., and Takeda, T. 2015a. Formation of Multiple-satellite Systems From Low-mass Circumplanetary Particle Disks. *Astron. J.*, **799**, 40.

Hyodo, R., Charnoz, S., Ohtsuki, K., and Genda, H. 2015b (Nov.). Physics of Tidal Disruption of Big Objects at the Close Encounter to Saturn. Page 218.10 of: *Bull. American Astron. Soc.* AAS/Division for Planetary Sciences Meeting Abstracts, vol. 47.

Julian, W. H., and Toomre, A. 1966. Non-axisymmetric responses of differentially rotating disks of stars. *Astrophys. J.*, **146**, 810–827.

Karjalainen, R. 2007. Aggregate impacts in Saturn's rings. *Icarus*, **189**, 523–537.

Karjalainen, R., and Salo, H. 2004. Gravitational accretion of particles in Saturn's rings. *Icarus*, **172**, 328–348.

Kolvoord, R. A., Burns, J. A., and Showalter, M. R. 1990. Periodic features in Saturn's F ring - Evidence for nearby moonlets. *Nature*, **345**, 695–697.

Langbert, Zachary, and Lewis, Mark C. 2014. Processing Hard Sphere Collisions on a GPU Using OpenCL. Pages 35–41 of: *PDPTA*, vol. 1. CSREA Press.

Latter, H. N., and Ogilvie, G. I. 2006. The linear stability of dilute particulate rings. *Icarus*, **184**, 498–516.

Latter, H. N., and Ogilvie, G. I. 2008. Dense planetary rings and the viscous overstability. *Icarus*, **195**, 725–751.

Latter, H. N., and Ogilvie, G. I. 2009. The viscous overstability, nonlinear wavetrains, and finescale structure in dense planetary rings. *Icarus*, **202**, 565–583.

Latter, H. N., and Ogilvie, G. I. 2010. Hydrodynamical simulations of viscous overstability in Saturn's rings. *Icarus*, **210**, 318–329.

Leinhardt, Z. M., Ogilvie, G. I., Latter, H. N., and Kokubo, E. 2012. Tidal disruption of satellites and formation of narrow rings. *Mon. Not. R. Astron. Soc.*, **424**, 1419–1431.

Lewis, M. C., and Stewart, G. R. 2000. Collisional Dynamics of Perturbed Planetary Rings. I. *Astron. J.*, **120**, 3295–3310.

Lewis, M. C., and Stewart, G. R. 2002. A new methodology for granular flow simulations of planetary rings - coordinates and boundary conditions. Pages 292–297 of: H., Hamza M. (ed), *Proceedings of the IASTED International Conference, Modeling and Simulation*. ACTA Press.

Lewis, M. C., and Stewart, G. R. 2003. A new methodology for granular flow simulations of planetary rings - collision handling. Pages 292–297 of: H., Hamza M. (ed), *Proceedings of the IASTED International Conference, Modeling and Simulation, Palm Springs*. ACTA Press.

Lewis, M. C., and Stewart, G. R. 2005. Expectations for Cassini observations of ring material with nearby moons. *Icarus*, **178**, 124–143.

Lewis, M. C., and Stewart, G. R. 2007. Collisional simulations of the F ring with Prometheus and Pandora. Page 26.08 of: *AAS/Division for Planetary Sciences Meeting Abstracts*, vol. 39.

Lewis, M. C., and Stewart, G. R. 2009. Features around embedded moonlets in Saturn's rings: The role of self-Gravity and particle size distributions. *Icarus*, **199**, 387–412.

Lewis, Mark, and Massingill, Berna L. 2006. Multithreaded Collision Detection in Java. Pages 583–592 of: *PDPTA*.

Lewis, Mark, Maly, Matthew, and Massingill, Berna L. 2009. Hybrid Parallelization of N-Body Simulations Involving Collisions and Self-Gravity. Pages 324–330 of: *PDPTA*.

Lewis, Mark, Stewart, Glen, Leezer, Jason, and West, Amy. 2011. Negative diffusion in planetary rings with a nearby Moon. *Icarus*, **213**(1), 201–217.

Lewis, Mark C, and Stewart, Glen R. 2006a. Simulating Saturns Keeler Gap Region. *Proceedings of the 17th IASTED international conference on Modeling and Simulation, Montreal, Canada*, 268–273.

Lewis, Mark C, and Stewart, GR. 2006b. Simulating the Keeler gap in Saturn's rings: Wake and edge dynamics. Page 560 of: *Bulletin of the American Astronomical Society*, vol. 38.

Lewis, Mark C, and Wing, Nick. 2002. A distributed methodology for hard sphere collisional simulations. Pages 404–409 of: *Proceedings of the International Conference on Parallel and Distributed Processing Techniques and Applications-Volume 1*. CSREA Press.

Lin, D. N. C., and Bodenheimer, P. 1981. On the stability of Saturn's rings. *Astrophys. J. Lett.*, **248**, L83–L86.

Longaretti, P.-Y., and Rappaport, N. 1995. Viscous overstabilities in dense narrow planetary rings. *Icarus*, **116**, 376–396.

Lukkari, J. 1981. Collisional amplification of density fluctuations in Saturn's rings. *Nature*, **292**, 433–435.

Lumme, K., and Bowell, E. 1981. Radiative transfer in the surfaces of atmosphereless bodies. I - Theory. II - Interpretation of phase curves. *Astron. J.*, **86**, 1694–1721.

Lumme, K., Esposito, L. W., Irvine, W. M., and Baum, W. A. 1977. Azimuthal brightness variations of Saturn's rings. II - Observations at an intermediate tilt angle. *Astrophys. J. Lett.*, **216**, L123–L126.

Lumme, K., Irvine, W. M., and Esposito, L. W. 1983. Theoretical interpretation of the ground-based photometry of Saturn's B ring. *Icarus*, **53**, 174–184.

Lynden-Bell, D., and Kalnajs, A.J. 1972. On the Generating Mechanism of Spiral Structure. *Mon. Not. R. Astron. Soc.*, **157**, 1–30.

Makino, J., and Funato, Y. 1993. The GRAPE Software System. *Publications of the Astronomical Society of Japan*, **45**, 279–288.

Michikoshi, S., Fujii, A., Kokubo, E., and Salo, H. 2015. Dynamics of Self-gravity Wakes in Dense Planetary Rings. I. Pitch Angle. *Astrophys. J*, **812**, 151.

Mishchenko, M. I. 1992. The angular width of the coherent backscatter opposition effect - an application to icy outer planet satellites. *Ap&SS*, **194**, 327–333.

Morishima, R., and Salo, H. 2004. Spin rates of small moonlets embedded in planetary rings: I. Three-body calculations. *Icarus*, **167**, 330–346.

Morishima, R., and Salo, H. 2006. Simulations of dense planetary rings IV. Spinning self-gravitating particles with size distributions. *Icarus*, **181**, 272–291.

Morishima, R., Spilker, L., Salo, H., Ohtsuki, K., Altobelli, N., and Pilortz, S. 2010. A multilayer model for thermal infrared emission of Saturn's rings II: Albedo, spins, and vertical mixing of ring particles inferred from Cassini CIRS. *Icarus*, **210**, 330–345.

Morishima, R., Spilker, L., and Ohtsuki, K. 2011. A multilayer model for thermal infrared emission of Saturn's rings. III: Thermal inertia inferred from Cassini CIRS. *Icarus*, **215**(Sept.), 107–127.

Morishima, R., Spilker, L., and Turner, N. 2014. Azimuthal temperature modulations of Saturn's A ring caused by self-gravity wakes. *Icarus*, **228**, 247–259.

Mosqueira, I. 1996. Local simulations of perturbed dense planetary rings. *Icarus*, **122**, 128–152.

Muinonen, K. O., Sihvola, A. H., Lindell, I. V., and Lumme, K. A. 1991. Scattering by a small object close to an interface. II. Study of backscattering. *Journal of the Optical Society of America A*, **8**, 477–482.

Nelson, R. M., Hapke, B. W., Smythe, W. D., and Spilker, L. J. 2000. The Opposition Effect in Simulated Planetary Regoliths. Reflectance and Circular Polarization Ratio Change at Small Phase Angle. *Icarus*, **147**, 545–558.

Nicholson, P. D., French, R. G., Campbell, D. B., Margot, J.-L., Nolan, M. C., Black, G. J., and Salo, H. J. 2005. Radar imaging of Saturn's rings. *Icarus*, **177**, 32–62.

Ohtsuki, K. 1992. Equilibrium velocities in planetary rings with low optical depth. *Icarus*, **95**, 265–282.

Ohtsuki, K. 1993. Capture probability of colliding planetesimals: Dynamical constraints on accretion of planets, satellites, and ring particles. *Icarus*, **106**, 228–246.

Ohtsuki, K. 1999. Evolution of particle velocity dispersion in a circumplanetary disk due to inelastic collisions and gravitational interactions. *Icarus*, **137**, 152–177.

Ohtsuki, K. 2004a. Formulation and analytic calculation for the spin angular momentum of a moonlet due to inelastic collisions of ring particles. *Earth Planets Space*, **56**, 909–919.

Ohtsuki, K. 2004b. On the rotation of a moonlet embedded in planetary rings. *Icarus*, **172**, 432–445.

Ohtsuki, K. 2005. Rotation rates of particles in Saturn's rings. *Astrophys. J.*, **626**, L61–L64.

Ohtsuki, K. 2006a. Rotation rate and velocity dispersion of planetary ring particles with size distribution. I. Formulation and analytic calculation. *Icarus*, **183**, 373–383.

Ohtsuki, K. 2006b. Rotation rate and velocity dispersion of planetary ring particles with size distribution. II. Numerical simulation for gravitating particles. *Icarus*, **183**, 384–395.

Ohtsuki, K. 2012. Collisions and gravitational interactions between particles in planetary rings. *Prog. Theor. Phys. Suppl.*, **195**, 29–47.

Ohtsuki, K., and Emori, H. 2000. Local N-Body Simulations for the Distribution and Evolution of Particle Velocities in Planetary Rings. *Astron. J.*, **119**, 403–416.

Ohtsuki, K., and Emori, H. 2000. Local N-body simulations for the distribution and evolution of particle velocities in planetary rings. *Astron. J.*, **119**, 403–416.

Ohtsuki, K., and Toyama, D. 2005. Local N-body simulations for the rotation rates of particles in planetary rings. *Astron. J.*, **130**, 1302–1310.

Ohtsuki, K., Stewart, G. R., and Ida, S. 2002. Evolution of Planetesimal Velocities Based on Three-Body Orbital Integrations and Growth of Protoplanets. *Icarus*, **155**(Feb.), 436–453.

Ohtsuki, K., Yasui, Y., and Daisaka, H. 2013. Accretion Rates of Moonlets Embedded in Circumplanetary Particle Disks. *Astronomical Journal*, **146**, 25.

Perrine, R. P., and Richardson, D. C. 2006. A Computational Model of Moons in Planetary Ring Gaps. Page 560 of: *AAS/Division for Planetary Sciences Meeting Abstracts #38*. Bulletin of the American Astronomical Society, vol. 38.

Perrine, R. P., and Richardson, D. C. 2007. Numerical Studies of Satellite-Ring Interactions. Page 425 of: *AAS/Division for Planetary Sciences Meeting Abstracts #39*. Bulletin of the American Astronomical Society, vol. 39.

Perrine, R. P., and Richardson, D. C. 2012. N-body simulations of cohesion in dense planetary rings: A study of cohesion parameters. *Icarus*, **219**, 515–533.

Perrine, R. P., Richardson, D. C., and Scheeres, D. J. 2011. A numerical model of cohesion in planetary rings. *Icarus*, **212**, 719–735.

Petit, J. M., and Hénon, M. 1987. A numerical simulation of planetary rings. I. Binary encounters. *Astron. & Astrophys.*, **173**, 389–404.

Porco, C. C., Weiss, J. W., Richardson, D. C., Dones, L., Quinn, T., and Throop, H. 2008. Simulations of the dynamical and light-scattering behavior of Saturn's rings and the derivation of ring particle and disk properties. *Astron. J.*, **136**, 2172–2200.

Porco, C.C., Thomas, P.C., Weiss, J. W., and Richardson, D. C. 2007. Saturn's small inner satellites: Clues to their origins. *Science*, **318**, 1602–1607.

Pöschel, T., and Schwager, T. 2005. *Computational Granular Dynamics*. Springer-Verlag Berlin Heidelberg.

Poulet, F., Cuzzi, J. N., French, R. G., and Dones, L. 2002. A Study of Saturn's Ring Phase Curves from HST Observations. *Icarus*, **158**, 224–248.

Rein, H., and Latter, H. N. 2013. Large-scale N-body simulations of the viscous overstability in Saturn's rings. *Mon. Not. Royal Astron. Soc.*, **431**, 145–158.

Rein, H., and Liu, S.-F. 2012. REBOUND: an open-source multi-purpose N-body code for collisional dynamics. *Astron. & Astrophys.*, **537**, A128.

Rein, Hanno, and Liu, S-F. 2012. REBOUND: an open-source multi-purpose N-body code for collisional dynamics. *Astronomy & Astrophysics*, **537**, A128.

Reitsema, H. J., Beebe, R. F., and Smith, B. A. 1976. Azimuthal brightness variations in Saturn's rings. *Astron. J.*, **81**, 209–215.

Richardson, D. C. 1993. A new tree code method for simulation of planetesimal dynamics. *Mon. Not. R. Astron. Soc.*, **261**, 396–414.

Richardson, D. C., Quinn, T., Stadel, J., and Lake, G. 2000. Direct Large-Scale N-Body Simulations of Planetesimal Dynamics. *Icarus*, **143**, 45–59.

Richardson, D.C. 1994. Tree code simulations of planetary rings. *Mon. Not. R. Astron. Soc.*, **269**, 493–511.

Robbins, S. J., Stewart, G. R., Lewis, M. C., Colwell, J. E., and Sremčević, M. 2010. Estimating the masses of Saturn's A

and B rings from high-optical depth N-body simulations and stellar occultations. *Icarus*, **206**, 431–445.

Safranov, V. 1969. *Evolution of the protoplanetary cloud and the formation of the earth and planets*. Nauka, NASA TTF-667.

Salmon, J., Charnoz, S., Crida, A., and Brahic, A. 2010. Long-term and large-scale viscous evolution of dense planetary rings. *Icarus*, **209**, 771–785.

Salo, H. 1987a. Collisional evolution of rotating, non-identical particles. *Moon Planets*, **38**, 149–181.

Salo, H. 1987b. Numerical simulations of collisions between rotating particles. *Icarus*, **70**, 37–51.

Salo, H. 1991. Numerical simulations of dense collisional systems. *Icarus*, **92**, 367–368.

Salo, H. 1992a. Gravitational wakes in Saturn's rings. *Nature*, **359**, 619–621.

Salo, H. 1992b. Numerical simulations of dense collisional systems. II. Extended distribution of particle sizes. *Icarus*, **96**, 85–106.

Salo, H. 1995. Simulations of dense planetary rings. III. Self-gravitating identical particles. *Icarus*, **117**, 287–312.

Salo, H. 2001. Numerical Simulations of the Collisional Dynamics of Planetary Rings. Pages 330–349 of: Pöschel, T., and Luding, S. (eds), *Granular Gases*. Lecture Notes in Physics, Berlin Springer Verlag, vol. 564.

Salo, H., and French, R. G. 2010. The opposition and tilt effects of Saturn's rings from HST observations. *Icarus*, **210**, 785–816.

Salo, H., and Karjalainen, R. 2003. Photometric modeling of Saturn's rings. I. Monte Carlo method and the effect of nonzero volume filling factor. *Icarus*, **164**, 428–460.

Salo, H., and Schmidt, J. 2010. N-body simulations of viscous instability of planetary rings. *Icarus*, **206**, 390–409.

Salo, H., Schmidt, J., and Spahn, F. 2001. Viscous overstability in Saturn's B ring: I. Direct simulations and measurement of transport coefficients. *Icarus*, **153**, 295–315.

Salo, H., Karjalainen, R., and French, R. G. 2004. Photometric modeling of Saturn's rings. II. Azimuthal asymmetry in reflected and transmitted light. *Icarus*, **170**, 70–90.

Salo, H. J., and Schmidt, J. 2007. Release of impact-debris in perturbed ring regions: Dynamical and photometric simulations. Page 425 of: *Bull. American Astron. Soc.* Bull. American Astron. Soc., vol. 38.

Schmidt, J., and Salo, H. 2003. A weakly nonlinear model for viscous overstability in Saturn's dense rings. *Physical Review Letters*, **90**(6), 061102.

Schmidt, J., Salo, H., Spahn, F., and Petzschmann, Olaf. 2001. Viscous overstability in Saturn's B ring: II. Hydrodynamic theory and comparison to simulations. *Icarus*, **153**, 316–331.

Schmidt, J., Ohtsuki, K., Rappaport, N., Salo, H., and Spahn, F. 2009. Dynamics of Saturn's Dense Rings. Page 413 of: Dougherty, M. K., Esposito, L. W., and Krimigis, S. M. (eds), *Saturn from Cassini-Huygens*.

Schmit, U., and Tscharnuter, W.M. 1995. A fluid dynamical treatment of the common action of self-gravitation, collisions, and rotation in Saturn's B-ring. *Icarus*, **115**, 304–319.

Schmit, U., and Tscharnuter, W.M. 1999. On the formation of the fine–scale structure in Saturn's B ring. *Icarus*, **138**, 173–187.

Sellwood, J. A. 2014. GALAXY package for N-body simulation. *ArXiv e-prints 1406.6606*.

Showalter, M. R. 1991. Visual detection of 1981S13, Saturn's eighteenth satellite, and its role in the Encke gap. *Nature*, **351**, 709–713.

Showalter, M. R. 1998. Detection of centimeter-sized meteoroid impact events in Saturn's F ring. *Science*, **282**, 1099–1102.

Showalter, M. R., Cuzzi, J. N., Marouf, E. A., and Esposito, L. W. 1986. Satellite 'wakes' and the orbit of the Encke Gap moonlet. *Icarus*, **66**, 297–323.

Shu, F. H. 1984. Waves in planetary rings. Pages 513–561 of: Greenberg, R., and Brahic, A. (eds), *Planetary Rings*. Tucson Arizona: Univ. of Arizona Press.

Shu, F. H., and Stewart, G. R. 1985. The collisional dynamics of particulate disks. *Icarus*, **62**, 360–383.

Shukhman, I.G. 1984. Collisional dynamics of particles in Saturn's rings. *Sov. Astron.*, **28**, 574–585.

Spahn, F., and Sremčević, M. 2000. Density patterns induced by small moonlets in Saturn's rings? *Astron. & Astrophys.*, **358**, 368–372.

Spahn, F., Hertzsch, J.-M., and Brilliantov, N.V. 1995. The role of particle collisions for the dynamics in planetary rings. *Chaos, Solitons and Fractals*, **5**, 1945–1964.

Springel, V. 2005. The cosmological simulation code GADGET-2. *Mon. Not. Royal Astron. Soc.*, **364**, 1105–1134.

Sremčević, M., Schmidt, J., Salo, H., Seiß, M., Spahn, F., and Albers, N. 2007. A belt of moonlets in Saturn's A ring. *Nature*, **449**, 1019–1021.

Stadel, Joachim, Wadsley, James, and Richardson, Derek C. 2002. High performance computational astrophysics with pkdgrav/gasoline. Pages 501–523 of: *High Performance Computing Systems and Applications*. Springer.

Stewart, G. R. 1991. Nonlinear satellite wakes in planetary rings. I - Phase-space kinematics. *Icarus*, **94**, 436–450.

Stewart, G. R., Lin, D. N. C., and Bodenheimer, P. 1984. Collision-induced transport processes in planetary rings. Pages 447–512 of: Greenberg, R., and Brahic, A. (eds), *Planetary Rings*. Tucson Arizona: Univ. of Arizona Press.

Stewart, S. T., and Leinhardt, Z. M. 2009. Velocity-Dependent Catastrophic Disruption Criteria for Planetesimals. *Astrophys. J. Lett.*, **691**, L133–L137.

Supulver, K. D., Bridges, F. G., and Lin, D. N. C. 1995. The coefficient of restitution of ice particles in glancing collisions: Experimental results for unfrosted surfaces. *Icarus*, **113**, 188–199.

Tanaka, H., Ohtsuki, K., and Daisaka, H. 2003. A new formulation of the viscosity in planetary rings. *Icarus*, **161**, 144–156.

Thompson, W. T., Lumme, K., Irvine, W. M., Baum, W. A., and Esposito, L. W. 1981. Saturn's rings - Azimuthal variations, phase curves, and radial profiles in four colors. *Icarus*, **46**, 187–200.

Thomson, F. S., Marouf, E. A., Tyler, G. L., French, R. G., and Rappoport, N. J. 2007. Periodic microstructure in Saturn's rings A and B. *Gephys. Res. Lett.*, **34**, 24203–+.

Tiscareno, M. S., Burns, J. A., Hedman, M. M., Porco, C. C., Weiss, J. W., Murray, C. D., and Dones, L. 2006. Observation of "propellers" indicates 100-metre diameter moonlets reside in Saturn's A-ring. *Nature*, **440**, 648–650.

Tiscareno, M. S., Burns, J. A., Nicholson, P. D., Hedman, M. M., and Porco, C. C. 2007. Cassini imaging of Saturn's rings: II. A wavelet technique for analysis of density waves and other radial structure in the rings. *Icarus*, **189**, 14–34.

Tiscareno, M. S., Perrine, R. P., Richardson, D. C., Hedman, M. M., Weiss, J. W., Porco, C. C., and Burns, J. A. 2010. An Analytic Parameterization of Self-Gravity Wakes in Saturn's Rings, with Application to Occultations and Propellers. *Astron. J.*, **139**, 492–503.

Tiscareno, M. S., Hedman, M. M., Burns, J. A., and Castillo-Rogez, J. 2013a. Compositions and Origins of Outer Planet Systems: Insights from the Roche Critical Density. *Astrophys. J. Lett.*, **765**, L28.

Tiscareno, M. S., Hedman, M. M., Burns, J. A., Weiss, J. W., and Porco, C. C. 2013b. Probing the inner boundaries of Saturn's A ring with the Iapetus -1:0 nodal bending wave. *Icarus*, **224**, 201–208.

Toomre, A. 1964. On the gravitational stability of a disk of stars. *Astrophys. J.*, **139**, 1217–1238.

Toomre, A. 1981. What amplifies the spirals. Pages 111–136 of: Fall, S. M., and Lynden-Bell, D. (eds), *Structure and Evolution of Normal Galaxies*.

Toomre, A., and Kalnajs, A. J. 1991. Spiral chaos in an orbiting patch. Pages 341–358 of: Sundelius, B. (ed), *Dynamics of Disc Galaxies*. Almquist-Wiksell, Göteborg.

Tremaine, S. 2003. On the origin of irregular structure in Saturn's rings. *Astron. J.*, **125**(Feb.), 894–901.

Trulsen, J. 1972. Numerical simulation of jetstreams,1:The three-dimensional case. *Astrophys. Space Sci.*, **17**, 241–262.

Ward, W. R. 1981. On the radial structure of Saturn's rings. *Geophys. Res. Lett.*, **8**, 641–643.

Weidenschilling, S. J., Chapman, C. R., Davis, D. R., and Greenberg, R. 1984. Ring particles: Collisional interactions and physical nature. Pages 367–415 of: Greenberg, R., and Brahic, A. (eds), *Planetary Rings*. Tucson Arizona: Univ. of Arizona Press.

Wisdom, J., and Tremaine, S. 1988. Local simulations of planetary rings. *Astron. J.*, **95**, 925–940.

Yasui, Y., Ohtsuki, K., and Daisaka, H. 2012. Viscosity in Planetary Rings with Spinning Self-gravitating Particles. *Astron. J.*, **143**, 110.

Yasui, Y., Ohtsuki, K., and Daisaka, H. 2014. Gravitational Accretion of Particles onto Moonlets Embedded in Saturn's Rings. *Astrophys. J.*, **797**, 93.